

RICE UNIVERSITY

**Plasmonic Nanoparticle Laden Medium for Solar/Thermal
Energy Storage**

by

Toni Kathleen Tullius

A THESIS SUBMITTED
IN PARTIAL FULFILLMENT OF THE
REQUIREMENTS FOR THE DEGREE

Doctor of Philosophy

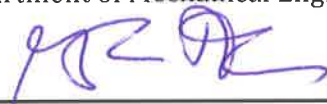
APPROVED, THESIS COMMITTEE



Yildiz Bayazitoglu, Chair
H.S. Cameron Chair Professor of Mechanical
Engineering,
Department of Mechanical Engineering



Andrew Dick
Assistant Professor,
Department of Mechanical Engineering



Robert Vajtai
Senior Faculty Fellow
Department of Materials Science and
Nanoengineering

HOUSTON, TEXAS
July 2015

ABSTRACT

Plasmonic Nanoparticle Laden Medium for Solar/Thermal Energy Storage

by

Toni Kathleen Tullius

Nanofluids have become a popular way of increasing the efficiency in solar energy applications and enhancing the thermophysical properties of the fluid. This thesis contributes to the field of solar energy utilization by two distinct projects. The first part is a thermal analysis involving a single plasmonic nanoparticle, exposed to radiation, in a solid medium that undergoes phase change creating a liquid film around the particle. The temperature profiles for the particle, film, and solid medium are analyzed. It is shown that the larger particle heats faster, developing a smaller surrounding film; however, the integrity of the smaller particle will stay intact for longer. Compromise between the thermal resistance at the interface of the particle and film as well as the absorption from radiation in order to determine the proper particle type, size, and medium is studied. The effect of the inclusion of the particle/film interface resistance is clarified.

In the second part of the thesis, a nanofluid mixture containing two or more different types of plasmonic nanoparticles, based on the absorption of the particles when exposed to radiation, is optimized. Because of the tunable plasmonic properties of metallic nanoparticles and the many possible variables to consider,

two different optimization techniques were used in order to determining the correct recipe of nanoparticles submerged in water for a given temperature in order to get the maximum absorption. This contribution will help to determine which particle mixture would be required when exposed to radiation depending on the particular set of particles, size of particles, height of the container, concentration, and incident temperature.

Acknowledgments

Foremost, I would like to express my sincere gratitude to my advisor, Dr. Yildiz Bayazitoglu for her guidance and support throughout my work. I would also like to thank my other committee members Dr. Vajtai and Dr. Dick.

A special thanks to Dr. Richard Tapia, Alliances for Graduate Education and Professoriate (AGEP), and NSF for their continuous support throughout my graduate school career.

Also, thank you to all of my friends that I have made here at Rice including to but not limited to Theresa Chatman, Maria Maldonado, Nabor Reyna, Kasim Toprak and most of all Jami Tullius for always encouraging me to finish; without them, I would not have been successful.

I want to thank my family for their unending encouragement and love, especially my mother, brother, sister, and sister in law. You four keep me grounded and sane and were always there when I was feeling low. I love you all.

I dedicate this thesis to all my angels: father, grandfather, grandmother dear, and cousin whose memories are constantly making me strive for my best. I also dedicate this to my Nana and Grandpa whom I will love forever and always.

Contents

Acknowledgments	iii
Contents.....	iv
List of Figures	vi
List of Tables	9
Introduction	10
Temperature of a metallic nanoparticle embedded in a phase change media exposed to radiation	13
2.1 Introduction	13
2.1.1 Plasmonic Properties	17
2.2 Nanoparticle mathematical formulation.....	20
2.2.1 Energy equation for the particle	21
2.2.2 Energy equations for the solid and liquid medium	26
2.2.3 Liquid solid interface velocity equations	27
2.2.4 Non-dimensionalized terms.....	29
2.3 Computational Analysis	30
2.3.1 Validation	32
2.3.2 Numerical Results.....	34
2.4 Conclusion.....	43
2.5 List of Variables	45
Analysis of a Nanofluid Exposed to Radiation.....	49
3.1 Introduction	49
3.1.1 Absorption Properties of Nanoparticles	52
3.2 Hybrid construction	57
3.2.1 Absorption Analysis of Nanoparticles	60
3.3 Hybrid Optimization	63
3.3.1 Method 1: Graphically determining a hybrid mixture	64
3.3.2 Method 2: Algorithm determining a hybrid mixture	69
3.4 Results based on the two methods.....	73
3.5 Conclusion.....	76
3.6 List of Variables	78

Concluding Remarks.....	82
Appendix A	84
A.1 Boiling and melting temperature shift for a nanofluid	84
Appendix B.....	90
B.1 Mathematical steps for Chapter 2-Thermal Storage	90
B.1.1 Step 1: Particle within a solid medium	90
B.1.2 Step 2: Film surrounding the particle within a solid medium	92
B.2 Code describing the particle in a solid medium with a film formation	97
Appendix C.....	120
C.1 Construction for the ‘hybrid’ Nanofluid	120
C.2 Optimization for the ‘hybrid’ Nanofluid	124
C.3 Code for describing the optimization of the hybrid nanofluid	131
Appendix D	142
D.1 Derivation for the Van Der Waal Equation	142
D.2 Derivation for the Clausius-Clapeyron Equation	142
D.3 Derivation for the Polarizability.....	144
D.4 Derivation for Drude’s Model.....	148
D.5 Derivation for Level Set Method	150
D.6 Derivation of the angle between radial and tangential direction	152
D.7 Comments about Plasmonic Properties	155
D.8 Code for Rayleigh Theory	159
References	168

List of Figures

Figure 2.1.1: Film formulations of one nanoparticle when it reaches the melting temperature.	16
Figure 2.1.2: Absorption versus wavelength a) for a particle with varying composition, particle size, and medium; b) for a Au 90 nm particle with its surrounding liquid film. Note: (90,100) nm implies that the particle has a diameter of 90 nm and a surrounding film diameter of 100 nm.	18
Figure 2.2.1: Film formulation of one nanoparticle.....	20
Figure 2.3.1: Validation for the particle temperature profile of a 90 nm Au particle in H₂O.....	33
Figure 2.3.2: Validation of the medium temperature profile vs. the non-dimensional r direction for a 90 nm Au particle in H₂O using separation of variables (SV).....	33
Figure 2.3.3: Temperature profile vs. time a) for various nanoparticle materials, sizes, and mediums b) a 90 nm Au particle in H₂O with different intensities.....	37
Figure 2.3.4: The liquid film diameter vs. non dimensional time a) for various nanoparticle properties b) for different intensities for a 90 nm Au particle in H₂O.....	38
Figure 2.3.5: The temperature profile of the particle, film, and surrounding medium vs. τ for a) a 90 nm Au particle in H₂O b) a 90 nm Au particle n-Octadecane, c) a 30 nm Au particle in H₂O, d) a 90 nm Al particle in H₂O, e) a 60 nm Cu particle in n-Octadecane, and f) a 90 nm Cu particle in n-Octadecane.	41
Figure 3.1.1: An electric field exposed to a metal nanoparticle results in an oscillation of the particle	53
Figure 3.1.2: Absorption curves for a) each different type of particle with diameter of 50 nm in water b) different Au particle diameters in water.....	54
Figure 3.1.3: The spectrum for radiation at different temperatures. Recalculated using the spectral blackbody intensity equation, Eqn. (3.2.1)....	56

Figure 3.2.1: Solar heating of a nanofluid.....	58
Figure 3.3.1: Presents the a) diameter vs. the SPR peak. b) diameter vs. the area of Q_{abs} for each particle type.....	66
Figure 3.3.2: Flow chart describing Method 1 for choosing the hybrid nanofluid	68
Figure 3.3.3: Algorithm for the hybrid nanofluid.....	72
Figure 3.4.1: The correlation between concentration and height for different temperatures. This relationship holds for every value of N	75
Figure A.1.1: The melting point depression and boiling point elevation phase change diagram.....	85
Figure B.1.1: Particle within a solid medium.	91
Figure B.1.2: Particle within a liquid film and solid medium.	93
Figure C.1.1 Solar heating of a nanofluid	121
Figure C.1.2 Solar radiation spectrum using Eqn. (C.1.1).....	122
Figure C.2.1 Description of the SPR peak.....	125
Figure C.2.2: Idea of a combination	126
Figure C.2.3 Description of A_j	128
Figure C.2.4 Description of when q_r is diminished of when q_r penetrated through the fluid and reached the bottom surface.	129
Figure C.2.5: Algorithm for the hybrid nanofluid.....	130
Figure D.3.1: The polarizability, P , is the combination of all the wavelets scattered by a region which is divided by many dipoles.....	145
Figure D.3.2: A particle surrounded by an arbitrary medium undergoing a uniform electric field.....	146
Figure D.3.3: A coated particle.....	148
Figure D.4.1: Lorentz model using simple harmonic oscillators.....	148

Figure D.6.1: Geometry for finding β when $\theta \geq 0$	153
Figure D.6.2: Geometry for finding β when $-\pi/2 \leq \theta \leq 0$	154
Figure D.6.3: Physical interpretation of the angle β	155
Figure D.7.1: Schematics of different nanoparticle shapes [39]	156

List of Tables

Table 2.1: Particle Properties	24
Table 2.2: Medium Properties	25
Table 3.1: Decay rate, oscillator strength, and transition energy for Eqn. (3.2.12).....	63
Table 3.2: Combinations for various temperatures and databases	77
Table A.1.1: Comparison of experimental data and Eqn. (A.1.3) for the melting point depression and the boiling point elevation	89
Table D.7.2: Optical properties of metal nanoparticles. Found in [39].....	157

Chapter 1

Introduction

Researchers are looking to utilize nanofluids as a way to increase the efficiency in solar energy applications. Over the past few years, researchers have introduced colloids of varying sizes into a fluid, such as water or n-octadecane, in order to enhance the thermophysical properties and the thermal energy efficiency. When exposing these mixtures to solar radiation, the nanoparticles can also increase the absorption of the fluid.

Many people have used nanofluids containing metallic particles, which have plasmonic properties, or carbon based particles in order to increase the efficiency of the base fluid. Plasmonic properties are described as a strong optical oscillations caused by photon/electron interaction located at the surface of the particle. These oscillations allow for unique, tunable absorption and scattering properties when exposed to radiation of particular frequency by varying their size, shape, and composition of the particles. Because of these

tunable properties, mechanical engineers, biologists, physicists, and chemists have all taken interest in studying metallic nanoparticles.

Two different techniques for the field of solar energy have been considered in this thesis in order to describe a hybrid nanofluid. The first analysis portrays a single metallic nanoparticle embedded in a solid phase change material exposed to radiation [1]. This analysis includes plasmonic properties of metals when exposed to a range of solar frequencies. When the particle temperature exceeds the phase change temperature an insulating liquid film forms around the particle. The temperature profiles of the solid medium, liquid film, and particle of different materials and particle diameters submerged in different mediums are presented. Analysis on the liquid film growth is also given. In addition to this study, the interface resistance between the particle and liquid film is included. A ratio is derived that determines whether the interface resistance at the particle and film is necessary to include. It is shown that a compromise must be made between the thermal resistance caused by the interface and film as well as the absorption from radiation to determine the proper particle type, size, and medium.

The second analysis views a nanofluid in bulk. In most studies, a nanofluid exposed to radiation containing one type of particle within the fluid has been considered. This thesis proposes the use of a 'hybrid' nanofluid containing two or more types of nanoparticles with water as the base fluid when exposed to radiation [2]. These particles, depending on their size, shape,

and composition, have variable peak absorption curves. Therefore, this mixture is able to utilize a broader spectrum to absorb heat. Two proposed recipes for optimizing a combination of gold, copper, aluminum, graphite, and silica dioxide gold nanoparticles into water is given numerically and graphically for different concentrations, height of the container, and number of types of particles within the nanofluid.

This remainder of this thesis is as follows. Chapter two gives the first analysis on the single nanoparticle in a solid medium undergoing phase change when exposed to radiation. Chapter 3 gives the second analysis on optimizing a hybrid nanofluid when exposed to radiation. Chapter 4 provides some concluding remarks. The Appendix provides details and derivations of some of the mathematical formulations used. Appendix A provides a small analysis on the shift of the melting/boiling temperature when nanoparticles are introduced in the fluid. Appendix B and C give a more detailed analysis of chapter 2 and 3 respectively. The MATLAB code is provided for both studies. Appendix D gives derivations of some mathematical formulations, including Van Der Waal forces, Clausius-Clapeyron equation, polarizability, Drude's model, level set method, angle between the normal and radial direction, and the Rayleigh scattering MATLAB program.

Chapter 2

Temperature of a metallic nanoparticle embedded in a phase change media exposed to radiation

2.1 Introduction

Thermal energy storage is captured when there is a change in internal energy of a material caused by latent heat, sensible heat, and/or heat caused by a thermal-chemical process. For the past ten years, latent heat storage has shown to be an attractive approach for thermal storage because large amounts of heat can be stored in small volumes with small temperature differences in the media. Thermal energy is accumulated in this material when a rise in temperature causes the phase change material (PCM) to change from a solid to liquid or liquid to vapor through the heat of fusion or heat of vaporization, respectively. Using a PCM provides a higher heat storage capacity with lower storage temperature.

Over the past decade, many people have studied the use of PCM for thermal storage [3–8]. Materials that utilize the phase change between solid and liquid have proved to be most effective. The solid-liquid PCMs comprise of organic, inorganic, and eutectic materials. Paraffins and salt hydrates are the typical choice for the PCM and more information on these types of materials can be found in [3–5]. Paraffins are compounds composed of hydrogen and carbon where all the atoms are linked by single bonds, i.e. C_nH_{2n+2} . All paraffins are colorless and odorless and are transparent in the visible range [9,10]. Paraffins between C_5 and C_{15} are liquids and the rest are waxy solids at room temperature with melting temperatures dependent on the number of carbons it contains ranging from 23-67 °C. The melting temperature increases as the number of carbons increases [11]. The paraffin used in these calculations is n-octadecane ($C_{18}H_{38}$). This material is commonly used to make crayons, candles, and electrical insulation and is affordable.

In 2007, Khodadadi and Hossienizadeh [12] proposed the idea of placing nanoparticles within the phase change material in order to improve thermal storage. In Khodadadi and Hossienizadeh's paper [12], they placed copper (Cu) nanoparticles of various concentrations into water and numerically simulated the solidification of a nanofluid in a square storage model. Fan and Khodadadi [13,14] and Nabil and Khodadadi [15] provided experimental insight of cyclohexane and eicosane both mixed with copper oxide (CuO_2) nanoparticles. This showed that the freezing rate was increased compared to the fluid with no nanoparticles because of the enhanced thermal conductivity. Hasadi and Khodadadi [16] numerically simulated the solidification of copper (Cu) nanoparticles in water. Dhaidan et al.

[17] showed experimentally and numerically the increase of the thermal conductivity using the mixture of n-octadecane with copper oxide (CuO_2) nanoparticles in a square enclosure subjected to a constant heat flux from one side. Aluminum nanoparticles and silica oxide (SiO_2) nanoparticles were mixed with n-nonadecane, n-eicosane, n-heneicosane, and n-docosane in a molecular dynamic simulation to determine the size of the particle provided by Rao et al. [18]. Cingarapu et al. [19] studied the viscosity, thermal conductivity, and total heat absorption of silica encapsulated tin (Sn/SiO_2) nanoparticles dispersed in a synthetic HFT Therminol 66 (TH66) fluid. Chieruzzi et al. [20] studied the effect of heat capacity when the base fluid was the salt mixture $\text{NaNO}_3\text{-KNO}_3$ with nanoparticles of silica (SiO_2), alumina (Al_2O_3), titana (TiO_2), and a mix of silica alumina ($\text{SiO}_2\text{-Al}_2\text{O}_3$). A computational fluid dynamics program, FLUENT, was used by Jegadheeswaran and Pohekar [21] who explored the heat transfer characteristics of micron sized copper particles during both charging and discharging modes. Ho and Gao [22] experimentally investigated how the thermal physical properties such as density, viscosity, and thermal conductivity with alumina (Al_2O_3) nanoparticles in paraffin (n-octadecane) are affected. The melting/freezing characteristics of paraffin and copper nanoparticles were studied by Wu et al. [23,24]. Wu showed that the melting/freezing rates were enhanced due to adding the nanoparticles. Zeng et al. enhanced the thermal conductivity of paraffin (n-octadecane) using silver (Ag) particles [25], silver (Ag) nanowires [26], and multiwalled carbon nanotubes [27]. All of these papers presented above concentrated on the enhancement of the thermal properties of various combinations of mediums and particles.

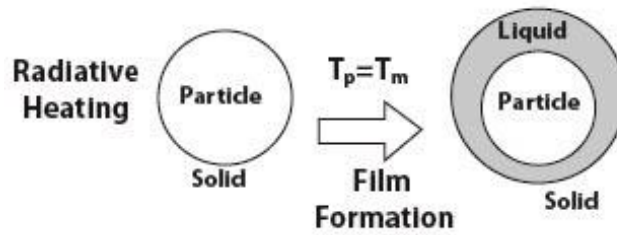


Figure 2.1.1: Film formulations of one nanoparticle when it reaches the melting temperature.

Around the particle, the temperature may exceed the melting temperature causing a liquid film to form surrounding the metal sphere and begin the two phase process, see Fig. 2.1.1. When considering solid/liquid phase change there are numerical and experimental analysis of freezing and melting paraffin wax and water in spherical enclosures [28–31]. Only a few papers have concentrated on the single particle interaction between a solid and liquid film. Uhlmann and Chalmers [32] shows that there exists a force between the solid interface and the particle that prevents the particle to lay on the solid surface unless the force of gravity is greater than the buoyant force. Shangguan et al. [33] and Garvin and Udaykumar [34] provide numerical analysis of particles experiencing the interface forces against a planar solid surface. Bulunti and Arslanturk [35] numerically investigated an inward melting of a sphere subject to radiation and convection. The focus of this paper is to understand how a metallic nanoparticle of various sizes and compositions inside a phase change material is affected when exposed to radiation.

2.1.1 Plasmonic Properties

Mechanical engineers, biologists, physicists, and chemists have all taken interest in studying metallic nanoparticles because they have unique, tunable absorption and scattering properties when interacting with photons. Gold (Au), silver (Ag), aluminum (Al), and copper (Cu) are just a few plasmonic particles that when interacting with an electric field, create strong optical resonances called surface plasmon resonances (SPR). On the surface of these metal structures, a collection of bound mobile electrons generate quantized waves or plasmons that excite from their equilibrium position and oscillate when the frequency of the incident light is in tune with their motion. The surface plasmon resonances combined with the size, shape, and composition alters the sensitivity and tunability of the optical properties [36,37]. The solid nanosphere, nanoshell, nanorod, nanocage, nanobelt, and nanohexapod structures are a few of the metallic particle shapes that have been created and tested. More information on plasmonic nanoparticles and the various shapes that have been considered can be found [38–43]. In addition to changing the physical components of the metallic nanoparticle, the particle absorption is extremely sensitive to changes in the medium that the particles are in [44,45]. Mie theory, a solution to Maxwell's equations for a sphere, provides the scattering and absorption coefficients [46]. The plasmonic properties are accounted for using Drude's model or the Drude-Lorentz model which is further described later in Sec. 2.2.1. Appendix D. 3, D.4, and D.7 provide more details on Mie theory, Drude's model, and the MATLAB code.

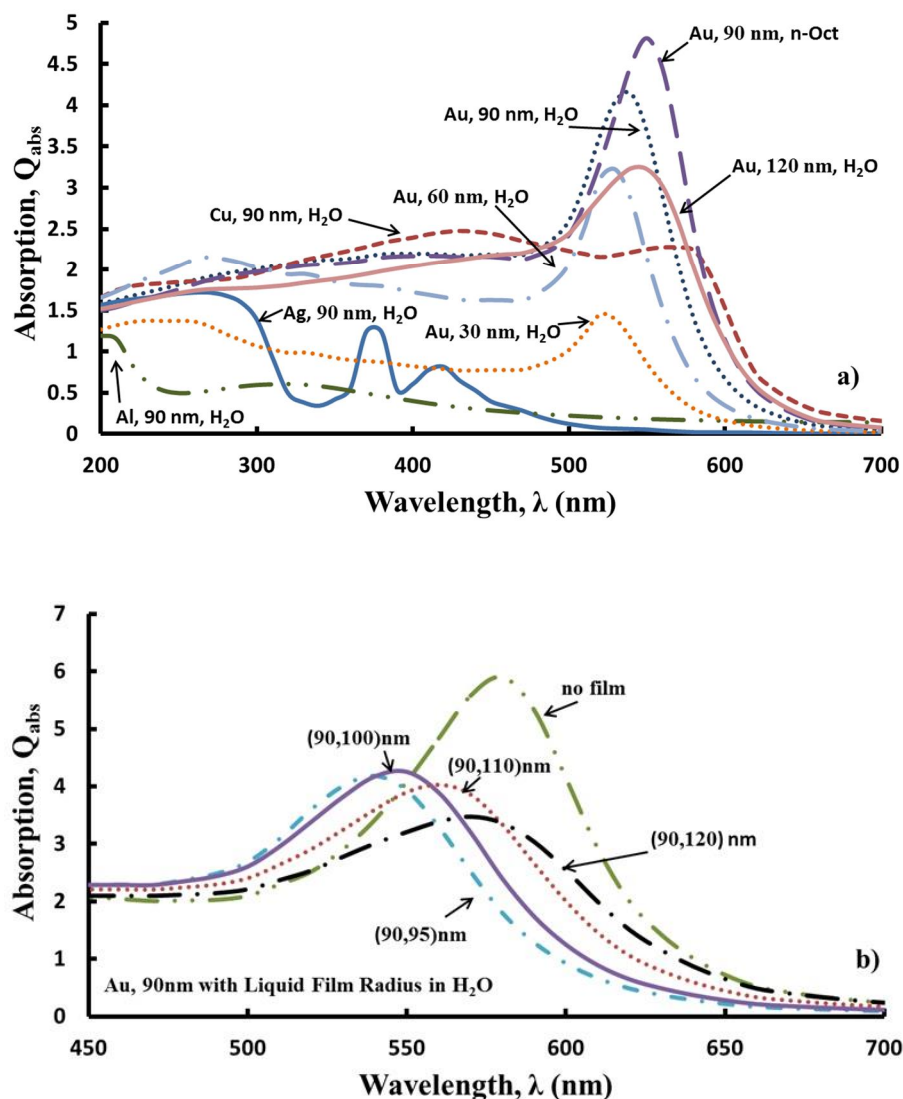


Figure 2.1.2: Absorption versus wavelength a) for a particle with varying composition, particle size, and medium; b) for a Au 90 nm particle with its surrounding liquid film. Note: (90,100) nm implies that the particle has a diameter of 90 nm and a surrounding film diameter of 100 nm.

Figure 2.1.2 gives an idea on how the absorption varies with different particle composition, size, medium, and also varying liquid film size around the particle. Figure 2.1.2a, shows how the absorption can be very different 1) for the various types of particles of a 90 nm particle, 2) the different sizes of a Au particle in

water, and 3) different mediums: water and n-octadecane. In Fig. 2.1.2b, a 90 nm Au particle was shown with varying sizes of liquid film surrounding the particle. The term (90,100) implies a 90 nm diameter particle with a film diameter of 100 nm. Notice that when a liquid film is added to a 90 nm particle, the particle absorption decreases as the size of the film increases.

Metallic particles, particularly Au nanoparticles, are considered to contribute to biomedical applications such as photothermal therapy [47–52] and imaging [53,54], and solar heating [55–57]. Neumann et al. [55,57] utilized the plasmonic effects for a solar based direct steam generation application. A vapor film was formed around a SiO_2/Au nanoparticle and due to buoyancy, the vapor bubble floats to the surface and steam escapes.

If PCMs such as water and paraffins are transparent in the visible region, the metallic nanoparticles of size 30, 60, 90, and 120 nm can be tuned to absorb the solar light in the visible region, increasing the temperature surrounding the nanoparticles faster because of the plasmonic effects and causing the liquid film to form. The temperature profiles of the film and the medium are tabulated. This chapter provides an in depth numerical investigation of a single nanoparticle composed of various metallic properties: Au, Ag, Cu, and Al subject to solar heating and experiencing phase change. Different mediums were also used: water and n-octadecane. Plasmonic properties were included in the analysis as well as the interface resistance between the particle and the film. A detailed mathematical

formulation is described in the next section followed by the numerical analysis and conclusions.

2.2 Nanoparticle mathematical formulation

The model used for the film formation is based on the derivations made from [58,59]. Initially the particle is in a solid medium heated through radiation. Once the temperature of the particle reaches the melting temperature, a film begins to form. At this stage, a velocity equation for the liquid film is necessary. This section provides the equations necessary to portray this process by giving the mass, momentum, and energy equations for the particle, liquid, and solid layers. Several assumptions were made such that there is a uniform surface temperature of the particle, thin liquid film compared to that size of the particle, and constant thermal properties within the films and the particle. Symmetry about the vertical axis for

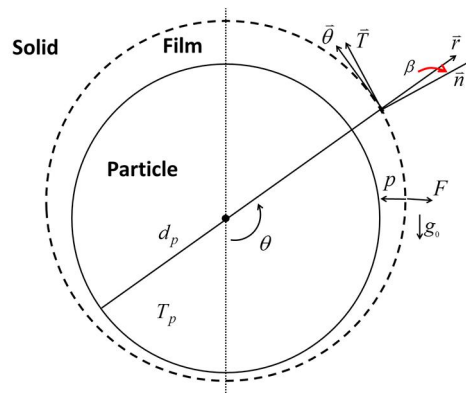


Figure 2.2.1: Film formulation of one nanoparticle.

the program is considered. For simplicity, the particle is stationary, and it is the medium around the particle that is changing. For this problem, a 2-D simulation in the radial coordinate, r , and polar direction, θ , is conducted. See Fig. 2.2.1 for details.

2.2.1 Energy equation for the particle

The particle is heated using lumped sum analysis heated through radiation, implying that the whole particle has a uniform temperature, T_p . The expression for the temperature of the particle is

$$\rho_p V_p c_p \frac{\partial T_p}{\partial t} = Q_{abs} \quad (2.2.1)$$

The particle density, volume, and heat capacity for the particle are defined by ρ_p [kg/m^3], V_p [m^3], and c_p [$J/kg \cdot K$]. The parameter, Q_{abs} [W], is the power absorbed from the small particle, based on Rayleigh scattering [46], such that

$$Q_{abs} = k \text{Im}(\alpha) I_{inc} = C_{abs} I_{inc} \quad (2.2.2)$$

where the wavenumber is k [m^{-1}], I_{inc} [W/m^2] is the incident intensity, and α is the polarizability. The parameter C_{abs} [m^2] is the absorption cross sections. Rayleigh scattering applies to spherical particles with a diameter smaller than the wavelength considered [46]. The electric field acts on the charged electrons in the particle which causes them to move at the same frequency and become a small

radiating dipole. The polarizability is the vector sum of the dipole moments in a unit volume and is defined by [47]:

$$\alpha = 3V_p \varepsilon_s \frac{\varepsilon_p - 1}{\varepsilon_p + 2} \quad (2.2.3)$$

where ε_p and ε_s are the permittivity of the particle and medium, respectively. See Appendix D.3 for more details. The permittivity of the particle must include the surface plasmon effects caused by the excitation of the electrons resulting from the interaction with photons on the surface of the metal as discussed earlier. Drude's model [47],

$$\varepsilon_p(\omega) = \varepsilon_\infty - \frac{\omega_{plasma}^2}{\omega(\omega + i\hat{\gamma})} \quad (2.2.4)$$

includes the plasma frequency, ω_{plasma}^2 [s^{-1}], ε_∞ is the bulk permittivity for the metal values which can be found using [60], ω [s^{-1}] is the frequency, and $\hat{\gamma}$ [s^{-1}] is the damping constant dependent on the Fermi velocity and the mean free path for the metal particle. Drude's model is a simplification of the Lorentz model for optical properties. This is derived by treating electrons as simple harmonic oscillators subject to a driving force of electromagnetic fields [46]. See Appendix D.4 for more details. For coated spheres, the polarizability changes to account for the material within the film where the subscript 1 represents the properties for inside the sphere, 2 represents the properties for the film, and 3 are the properties for outside the film [61].

$$\alpha = 3V_p \varepsilon_3 \left[\frac{\varepsilon_2 \varepsilon_a - \varepsilon_3 \varepsilon_b}{\varepsilon_2 \varepsilon_a + 2\varepsilon_3 \varepsilon_b} \right] \quad (2.2.5)$$

where

$$\varepsilon_a = \varepsilon_1 (3 - 2P) + 2\varepsilon_2 P$$

$$\varepsilon_b = \varepsilon_1 P + \varepsilon_2 (3 - P)$$

$$P = 1 - (d_1/d_2)^3$$

For other geometries like nanorods, the absorption cross section is generally found by using discrete dipole approximation developed by Draine and Flatau [62] or using Rayleigh Gans theory, which is an extension of Mie theory [46,63]. The parameters used for the two phases and the particle are provided in Tables 2.1 and 2.2.

Table 2.1: Particle Properties

Particle	Au	Ag	Cu	Al
ρ_p $[kg/m^3]$	19.32x10 ³	10.49x10 ³	8.94x10 ³	2.7x10 ³
c_p $[J/kg \cdot K]$	129	235	384	904
ω_p $[s^{-1}]$	2.18x10 ¹⁵	1.37x10 ¹⁵	1.69x10 ¹⁵	2.83x10 ¹⁵
\tilde{r} $[m^2 \cdot K / W]$	15x10 ⁻⁹	5x10 ⁻⁹	5x10 ⁻⁹	2.5x10 ⁻⁹
$\hat{\gamma}$ $[s^{-1}]$	6.42x10 ¹²	4.34x10 ¹²	4.03x10 ¹³	19.79x10 ¹²
\hat{k}_p $[W/m \cdot K]$	318	429	396	247
T_m $[K]$	1337	1235	1358	993

Table 2.2: Medium Properties

Medium	H ₂ O	n-octadecane
Solid		
ρ_s $[kg/m^3]$	917	814
c_s $[J/kg \cdot K]$	2050	2150
\hat{k}_s $[W/m \cdot K]$	2.22	0.358
ε_s	3.18	2.149
Liquid		
ρ_l $[kg/m^3]$	1000	744
c_l $[J/kg \cdot K]$	4216	2180
\hat{k}_l $[W/m \cdot K]$	0.68	0.148
ε_l	1.78	2.065
Other		
h_{sl} $[kJ/kg]$	334	244
a_0 $[m]$	1E-07	1.2E-11
$\Delta\gamma_o$ $[kg/s^2]$	0.0317	0.0096
T_m $[K]$	273	301
T_{crit} $[K]$	580	747

2.2.2 Energy equations for the solid and liquid medium

The energy equation for the film and outer medium in spherical coordinates is given by

$$\frac{\partial T_j}{\partial t} = \frac{\hat{k}_j}{\rho_j c_j} \left(\frac{\partial^2 T_j}{\partial r^2} + \frac{2}{r} \frac{\partial T_j}{\partial r} \right) \quad (2.2.6)$$

where the density, conductivity, and specific heat of the liquid/solid is described by $\hat{k}_j [W/m \cdot K]$, $\rho_j [kg/m^3]$, and $c_j [J/kg \cdot K]$, respectively. The subscript j references the particular layer. The parameter, T_j , is the temperature. The boundary condition at the particle/film interface incorporates an interface resistance, \tilde{r} [64], which is provided by

$$T = T_p - \frac{Q_{abs} \tilde{r}}{A_p} \quad (2.2.7)$$

The parameter, $A_p [m^2]$, is the surface area of the particle and $\tilde{r} [m^2 K/W]$ is dependent on the type of material the particle is in and is found in Table 2.1. Note: *these values represent the interface resistance for the particles in water. Values for n-octadecane have not been tabulated and therefore an assumption was made to use the same value.* The boundary condition at the film/medium interface is provided by

$$\frac{\partial T}{\partial r} = \frac{1}{\hat{k}_l} \frac{\partial m''}{\partial t} h_{sl} \quad (2.2.8)$$

Here, h_{sl} is the latent heat [J/kg]. The mass conservation at the bubble interface, is defined by

$$\frac{dm''}{dt} = \rho_l v_r \cos(\beta) + \rho_l v_\theta \sin(\beta) \quad (2.2.9)$$

where $\frac{dm''}{dt}$ [$kg/m^2 \cdot s$] is the area specific mass flux per unit area and β is the angle between the normal and radial coordinate, refer to Fig. 2.2.1. See Appendix B for the derivation of Eqn. (2.2.9). In Eqn. (2.2.9), v_r [m/s] is the radial velocity of the liquid film interface, and v_θ [m/s] is the polar velocity.

2.2.3 Liquid solid interface velocity equations

Once the temperature of the particle reaches the melting temperature, T_m , a liquid film develops between the particle and the solid medium. The interface velocity between the liquid film and the solid medium in the radial direction is satisfied by the equation

$$\rho_l \left(\frac{\partial v_r}{\partial t} + v_r \frac{\partial v_r}{\partial r} - \frac{v_r v_\theta}{r} \right) = \frac{3F}{4\pi d_{sl}^3} - \frac{\partial p}{\partial r} + (\rho_s - \rho_l) g_0 \cos \theta \quad (2.2.10)$$

The parameters $d_{sl}(t, r)$ [m] represent the diameter of the film. The term F [N] is the interfacial energies between the solid phase and liquid given by the Van der Waals forces similar to [33,34]

$$F = \pi d_p \Delta \gamma_0 \left(\frac{a_0}{a_0 + 0.5(d_{sl} - d_p)} \right)^2 \quad (2.2.11)$$

where d_p [m] is the diameter of the particle. The parameter $\Delta\gamma_0 = \gamma_{sp} - \gamma_{lp} - \gamma_{sl}$ where γ [kg/s²] is the interfacial energies between the solid/liquid, liquid/particle, and the solid/liquid interfaces. The parameter α_0 [m] is the molecular diameter of the two materials and $0.5(d_{sl} - d_p)$ represents the thickness of the liquid layer. For water $\alpha_0 = 0.10 \times 10^{-6}$ m and $\Delta\gamma_0 = 31.7 \times 10^{-3}$ kg/s² [65] and for n-octadecane, $\alpha_0 = 0.12 \times 10^{-10}$ m and $\Delta\gamma_0 = 9.6 \times 10^{-3}$ kg/s² [66]. The Van der Waal forces describe the force given by the molecular attraction between the molecules within each substance. See Appendix D.1 for more details. The change in pressure can be calculated using the Clausius-Clapeyron equation [67]

$$\frac{dp}{dr} = \frac{h_{sl}\rho_l}{T} \frac{dT}{dr} \quad (2.2.12)$$

This expression represents the influence of the external pressure on the melting solid. This implies that Eqn. (2.2.10) can be rewritten as

$$\rho_l \left(\frac{\partial v_r}{\partial t} + v_r \frac{\partial v_r}{\partial r} - \frac{v_r^2}{r} \right) = \frac{3F}{4\pi d_{sl}^3} - \frac{h_{sl}\rho_l dT}{T dr} + (\rho_s - \rho_l)g_0 \cos \theta \quad (2.2.13)$$

The polar interface velocity, v_θ , can be expressed by

$$\rho_l \left(\frac{\partial v_\theta}{\partial t} + v_\theta \frac{\partial v_\theta}{\partial \theta} - \frac{v_r v_\theta}{r} \right) = (\rho_s - \rho_l)g_0 \sin \theta \quad (2.2.14)$$

The buoyancy/gravitational effects are considered in both equations where $g_0 = -9.8$ m/s² is the gravitational acceleration.

2.2.4 Non-dimensionalized terms

After describing the mathematical model, non-dimensional equations were used to describe the equations found in Secs. 2.2.1-2.2.3. The following dimensionless parameters for the radial direction, time, temperature, radial velocity, polar velocity, and diameter of the film is defined as

$$R = \frac{2r}{d_p}, \quad \tau = t \frac{4\hat{\alpha}}{d_p^2}, \quad \Theta = \frac{T}{T_\infty}, \quad \hat{V}_r = \frac{d_p v_r}{2\hat{\alpha}}, \quad \hat{V}_\theta = \frac{d_p v_\theta}{2\hat{\alpha}}, \quad \phi = \frac{d_{sl}}{d_p} \quad (2.2.15)$$

Here $\hat{\alpha} = \hat{k}_l / \rho_l c_l$ [m²/s] is the thermal diffusivity. Equations (2.2.1)-(2.2.14) can be converted into the dimensionless governing equations:

The mass flow rate

$$\frac{d_p}{2\hat{\alpha}\rho_l} \frac{\partial m''}{\partial \tau} = \hat{V}_r \cos(\beta) + \hat{V}_\theta \sin(\beta) \quad (2.2.16)$$

The velocity interface equations between the liquid and solid mediums for the radial and polar direction, respectively, are

$$\begin{aligned} \left(\frac{\partial \hat{V}_r}{\partial \tau} + \hat{V}_r \frac{\partial \hat{V}_r}{\partial R} - \frac{\hat{V}_\theta^2}{R} \right) &= \frac{3d_p \Delta \gamma_0}{32\rho_l \hat{\alpha}^2 \phi^3} \left(\frac{a_0}{a_0 + 0.5d_p(\phi - 1)} \right)^2 - \frac{d_p^2}{4\hat{\alpha}^2} \frac{h_{sl} \partial \Theta}{\Theta \partial R} + \frac{(\rho_s - \rho_l)}{\rho_l} \frac{d_p^3}{8\hat{\alpha}^2} g_0 \cos(\theta) \\ \left(\frac{\partial \hat{V}_\theta}{\partial \tau} + \frac{\hat{V}_\theta}{R} \frac{\partial \hat{V}_\theta}{\partial \theta} - \frac{\hat{V}_r \hat{V}_\theta}{R} \right) &= \frac{(\rho_s - \rho_l)}{\rho_l} \frac{d_p^3}{8\hat{\alpha}^2} g_0 \sin(\theta) \end{aligned} \quad (2.2.17)$$

The film and solid temperature profile equations in non-dimensional form and boundary conditions are

$$\begin{aligned}
\frac{\partial \Theta_j}{\partial \tau} &= -\frac{\hat{k}_j}{\rho_j c_j \hat{\alpha}} \left(\frac{\partial^2 \Theta_j}{\partial R^2} + \frac{2}{R} \frac{\partial \Theta_j}{\partial R} \right) \\
\Theta &= \Theta_p - \frac{Q_{abs} \tilde{r}}{T_\infty A_p} \\
\frac{\partial \Theta}{\partial R} &= \frac{-\hat{\alpha} h_{sl}}{T_\infty \hat{k}_l} \frac{\partial m}{\partial t}
\end{aligned} \tag{2.2.18}$$

The non-dimensional equations for the particle temperature profile is given as

$$\frac{\partial \Theta_p}{\partial \tau} = \frac{Q_{abs}}{4 \rho_p c_p V_p T_\infty \hat{\alpha}} \tag{2.2.19}$$

2.3 Computational Analysis

The model described from Secs. 2.2.1-2.2.4 simulates the two stages for when a single nanoparticle in a solid medium is heated through radiation. Once the particle reaches melting temperature of the surrounding medium, a film begins to form surrounding the particle. The particle is initially surrounded by a solid medium. The medium and particle are considered to be the same temperature at $T_s = T_p = 270 \text{ K}$ and the reference temperature is $T_\infty = 383 \text{ K}$. Incident radiation is transparent to the solid medium, and the particle absorbs heat from the intensity of $I_{inc} = 1 \times 10^8 \text{ W/m}^2$. The absorption term is calculated for all frequencies in the solar range ($\lambda = 150 - 2000 \text{ nm}$). Properties of the materials used are found in Tables 2.1 and 2.2. The temperature profiles for the particle and for the solid medium are captured. When the temperature of the particle reaches the melting temperature of the medium, the velocity equations for the liquid film become nonzero, the film

diameter begins to grow, and the absorption term is recalculated using the new film diameter. The stopping criteria for these calculations is when the temperature of the particle reaches 89% of the critical temperature. At this temperature a vapor film maybe begin to develop [68]. This value was used to avoid a vapor phase change that might occur at this temperature.

In order to track the movement of the film, the level set method was used. This method, first introduced by Othian and Sethian [69], is a technique that relies on the implicit formulation of the interface given by a time dependent partial differential equation found in Eqn. (2.3.1). More information can be found in various texts including [70] and Appendix D.5. The equation used for the non-dimensional level set method is

$$\frac{\partial \phi}{\partial \tau} = \frac{\hat{V}_r + \hat{V}_\theta}{2} \quad (2.3.1)$$

The non-dimensional equations are calculated using the finite difference method for space and fourth order Runge Kutta method was used in time. For this simulation, the time and space steps are different for each stage. Vertical symmetry was assumed in the model. The Von Neumann stability criteria is considered for this program and is given by [71]

$$\frac{\hat{k}\Delta t}{\rho c \Delta r^2} \leq \frac{1}{2} \quad (2.3.2)$$

For the first stage before the temperature of the particle reaches the melting temperature of the liquid, T_m , the non-dimensional time step and space step are

$\Delta\tau_1 \approx 10^{-4}$ and $\Delta R \approx 10^{-2}$, respectively. The second stage when the liquid film begins to grow, the time step is $\Delta\tau_2 \approx 10^{-5}$, the space step in the liquid film is $\Delta R \approx 10^{-3}$, and space step in the solid medium is $\Delta R \approx 10^{-2}$. For these simulations $\Delta\theta \approx 0.39\text{rads}$. The finite difference method for the medium temperature is given by

$$\frac{\partial \Theta_{ii+1}^n}{\partial \tau} = \frac{\hat{k}_j}{\rho_j c_j \alpha} \left(\frac{\Theta_{ii}^{n+1} - 2\Theta_{ii}^n + \Theta_{ii}^{n-1}}{\Delta R^2} + \frac{2}{R} \frac{\Theta_{ii}^{n+1} - \Theta_{ii}^n}{\Delta R} \right) \quad (2.3.4)$$

where n is the space step in the r direction and ii is the time step.

2.3.1 Validation

No experimental data has been found at this time for this model. Therefore, this analysis was validated using several different methods depending on the expression. For the temperature of the particle, this is a simplistic ordinary differential equation and the solution to the non-dimensional Eqn. (2.2.19) is

$$\Theta_p(\tau) = \Theta_i + \tau \frac{Q_{abs}}{4\hat{\alpha}\rho_p V_p c_p T_\infty} \quad (2.3.5)$$

Figure 2.3.1 shows the validation using Eqn. (2.3.5) and the more rigorous algorithm using Eqns. (2.2.15-2.2.19) for a 90 nm particle in solid water with intensity 1×10^8 W/m². There is a difference because when using Eqn. (2.3.5), because only the solid properties and initial absorption coefficient was used throughout. The growth of the film was not accounted for and, therefore, the recalculation of the absorption, C_{abs} , is not incorporated.

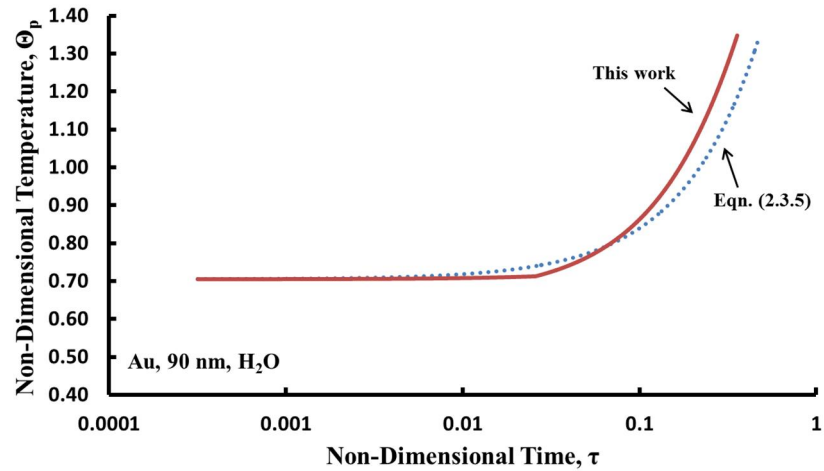


Figure 2.3.1: Validation for the particle temperature profile of a 90 nm Au particle in H₂O

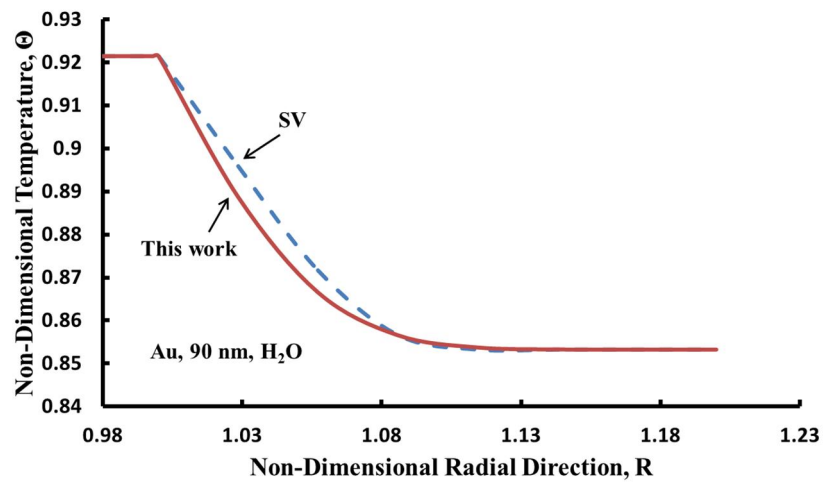


Figure 2.3.2: Validation of the medium temperature profile vs. the non-dimensional r direction for a 90 nm Au particle in H₂O using separation of variables (SV).

Another validation was used for the temperature profile of the medium using separation of variables (SV). Figure 2.3.2 gives the profile for a 90 nm particle in solid water medium vs. the non-dimensional radial direction, R . When $R=1$, the

temperature at the particle/medium interface is presented. When $R < 1$, the particle temperature is represented and when $R > 1$ represents the temperature of the medium. This shows it is a good expression for the calculations. The film and medium use the same expression and no other validations were necessary.

2.3.2 Numerical Results

This simulation captured many characteristics. First, the non-dimensional temperature profile for the particle, Θ_p , vs. the non-dimensional time, τ , is given in Fig. 2.3.3. Similar results were found within both mediums. Figure 2.3.3a compares the temperature profiles of the particle made up of different materials and sizes. These materials are in a H_2O medium and τ is displayed in logarithmic scale. The program was stopped when the particle temperature reaches 89% of the critical temperature which is about $\Theta_p = 1.38$ for water because a vapor layer may begin to develop at this temperature [68]. This graph shows that the Au particle heats up faster than the others with Cu, Ag, and Al follows. Figure 2.3.3a also conveys that when comparing different size particles, the larger the particle, the faster the particle heats up. Similar results are given for the other particle materials and the n-octadecane medium. The difference of the temperature profiles of the particles in the different mediums is also conveyed showing that a particle in n-octadecane heats up faster than when in water. Figure 2.3.3b implies that the particle will take a longer time to heat up with a lower intensity, which is accurate with Eqn. (2.2.19). The results of Fig. 2.3.3 are attributed to the absorption from the particles. A particle of size 30 nm has less absorption, compared to the particles of size 60-120

nm which have similar absorption spectrum, see Fig. 2.1.2a [39]. Also, the absorption of the Al nanoparticles is much less than that of Au and the absorption for a particle in n-octadecane is higher than water as seen in Fig. 2.1.2a. Based on this graph, a 120 nm Au particle in n-octadecane heats the fastest. However, these simulations stopped when another film, a vapor layer, may occur and possibly the particle may reach its melting temperature affecting its integrity. Choosing a particle where the integrity would not be affected but still heats up faster implies that a 90 nm or 60 nm particle works better.

Figure 2.3.4 gives insight on how the film radius is affected with particle properties and incoming heat. Figure 2.3.4a shows how the non-dimensional variable of the film diameter, ϕ , is varied by the material properties, size of the particle, and different mediums. The profile for ϕ follow similar paths when varying the compositions. Note that the ϕ values were taken at the bottom of the sphere. The difference due to gravity from the bottom of the particle to the top of the particle is about $\Delta\phi = 2 \times 10^{-6}$ and therefore considered negligible. Also, $\beta \approx 10^{-9}$ which implies the $\Delta\phi$ is small. For Au, Ag, Cu, and Al, the profiles are $\phi = 1.07, 1.45, 1.12, 1.62$ respectively, resulting in $d_{sl} = 96.3, 130.5, 100.8, 145.8$ nm respectively. This figure also shows that when the particle size is small, the film diameter grows larger in relation to the particle size. For the 30, 60, 90, 120 nm particles, the film diameter reaches $\phi = 1.90, 1.14, 1.07, 1.06$, respectively, which implies that the film diameter is $d_{sl} = 57, 68.4, 96.3, 127.2$ nm, respectively. Figure 2.3.4a also gives the film profiles for a 90 nm Au particle in both water and n-

octadecane. When the particle is in n-octadecane, the film diameter is much smaller than that of water. Figure 2.3.4b, gives an idea of how the film grows with intensity. The smaller the intensity the larger the film growth. To understand why these results occurred in Fig. 2.3.4, the particle with less heat or less absorption added resulted in the particle taking longer to heat and, in turn, allows for a larger film to grow. The Al particle has the least absorption, as well as the 30 nm particle and it resulted in a greater ϕ size. Having a larger film provides more thermal insulation to the incoming radiation, causing the particle to absorb less heat and it takes longer to reach the stopping temperature. This will further be shown in Fig. 2.3.5.

Figure 2.3.5 portrays the non-dimensional temperature profile for the particle, film, and surrounding medium vs. the non-dimensional “ r ” direction at specific times, τ . In this graph, the values where $R < 1$ implies the particle, $R = 1$ is the interface at the particle surface, and $R > 1$ implies the film and medium the particle is in. The first line in the legend represents time when the film has not yet developed. The other lines give an evolution of the temperature as the film grows. In this figure, arrows are used to show the interface resistance between the particle and film, \tilde{r} , and the film temperature profile. Figure 2.3.5a gives the profile for a 90 nm Au particle in water, Fig. 2.3.5b is the profile for a 90 nm particle in n-octadecane, Fig. 2.3.5c gives information for a Au 30nm particle in water, Fig. 2.3.5d gives information for a 90 nm Al particle in water, Fig. 2.3.5e gives information for a 60 nm Cu particle in n-octadecane, and lastly Fig. 2.3.5f gives information for a 90 nm Cu particle in n-octadecane. These figures were chosen arbitrarily. Based on Vera et al. [64], the temperature jump at the interface is huge

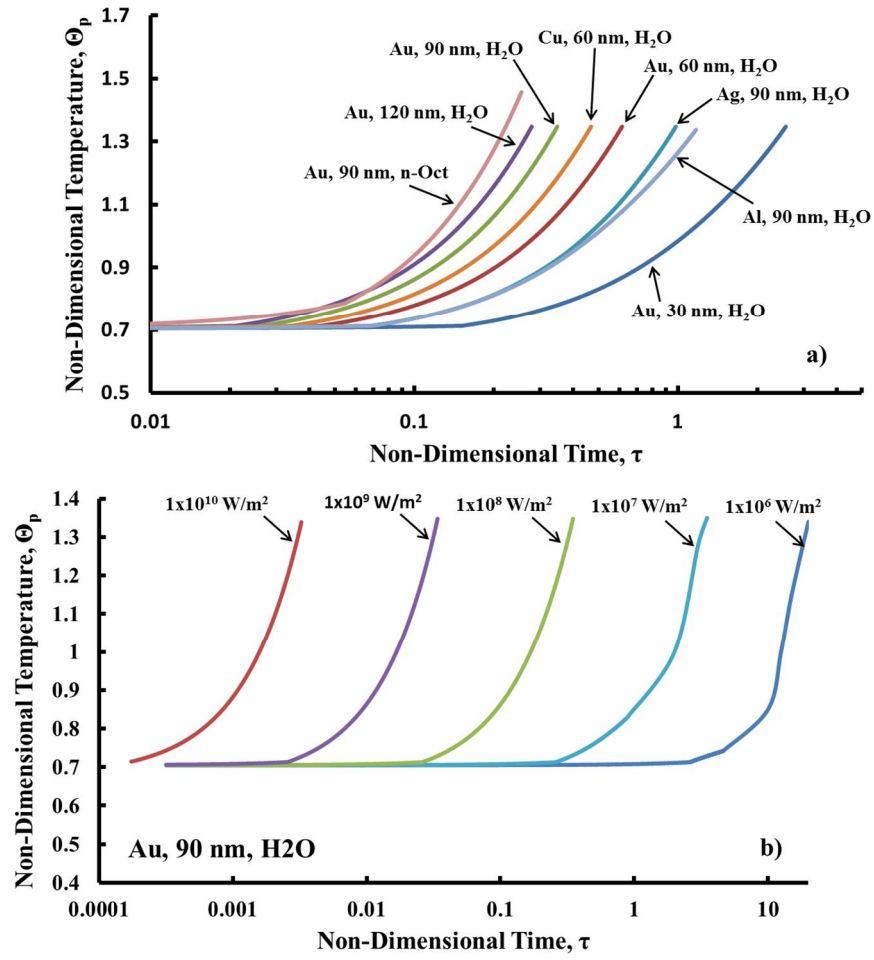


Figure 2.3.3: Temperature profile vs. time a) for various nanoparticle materials, sizes, and mediums b) a 90 nm Au particle in H₂O with different intensities.

for Au compared to the other particles, see Table 2.2, and is portrayed in Fig. 2.3.5.

This can be understood by viewing the relation used,

$$\Delta\Theta = \frac{Q_{abs}\tilde{r}}{A_p T_\infty} \quad (2.3.6)$$

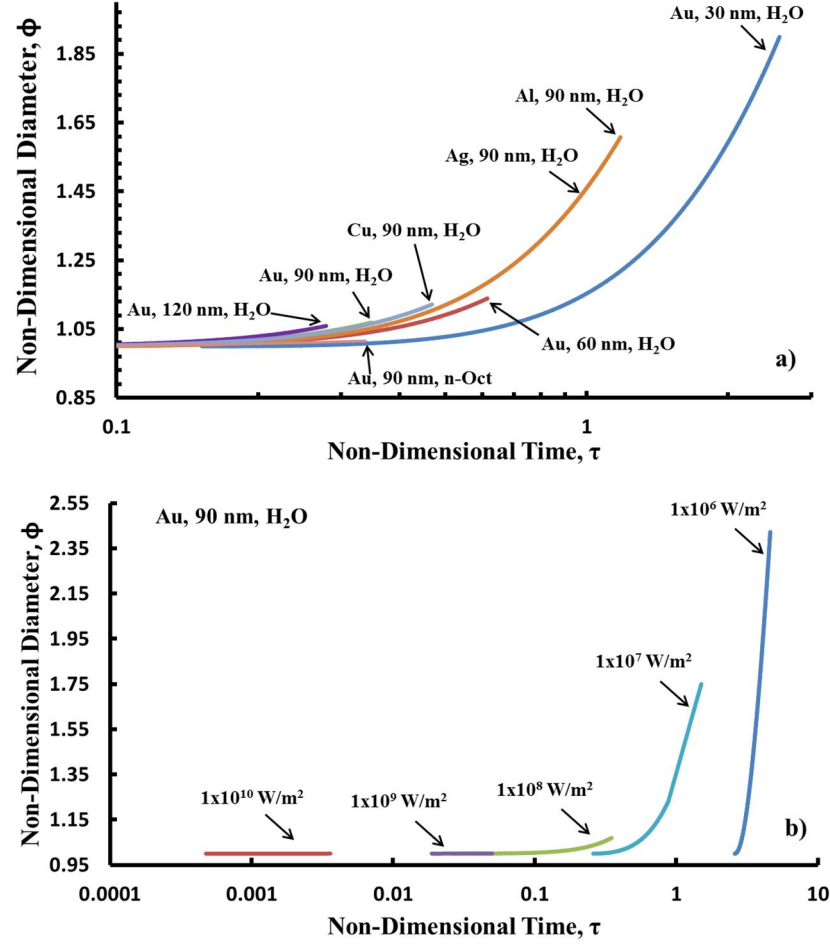


Figure 2.3.4: The liquid film diameter vs. non dimensional time a) for various nanoparticle properties b) for different intensities for a 90 nm Au particle in H₂O.

For gold, both Q_{abs} and \tilde{r} are larger than for the other particles resulting in a larger change in temperature for Au caused by the interface resistance. When changing

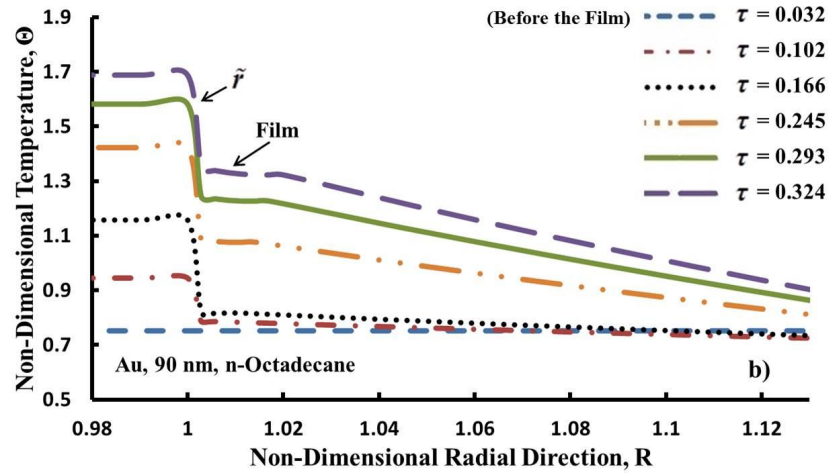
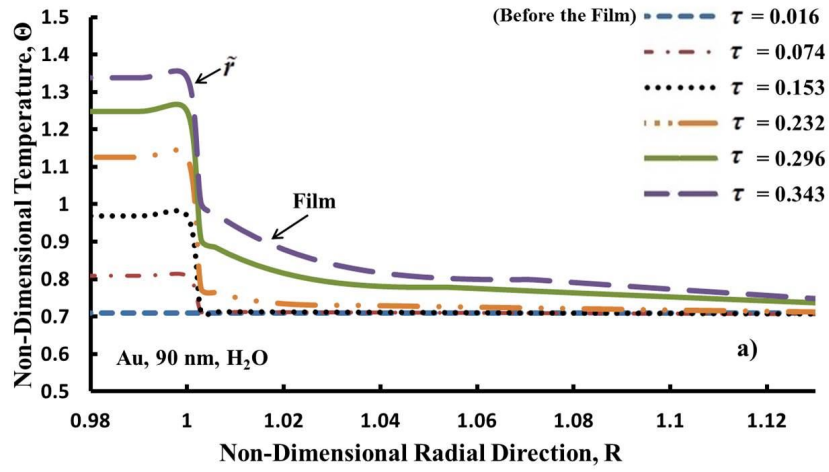
the size of the particle $\left. \frac{Q_{abs}}{A_p} \right|_{30nm} \leq \left. \frac{Q_{abs}}{A_p} \right|_{120nm}$ implies that the temperature jump for the

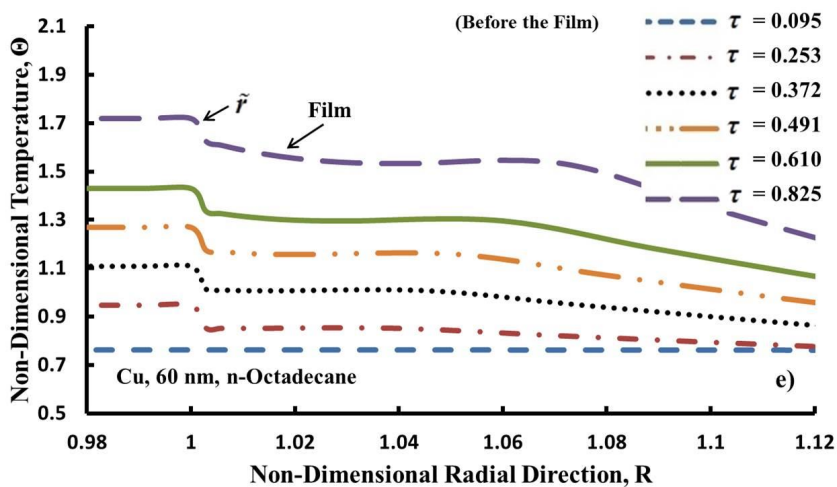
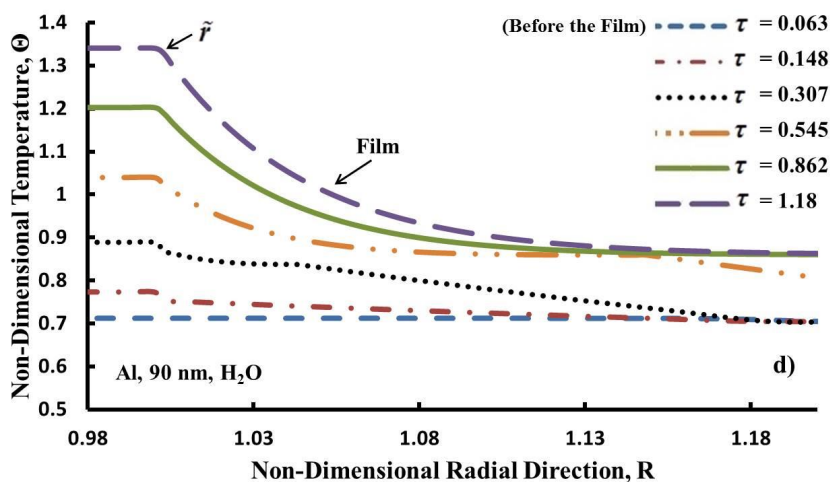
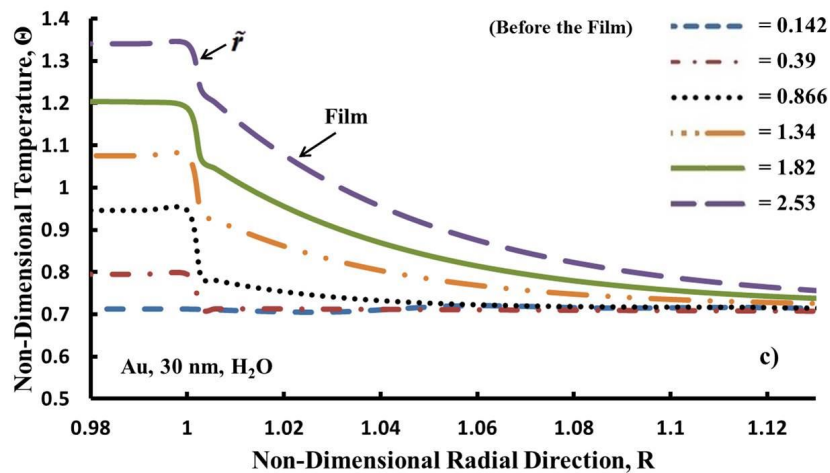
smaller particle is less than that of the larger particle. To further analyze the internal resistance at the surface of the particle, a temperature jump ratio is

established and derived here. Using Eqn. (2.2.1), the temperature change for the spherical particle heated by radiation is

$$\Delta\Theta_{particle} = \frac{Q_{abs}\Delta t}{T_{\infty}\rho_p c_p V_p} \quad (2.3.7)$$

At the interface, there is that thermal resistance as shown in Fig. 2.3.5 and Eqn. (2.3.6). The temperature jump ratio is defined as ratio of the temperature jump at the interface over the temperature jump of the particle:





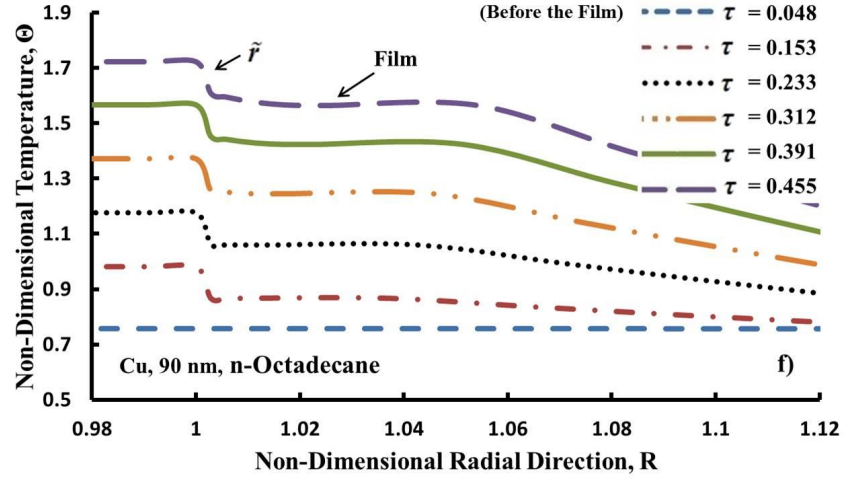


Figure 2.3.5: The temperature profile of the particle, film, and surrounding medium vs. τ for a) a 90 nm Au particle in H_2O b) a 90 nm Au particle n-Octadecane, c) a 30 nm Au particle in H_2O , d) a 90 nm Al particle in H_2O , e) a 60 nm Cu particle in n-Octadecane, and f) a 90 nm Cu particle in n-Octadecane.

Because the particle is spherical, the simplified expression is defined as

$$TJR = \frac{\rho_p c_p d_p \tilde{r}}{6\Delta t} \quad (2.3.9)$$

Notice that this ratio is dependent on time. This temperature jump occurs instantaneously, therefore, $\Delta t = 1 \times 10^{-9} s$. Also notice that this ratio is dependent on the type of the particle and the size of the particle. The physical interpretation of this ratio is describing the heat at the interface due to the heat flow of the particle caused by the incoming radiation from the particle. This ratio determines whether the particle resistance at the interface will be too large and whether it is necessary to include in the analysis. When the $TJR < 0.2$, the temperature jump due to the interface resistance, \tilde{r} , is small, refer to Fig. 2.3.5d. When the value is larger than 0.2, the temperature at the particle interface is large and should be included into the

analysis, refer to Fig. 2.3.5a. The value 0.2 was found by analyzing the results for all particles. Having a value of <0.2 implies that the temperature jump at the interface is <15 K.

There is also an additional temperature jump between the particle/film interface and the solid medium due to the film. The film acts as an insulation and for larger films, it results in a larger temperature jump. The total thermal resistance is calculated by:

$$\tilde{R}_{tot} = \tilde{R}_i + \tilde{R}_f = \frac{\tilde{r}}{\pi d_p^2} + \frac{\phi - 1}{4\pi \hat{k}_l \phi d_p} \quad (2.3.10)$$

Within this equation, the interface resistance is comparable to the resistance caused by the film.

In the field of thermal storage, high heat transfer rates are valued without affecting the structure of the particle, i.e. a larger temperature difference within a smallest time change. Based on Figs. 2.1.2 and 2.3.3-2.3.5, a compromise must be made dependent upon how fast the particle heats and how fast the medium heats. The heating of the medium depends on the particle/film interface and liquid film thermal resistances. A particle with a smaller film and \tilde{r} will heat the medium faster; however, the smaller the film, the faster the particle will reach the ending temperature and eventually may surpass the melting temperature of the particle. Because of this reasoning, Eqn. (2.3.10) can be utilized to calculate the total resistance for all combinations considered. The one with the smallest R_{tot} is the best for this application. A Cu particle of size 90 nm in n-octadecane is ideal for thermal storage. See Fig. 2.3.5 for a visual.

2.4 Conclusion

This work describes the characteristics to a single nanoparticle submerged into a phase change material. No other work had been concentrated on single nanoparticle analysis, only multiple nanoparticles in the PCM as a whole. The temperature profile of the particle and medium around the particle as well as the liquid film are analyzed for different material and size of nanoparticles submerged in two different mediums for various incident intensities. A few observations and conclusions are discussed below.

- The non-dimensional temperature profile for the particle is dependent on the plasmonic absorption. Al has less absorption and results in a longer time to heat. Similarly, a 30 nm particle has less absorption and also results in a longer time to heat in order to reach similar ending temperatures. These simulations stopped when a vapor film may develop and/or the integrity of the particle may be become affected.
- For the non-dimensional parameter of the liquid film, ϕ , the time it takes to reach a stabilized value differs depending on the type of particle used, the size of the particle, and the medium. Al takes the longest to develop a film and results in a larger ϕ with Au taking the least time and have the smallest film. The smaller the particle, the larger the relative film size. A medium of water showed larger film diameters when compared to n-octadecane. Having a larger film

provides more thermal insulation to the incoming radiation, causing the particle to absorb less heat and it takes longer to reach the stopping temperature.

- When decreasing the intensity of the particle, the film diameters of the liquid increase drastically. The lesser the intensity, the greater the impact there is on these parameters and the larger the films. This is because the film has more time to grow until the particle reaches the phase change temperature.
- The temperature profiles in the medium convey a temperature jump that occurs at the interface. This temperature jump depends on the particle type and size, as seen by the TJR . This interface resistance was found to be necessary to include when $TJR > 0.2$. There is also a resistance due to liquid film. When the film is larger, this temperature jump is more pronounced. The total resistance caused by the film and interface is found by Eqn. (2.3.10). The thermal storage application desires a particle with least total resistance (both interface and caused by the film).

This chapter considers solar heating with a range of wavelengths in the visible range. When discussing this chapter, stopping criteria for the simulation was that the temperature of the particle reaches 89% of the critical temperature because a vapor film may begin to form and cause an additional resistance. More research should be conducted when the vapor film may begin to form. Based on the results a Cu particle of size 90 nm in n-octadecane is ideal for thermal storage.

2.5 List of Variables

A	Surface Area (m ²)
a_o	Molecular diameter (m)
C_{abs}	Cross section (m ²)
c	Specific heat (J/kg K)
d	Diameter (m)
F	Interfacial force (N)
g_o	Gravitational acceleration (m/s ²)
h_{sl}	Latent heat of fusion (J/kg)
I_{inc}	Intensity (W/m ²)
k	Wavenumber (m ⁻¹)
k_B	Boltzmann constant (m ² kg/s ² K)
\hat{k}	Thermal Conductivity (W/m K)
m''	Mass flow rate (kg/m ² s)
\bar{n}	Normal direction (m)
P	Polarizability constant

p	Pressure (kg/m s ²)
Q_{abs}	Absorption radiation (W)
\tilde{R}	Resistance (K/W)
\tilde{r}	Interface Resistance (m ² K/W)
r	Radial direction (m)
T	Temperature (K)
t	Time (s)
\bar{T}	Tangential direction
V	Volume (m ³)
v	Velocity (m/s)

Greek Symbols

α	Polarizability
$\hat{\alpha}$	Thermal Diffusivity (m ² /s)
β	Vector between the normal and radial direction
$\hat{\gamma}$	Damping term (s ⁻¹)
ε	Permittivity
ε_{∞}	Permittivity of the bulk particle

κ	Absorption index
λ	Wavelength (m)
σ	Absorption coefficients (m ⁻¹)
ϕ	Volume Fraction
$\bar{\theta}$	Polar direction
ω	Frequency (s ⁻¹)

Subscript

<i>crit</i>	Critical value
<i>f</i>	Film
<i>ii</i>	Step in time direction
<i>i</i>	Interface
<i>j</i>	Type of nanoparticles
<i>l</i>	Liquid
<i>m</i>	Melt
<i>n</i>	Step in the r direction
<i>p</i>	Particle
<i>plamsa</i>	Plasma

r	Radial direction
s	Solid
sl	Solid/liquid interface
tot	Total

Non-Dimensional Variables

R	Radial direction
τ	Time
Θ	Temperature
\hat{V}	Velocity
ϕ	Film diameter
TJR	Temperature jump ratio

Chapter 3

Analysis of a Nanofluid Exposed to Radiation

3.1 Introduction

Fluids, such as water and ethylene glycol, with relatively low thermal conductivity cannot reach the high temperatures needed for thermal engineering devices. Introducing a small amount of suspended colloids of about 1-100 nm in size into fluids can improve the thermal properties and be able to absorb more heat. In 1995, Cho [72] was the first to present this idea of a nanofluid using millimeter to micrometer sized metallic particles and showed how the thermal conductivity improved. Since then, many researchers have experimentally and numerically investigated the different enhancements and provided mathematical approximations in order to define the thermophysical properties such as specific heat, thermal conductivity, density, and viscosity of those fluids [73]. They have also

been utilized in a variety of applications like cooling electronics, heat exchangers, medical applications, fuel cells, nuclear reactors, etc. [74].

Solar energy has become an increasingly popular field. Because of the rise in price of fossil fuels, researchers are motivated to find alternatives. Nanofluids have also been studied to find improvements in solar collectors, thermal storage [16,17], direct absorption steam generation [55–57], and solar stills. A review of these solar energy applications can be found in [75,76]. Within these applications, the use of the incoming solar radiation is converted into heat and transferred to a fluid flowing through the collector. This energy that was collected from the fluid is then stored in a thermal energy tank and can be used in the evening or during an overcast day. Tyagi et al. [77] provided a base model for a direct absorption collector with low-temperature aluminum/water nanofluid. It was found that there was an increase in the collector efficiency because of the increase in attenuation of sunlight passing through the collector caused by the nanoparticle addition. Also, they found that there was a slight increase in efficiency as the particle size grew; however, particle size was tested only up to 20 nm. Nanofluids containing carbon nanotubes, graphite, or silver in water were investigated both experimentally and numerically for a direct absorption solar collector by Otanicar et al. [78]. This showed that adding a small amount of these particles increases the efficiency substantially until the volume fraction is about 0.5% and it levels off. In [78], it was also shown that increasing particle size, the efficiency of the collector decreases unlike the results in [77]. Taylor et al. [79] studied optical properties of graphite, silver (Ag), copper

(Cu), gold (Au), and aluminum (Al) nanoparticles in Therminol VP1 for the use in direct absorption collectors. It was shown that about 95% of the solar light can be absorbed in nanofluids with fluid height ≥ 10 cm and low volume fractions of less than 1×10^{-5} . They found that based on the price of the raw materials, graphite and/or aluminum are better to use. In [80], Taylor et al. also studied the use of nanoparticles and black dyes in steam generation studies, showing up to a 50% increase in vapor generation compared to just water. Lenert et al. [81] experimentally and numerically optimized the effect of solar concentration and nanofluid height using carbon coated cobalt nanoparticles in Therminol VP-1. It was shown that the efficiency increased with increasing height and incident solar flux. Saidur et al. [82] tests the absorption and scattering enhancements of the nanofluid dependent on the light length path, diameter, and concentration of aluminum and water nanofluid. Yousefi et al. [83,84] experimentally explored the efficiency of $\text{Al}_2\text{O}_3/\text{H}_2\text{O}$ and multi-walled carbon nanotubes (MWCNT)/ H_2O nanofluid of a flat plate collector. It was found that the efficiency of the collector with 0.2% wt.% $\text{Al}_2\text{O}_3/\text{H}_2\text{O}$ nanofluid was higher than compared to 0.4% wt.%. Also if used the surfactant, Triton X-100, instead of water, there was a 15.63% enhancement. For the MWCNT/ H_2O without surfactant nanofluid increased for 0.4% wt.% whereas with 0.2 wt.% the efficiency reduces compared to just water as the working fluid. Won Lee et al. [85] and Zhang et al. [86] studied the effects that graphene oxide water nanofluid has on the critical heat flux. Both remarked that one of the reasons why the critical heat flux was enhanced was because of the increase in wettability.

Recently carbon nanohorns, which have large surface area, have been used to improve the optical properties for direct absorbers in [87]. Nanofluids in other tubular solar collectors [88,89] and parabolic solar collectors [90] were also investigated.

3.1.1 Absorption Properties of Nanoparticles

Metallic particles suspended in a fluid have unique characteristics when interacting with photons. The use of metallic nanoparticles has been thoroughly studied by mechanical engineers, biologists, physicists, and chemists because of their unique, tunable absorption and scattering properties. These metallic particles, such as gold (Au), copper (Cu), and aluminum (Al), when interacting with an electric field, create strong optical resonances called surface plasmon resonances (SPR). On the surface of these metal structures, a collection of bound mobile electrons generate quantized waves or plasmons. These bound electrons excite from their equilibrium position and oscillate when the frequency of the incident light is in tune with their motion, refer to Fig. 3.1.1.

Properties for Au, Cu, and Al were found using [60,91]. The surface plasmon resonances combined with the size, shape, and composition alters the sensitivity and tunability of the optical properties [36,37]. The diameter of the solid nanosphere shifts the SPR as well as the composition of the metal. The SPR peak shifts throughout the visible range depending on the composition of the particle. In

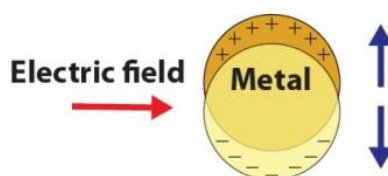


Figure 3.1.1: An electric field exposed to a metal nanoparticle results in an oscillation of the particle

addition to changing the physical components of the metallic nanoparticle, the particle absorption is extremely sensitive to changes in the medium that the particles are in [45]. See Fig. 3.1.2a to see how the SPR peak shifts when changing material properties. As you can see from Fig. 3.1.2b, the absorption peak shifts slightly to the right as the particle size gets larger. Mie theory is a solution to Maxwell's equations for a sphere providing the scattering and absorption coefficients [46]. MATLAB functions for Mie scattering and absorption can be found in Sec. 3.2.1 [92]. Also, see Appendix D.7 for the code. To account for the plasmonic effects at a particular frequency, Drude's model or the Drude-Lorentz model is used. More information about calculating the absorption and scattering of the nanoparticles can be found in Sec. 3.2.1 and in Appendix D.3, D.4, and D.7. The solid nanosphere, nanoshell, nanorod, nanocage, nanobelt, and nanohezapod structures are a few of the metallic particle shapes that have been created and tested. More information on plasmonic nanoparticles and the various shapes that have been considered can be found [39,40,43]. Metallic particles, particularly Au

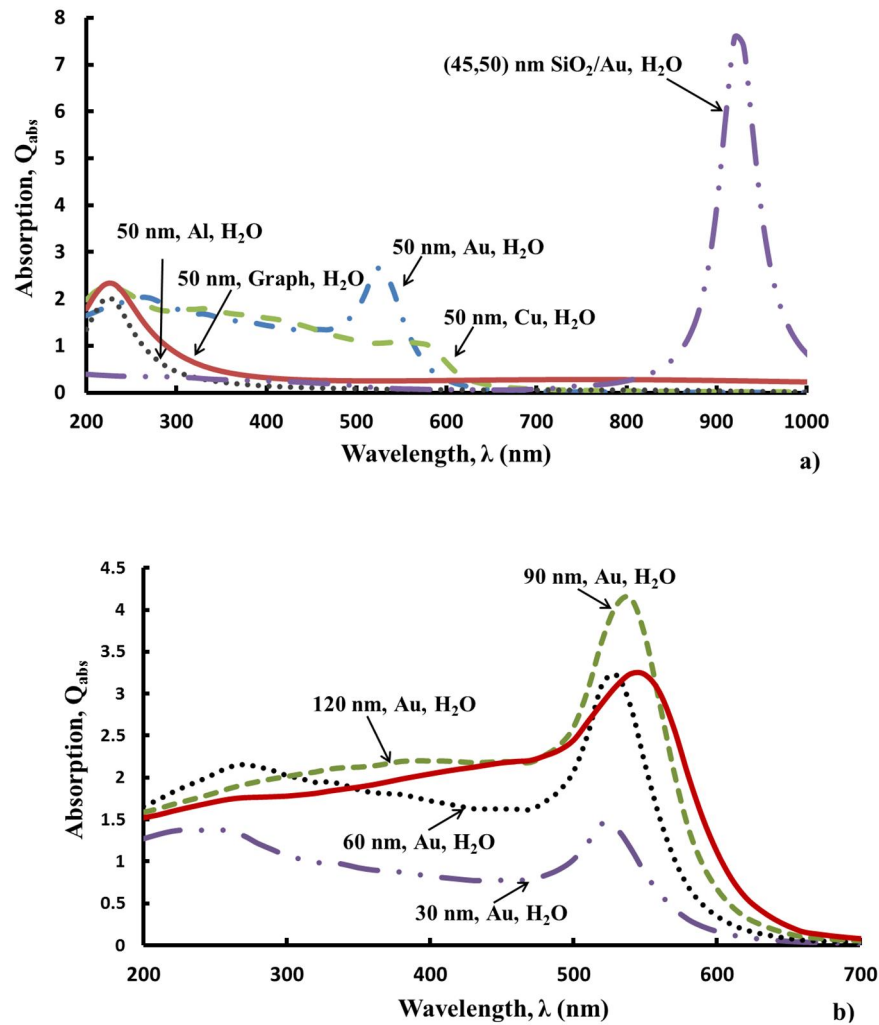


Figure 3.1.2: Absorption curves for a) each different type of particle with diameter of 50 nm in water b) different Au particle diameters in water.

nanoparticles, are considered to contribute to biomedical applications such as photothermal therapy [47–52] and imaging [54], and solar heating [55–57,93]. A review on optical properties of nanofluids is given by Hossain et al. [94].

Nonmetal nanoparticles, such as carbon based particles, are becoming increasingly interesting in the field of material sciences. Carbon based

nanomaterials include nanographene sheets (NGS) [95], graphite which are stacked graphene sheets, single walled carbon nanotubes (SWNTs) [96], and multiwalled carbon nanotubes (MWNTs) [97], and fullerenes. Carbon nanomaterials such as NGS and carbon nanotubes (CNTs) have unique properties such as mechanical stiffness, photostability, and high thermal and electrical conductivity. NGS have an array of carbon atoms arranged in a honeycomb lattice structure as defined by sp^2 bonding [95]. These structure are used as semiconductors and nanocomposites in electrical devices [98,99] and are currently being tested for biomedical applications [100,101]. SWNTs are 3D shaped long and thin tubes of sp^2 carbon atoms that resemble a rolled up nanographene sheet. Graphite can be thought of as a hexagonal structure of carbon. When determining the absorption in graphene and SWCTs, the optical absorption comes from two distinct types of contributions: the interband and intraband contributions [95]. Interband transitions are the interaction between the conduction and valence bands. Intraband transitions are the relationship between the quantized levels within the conduction or valence bands. For the far-infrared region, the optical absorption is influenced by the intraband transitions. More information on calculating the absorption is found in Sec. 3.2.1.

Researchers mainly worked on research using only one type of nanoparticle within the fluid and do not utilize the whole absorption spectrum. A review of other researchers that have considered using a hybrid nanofluid for various applications not exposed to radiation is found in [102]. A hybrid nanofluid is a nanofluid with more than one type of particle within the base fluid, is found in [102]. No one has

yet to consider the plasmonic properties caused by the hybrid fluid when exposed to radiation.

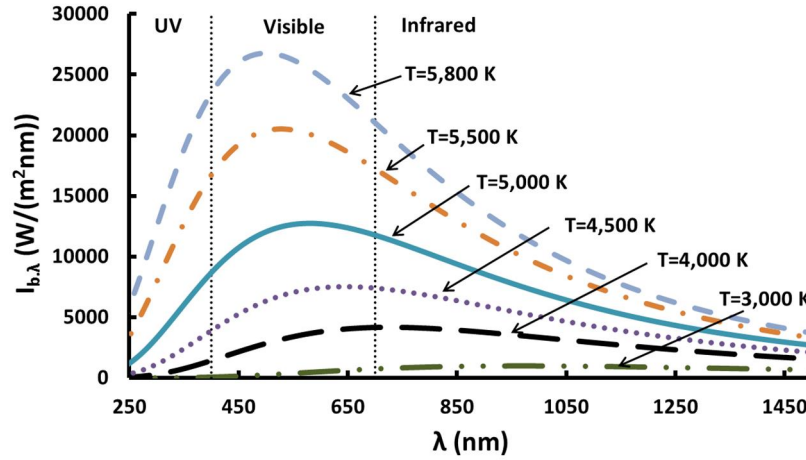


Figure 3.1.3: The spectrum for radiation at different temperatures. Recalculated using the spectral blackbody intensity equation, Eqn. (3.2.1)

Figure 3.1.3 shows the spectral irradiance for different temperatures calculated using the spectral blackbody intensity equation, Eqn. (3.2.1). Solar radiation is considered for when $T=5,800$ K. In viewing Fig. 3.1.3, approximately 40% of the energy emitted from the sun is in the visible range (400-700 nm) [103] and the other parts consist of the infrared and the ultraviolet range. For various other temperatures the structure of the graph shifts. This paper presents two methods in optimizing which mixture of particles should be used within the ‘hybrid’ nanofluid for a given temperature and wavelength range. The first method is based on viewing graphs describing the relationship of the SPR peaks and diameters for each particle type and also uses the fraction of emissive blackbody charts found in

radiation books. The second method is an algorithm which provides a more accurate optimized method for this hybrid solution where concentrations, height of the container, and number of types of particles within the mixture are considered. The chapter ends with a few observations of finding the correct optimization for the hybrid mixture.

3.2 Hybrid construction

A pictorial idea of a solar collector model is presented in Fig. 3.2.1 to give an idea of the mathematical model provided. A nanofluid between an adiabatic surface and a transparent glass is heated through convection and radiation. Tyagi et al. [77] provided a base numerical model of a direct absorption receiver that utilizes nanofluids. A nanofluid is contained between a transparent glass surface and an adiabatic surface heated by solar radiation is described in [77,78,81,82]. In Fig. 3.2.1, H is height, $L = 1\text{ m}$ is the length, and the radiative heat flux is q_r . The fluid is considered to be stagnant. The blackbody intensity radiation is calculated by, $I_{b,\lambda}$ [W/m^2], defined by [103]

$$I_{b,\lambda}(\lambda, T) = \frac{2hc_0^2}{\lambda^5 \left[\exp\left(\frac{hc_0}{\lambda k_B T}\right) - 1 \right]} \quad (3.2.1)$$

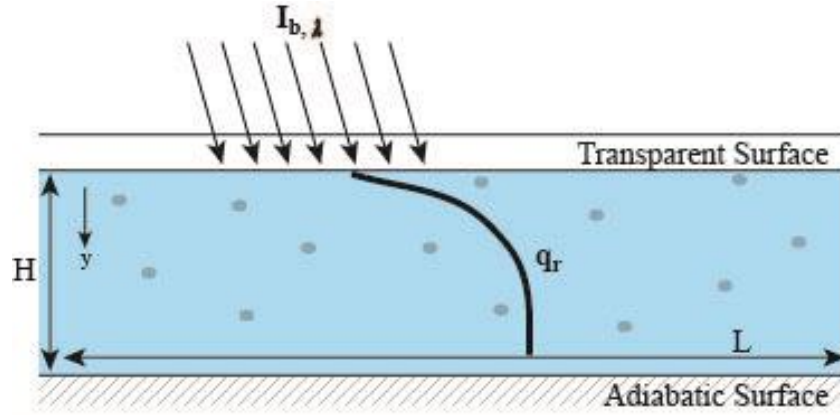


Figure 3.2.1: Solar heating of a nanofluid

In this expression, $h = 6.626 \times 10^{-34} \text{ J} \cdot \text{s}$ is Planck's constant, $c_0 = 3 \times 10^8 \text{ m/s}$ is the speed of light in a vacuum, $k_B = 1.38 \times 10^{-23} \text{ m}^2 \text{kg} / \text{s}^2 \text{K}$ is Boltzmann's constant, λ [m] is the wavelength, and T [K] is the temperature. The intensity is assumed to be isotropic with no in-scattering term. The direction of the intensity is only in the y -direction because the x -direction is considered infinitely long [103]. The intensity expression is given by

$$\frac{\partial I_\lambda}{\partial y} = -\sigma_{abs,\lambda} I_\lambda \quad (3.2.2)$$

where $\sigma_{abs,\lambda} = \sigma_{abs,\lambda,f} + \sigma_{abs,\lambda,p,tot}$ is the absorption for the fluid and particles and described later. Equation (3.2.2) describes the spectral intensity involving the absorption of the nanofluid. The boundary conditions at the top of the container is defined by Eqn. (3.2.1)

$$I_\lambda(y=0) = I_{b,\lambda} \quad (3.2.3)$$

In these applications, the highest absorption of incoming heat is desired; therefore, the expression that is optimized is given by

$$\left(\sigma_{abs,\lambda,f} + \sigma_{abs,\lambda,p,tot} \right) I_{b,\lambda} \quad (3.2.4)$$

The absorption term for a pure fluid, $\sigma_{abs,\lambda,f}$, is the attenuation coefficient used in the Beer-Lambert law [77]

$$\sigma_{abs,\lambda,f} = \frac{4\pi\kappa}{\lambda} \quad (3.2.5)$$

where κ is the absorption index. Values for κ are found in [104,105]. The ‘hybrid’ nanoparticle absorption coefficients are defined using

$$\begin{aligned} \sigma_{abs,\lambda,p,tot} &= \sum_j \sigma_{abs,\lambda,p,j} = \sum_j \frac{6\phi_j C_{abs,\lambda,j}}{\pi d_j^3} \\ \phi_{tot} &= \frac{\sum_j n_j V_{p,j}}{\sum_j n_j V_{p,j} + V} = \sum_j \phi_j \end{aligned} \quad (3.2.6)$$

The parameter, ϕ_{tot} is the total volume fraction of the particles due to the total volume of the fluid and particles, d [m] is the diameter of the particles, n is the amount of each type of particle, V_p and V [m³] are the volume of the particle and fluid, respectively, and $C_{abs,\lambda,j}$ [m²] is the cross section for each particle [46,103] described in Sec. 3.2.1. In the ‘hybrid’ nanofluid, there are distinct volume fractions, diameters, and absorption cross sections for each material. The summation part in Eqn. (3.2.6) includes the summation of all the properties over the number of particle

types, j . The radiative heat flux is determined by integrating the intensity over all possible directions and wavelengths as shown

$$q_r = 4\pi \int_{\lambda} I_{\lambda} d\lambda \quad (3.2.7)$$

3.2.1 Absorption Analysis of Nanoparticles

To calculate the absorption, Q_{abs} , Rayleigh scattering [46] was used

$$Q_{abs} = \frac{C_{abs,\lambda}}{\pi \left(\frac{d}{2}\right)^2} = \frac{k \operatorname{Im}(\alpha)}{\pi \left(\frac{d}{2}\right)^2} \quad (3.2.8)$$

where the wavenumber is $k [m^{-1}]$ and α is the polarizability. Rayleigh scattering applies to spherical particles with a diameter smaller than the wavelength considered [46]. The polarizability, α , describes the polarization between two dielectric constants from two different medias as shown [46]:

$$\alpha = 3\varepsilon_f V_p \frac{\varepsilon_p - \varepsilon_f}{\varepsilon_p + 2\varepsilon_f} \quad (3.2.9)$$

where ε_p and ε_f are the permittivity of the particle and medium, respectively. See Appendix D.3 for more information on the polarizability. The permittivity of the particle must include the surface plasmon effects caused by the excitation of the electrons due to the interaction with photons on the surface of the metal as discussed in Sec. 3.1.1. For the metallic particles, Drude's model describes the particle permittivity [46],

$$\varepsilon_p(\omega) = \varepsilon_\infty - \frac{\omega_{plasma}^2}{\omega(\omega + i\hat{\gamma})} \quad (3.2.10)$$

where the plasma frequency is represented by ω_{plasma} [s^{-1}], ε_∞ is the bulk permittivity for the metal which values can be found using [60], ω [s^{-1}] is the frequency, and $\hat{\gamma}$ [s^{-1}] is the damping constant. Drude's model is a simplification of the Lorentz model for optical properties. This is derived by treating electrons as simple harmonic oscillators subject to a driving force of electromagnetic fields [46]. See Appendix D.4 for more details. For nanoshells, the polarizability changes to account for the material within the shell where ε_1 represents the permittivity for inside the sphere, ε_2 is the permittivity for the shell, and ε_3 is the property for outside the particle [61,106]. The polarizability for a nanoshell is

$$\alpha = 4\pi\varepsilon_3(d_2/2)^3 \left[\frac{\varepsilon_2\varepsilon_a - \varepsilon_3\varepsilon_b}{\varepsilon_2\varepsilon_a + 2\varepsilon_3\varepsilon_b} \right] \quad (3.2.11)$$

where

$$\begin{aligned} \varepsilon_a &= \varepsilon_1(3 - 2P) + 2\varepsilon_2P \\ \varepsilon_b &= \varepsilon_1P + \varepsilon_2(3 - P) \\ P &= 1 - (d_1/d_2)^3 \end{aligned}$$

For other geometries like nanorods, the absorption cross section is generally found by using discrete dipole approximation developed by Draine and Flatau [62] or using Rayleigh Gans theory, which is an extension of Mie theory [46,107]. More

information can be found [63]. Only spherical particles are considered in this thesis.

Appendix D.7 gives the MATLAB code for calculating the absorption coefficients.

The Drude-Lorentz model accurately describes the particle permittivity for graphite and carbon nanotubes [108–110]:

$$\varepsilon_p(\omega) = 1 - \frac{\omega_p^2}{\omega(\omega + i\hat{\gamma})} + \sum_{s=1}^S \frac{\sigma_s^2}{\omega_s^2 - \omega^2 - i\omega\hat{\gamma}_s} \quad (3.2.12)$$

Where ω_s , σ_s , and $\hat{\gamma}_s$ are the transition frequency, oscillator strength, and decay rate for the Lorentz term [108]. To describe the permittivity accurately for graphite, it was shown experimentally that $S = 7$ [111]. The parameters for the Lorentz part of the equation are repeated from [108] and provided in Table 3.1.

Table 3.1: Decay rate, oscillator strenght, and transition energy for Eqn. (3.2.12)

S	$\hat{\gamma} \quad [s^{-1}]$	$\omega_p \quad [s^{-1}]$	$\sigma_s \quad [s^{-1}]$
1	2.4×10^{15}	1.12×10^{15}	6.56×10^{15}
2	3.93×10^{15}	6.62×10^{15}	7.89×10^{15}
3	2.43×10^{15}	6.78×10^{15}	1.25×10^{16}
4	1.53×10^{15}	2.19×10^{16}	5.48×10^{15}
5	3.30×10^{15}	2.14×10^{16}	2.22×10^{16}
6	1.51×10^{15}	2.49×10^{16}	2.27×10^{16}
7	1.28×10^{16}	3.26×10^{16}	9.19×10^{15}

3.3 Hybrid Optimization

There are many dependent variables to consider when optimizing a ‘hybrid’ nanofluid when exposed to radiation: T_{input} , λ , H , ϕ_{tot} , the number of particles types of particles in a mixture (N), and the materials available to create the database. Refer to Fig. 3.2.1 to understand that the H represents the height of the container in which the nanofluid is in. This section provides two methods on determining a hybrid nanofluid. The first method is using a set of graphs to determine which particles to consider in the nanofluid, the second method provides

a step by step algorithm for providing a more accurate way to determine which optimized mixture to use when exposed to radiation.

3.3.1 Method 1: Graphically determining a hybrid mixture

This section first describes information how to choose the different types of particles and the corresponding diameters for the hybrid mixture. The hybrid mixture can be found using the SPR peaks and the areas of Q_{abs} for each particle material and each diameter in the database. Figure 3.3.1 relates all of this information where Fig. 3.3.1a gives the diameter vs. the SPR peak for each material and Fig. 3.3.1b relates the diameter vs. the area of Q_{abs} . The materials considered were Au, Cu, Al, Graphite, and SiO₂/Au nanoshell with diameters ranging from $d=10-150$ nm. For the nanoshell, the shell thickness is 5 nm. This section also determines the percentage of concentration of how many particles to use of each material. The steps for this method is as follows:

- 1) Choose the input temperature, T_{input} , container height, H , number of particles to use, N , and concentration, ϕ_{tot} .
- 2) Use the input temperature and Fig. 3.13 to determine the structure of the blackbody intensity over a specific wavelength, $\lambda \in [\lambda_{min}, \lambda_{max}]$. This is important because the structure of $I_{b,\lambda}$ differs depending on the temperature and, as a result, the temperature changes the combination of which particles to use.

- 3) Based on N , visually determine the set of intervals of wavelength that contain a large amount of area within the intensity figure. The median within these intervals will represent the SPR peaks that should be chosen.
- 4) Using Fig. 3.3.1a, find the diameter(s) and material that correlates to the SPR peak found in step 3).
 - a) If there is only one diameter proceed to step 6)
- 5) Consider Fig. 3.3.1b and the diameters for the chose material found from step 4) to find the specific diameter and particle type with the highest area of Q_{abs} .
- 6) Find the percentage of concentration P_j , using the fraction of blackbody emissive power, $f(\lambda T_{input})$, from a radiation book [103,112]. In most radiation books, a chart is given in the appendix to calculate the fraction of emissive power from a wavelength range of 0- λ . You find P_j by
 - a) Determine the median between the different SPR peaks found from step 3).
 - b) Using the median of the SPR peaks found in step 6a) and the minimum and maximum wavelength, create an interval $[\lambda_{min}, median, \lambda_{max}]$.
 - c) Calculate P_j by referencing the chart from the radiation book and the interval found in step 6b) for each N .

$$P_j = \frac{f(\lambda_{j+1} T_{input}) - f(\lambda_j T_{input})}{f(\lambda_{max} T_{input}) - f(\lambda_{min} T_{input})} \quad (3.3.1)$$

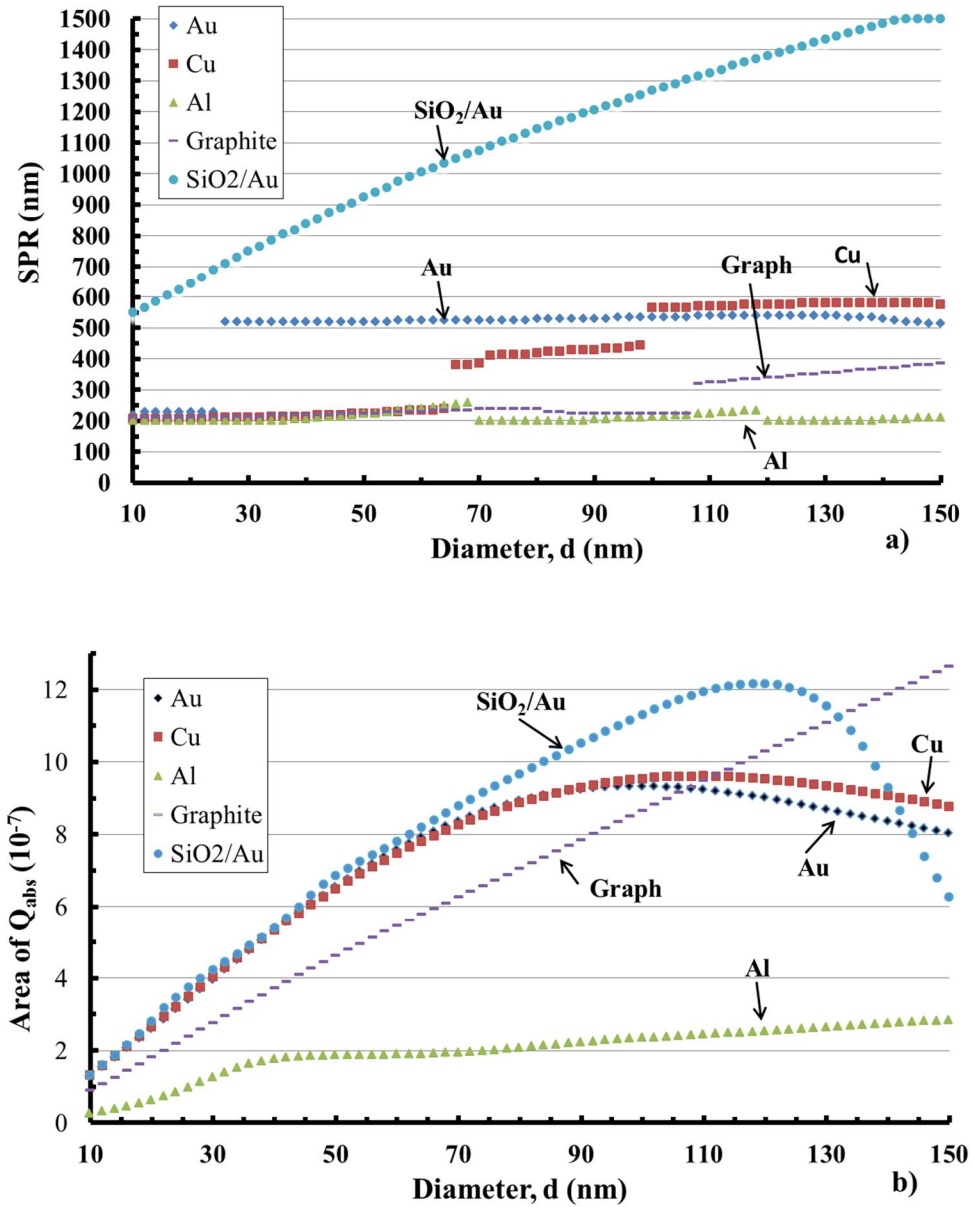


Figure 3.3.1: Presents the a) diameter vs. the SPR peak. b) diameter vs. the area of Q_{abs} for each particle type.

This method gives you the material, diameter of the particles, and percentage of the particle type for each N . An example can further explain how to use this technique. Choose $T_{input} = 5,800\text{ K}$, $N = 2$, and $\lambda = [\lambda_{min}, \lambda_{max}] = [200, 1000]\text{ nm}$.

Viewing Fig. 3.1.3, the peak of $I_{b,\lambda}$ lies within the range 400-600 nm. This implies that a particle that has an SPR peak within the observed range 400-600 nm should be considered. Also for this specific temperature and $N = 2$, a second particle with an SPR peak between the wavelength range 600-1000 nm would be advised. Using Fig. 3.3.1a, at an SPR peak of ~ 500 nm, Au particles with diameters of 25-150 nm should be considered. For the second interval, an SPR peak of ~ 700 nm implies a 30-35 nm SiO₂/Au particle would work. Because there is more than one diameter to choose from, view Fig. 3.3.1b. For the Au particle, the 90 nm diameter has highest area of Q_{abs} . For the SiO₂/Au particle the 35 nm particle would be advised. A similar process can be used for different values of T_{input} and N . To find the percentage of concentration, the fraction of blackbody emissive power can be utilized. Using median between the different SPR peaks and the wavelengths, $\lambda_{min} = 200nm$, $\lambda_{max} = 1000nm$, the interval is $[200,600,1000]nm$. Using Eqn. (3.3.1), then the percentage of the total concentration for the 90 nm Au particle and the 30 nm SiO₂/Au nanoshells is calculated by

$$\begin{aligned}
 P_{Au} &= \frac{f((600nm)5800) - f((200nm)5800)}{f((1000nm)5800) - f((200nm)5800)} = 0.52 \\
 P_{SiO_2/Au} &= \frac{f((1000nm)5800) - f((600nm)5800)}{f((1000nm)5800) - f((200nm)5800)} = 0.48
 \end{aligned}
 \tag{3.3.2}$$

This implies that 52% of ϕ_{tot} should be Au particles of 90 nm and 48% should be SiO₂/Au nanoshells with a diameter of 35 nm.

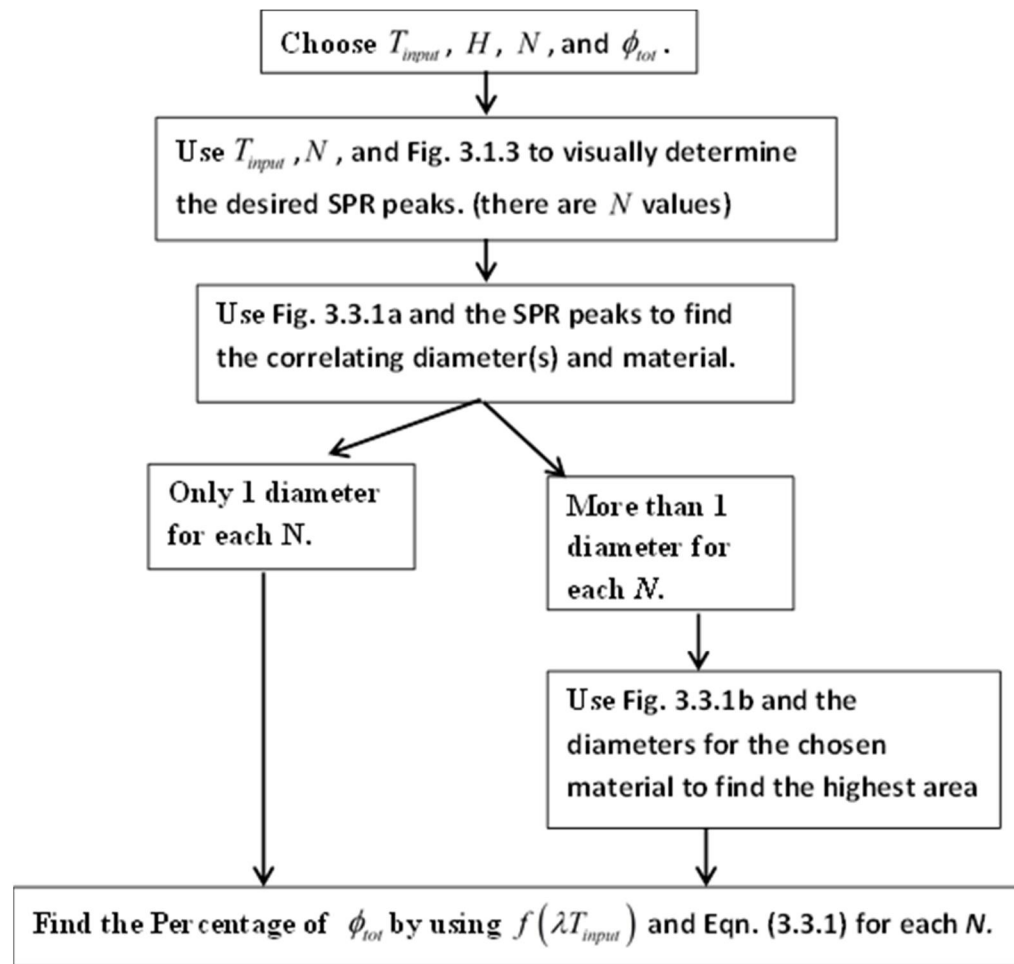


Figure 3.3.2: Flow chart describing Method 1 for choosing the hybrid nanofluid

Figure 3.3.1 gives information for five different particles materials. If access to this collection of materials is not available, then use the graphs to compare for the particular particles composition within your database. Note that at times, a hybrid mixture can compose of a single particle type with different diameters as an optimal choice of mixture. A flow chart for this method is given in Fig. 3.3.2. This section gave information on finding the correct particles compositions, diameter size, and

percentage of the type of particle when using a specific value of N and T_{input} . The same process can be duplicated for applying different values to these variables. An algorithm will be provided in the next section for a more accurate approximation that is presented here in this section.

3.3.2 Method 2: Algorithm determining a hybrid mixture

In this section, a numerical algorithm is provided for a more accurate recipe in determining the 'hybrid' mixture. Assume a given temperature, $T_{input} = 5,800 \text{ K}$, and wavelength range, $\lambda = [\lambda_{min}, \lambda_{max}] = [200, 1000] \text{ nm}$. Different heights, $H = [1.2 \times 10^{-5}, 1.2 \times 10^{-4}, 1.2 \times 10^{-3}, 1.2 \times 10^{-2}, 1.2 \times 10^{-1}] \text{ m}$, number of particle within the combination you wish to use, $N = [1, 2, 3, 4]$, and concentrations, $\phi = [1 \times 10^{-6}, 1 \times 10^{-5}, 1 \times 10^{-4}, 1 \times 10^{-3}, 1 \times 10^{-2}, 1 \times 10^{-1}]$, were considered. The following steps were taken:

- 1) Create a database by finding the absorption, Q_{abs} , over your desired wavelength range, using Eqns. (3.2.8-3.2.12), for all particles and diameters you wish to consider. For this problem, Au, Cu, Al, SiO₂/Au Shell nanoparticles, and Graphite were considered with diameters ranging from $d = [10, 30, \dots, 130, 150] \text{ nm}$. When calculating the shell nanoparticles, the shell thickness was 5 nm. Calculate $\sigma_{abs, \lambda, p, j}$, using Eqn. (3.2.6), and find the SPR peaks for all of the absorption curves for all the particles and diameters.
- 2) Calculate the absorption of the fluid, $\sigma_{abs, \lambda, f}$, using Eqn. (3.2.5).

3) Integrate the blackbody radiation over the whole wavelength range

$$Area_{tot} = \int_{\lambda} I_{b,\lambda} d\lambda.$$

4) Consider all combinations of particles, $\left(\begin{matrix} database \\ N \end{matrix} \right)$. For each combination steps

a) and b) are considered.

a) Find the percentage, P_j , of the total concentration for each type of particle by

i) Sort the SPR peaks, found in step 1) which correspond to the specific combination and find the median between the peaks. Use the medians, along with the initial and final wavelength in which you are considering, to create an interval of wavelengths, i.e. $[\lambda_{min}, median, \lambda_{max}]$.

ii) Integrate $I_{b,\lambda}$ over the interval range found in step i), $A_j = \int_{\lambda_j}^{\lambda_{j+1}} I_{b,\lambda} d\lambda$.

Note: This is similar to the fraction of blackbody emissive power found in radiations books [103,112].

iii) Divide the area for the different intervals found in step ii) over that of the total found in step (3) to find percentages of the total concentration for

each particle type, $P_j = \frac{A_j}{Area_{tot}}$.

b) Calculate $area = \int_{\lambda} \left(\sum_j P_j \sigma_{abs,\lambda,p,j} + \sigma_{abs,\lambda,f} \right) I_{b,\lambda} d\lambda$ for each combination

5) Sort the combinations and choose the mixture with the greatest value for the area. Make sure all the diameter sizes and particle types are tracked.

6) Calculate the intensity, I_λ , and radiation, q_r , using Eqns. (3.2.2) and (3.2.7), respectively.

7) Record the value of q_r which corresponds to the bottom of the liquid container.

This value helps to determine whether the radiation reaches the bottom of the container or if the radiation is attenuated before it reaches the full liquid height.

These steps are repeated for every concentration, ϕ_{tot} . Once this is done, use the values found in step 7 and determine which is closest to 0. When having a value >0 implies that the radiation used is greater than necessary and backscattering can occur at the bottom of the surface of the container. Backscattering from the bottom of the surface is not considered. If the value is <0 , implies that the intensity did not penetrate all the way through the container. Repeat the steps for number of particles, N , and height, H . Figure 3.3.3 gives an outline of the process described here. See Appendix C for more details on method 2 and also on the code for this algorithm.

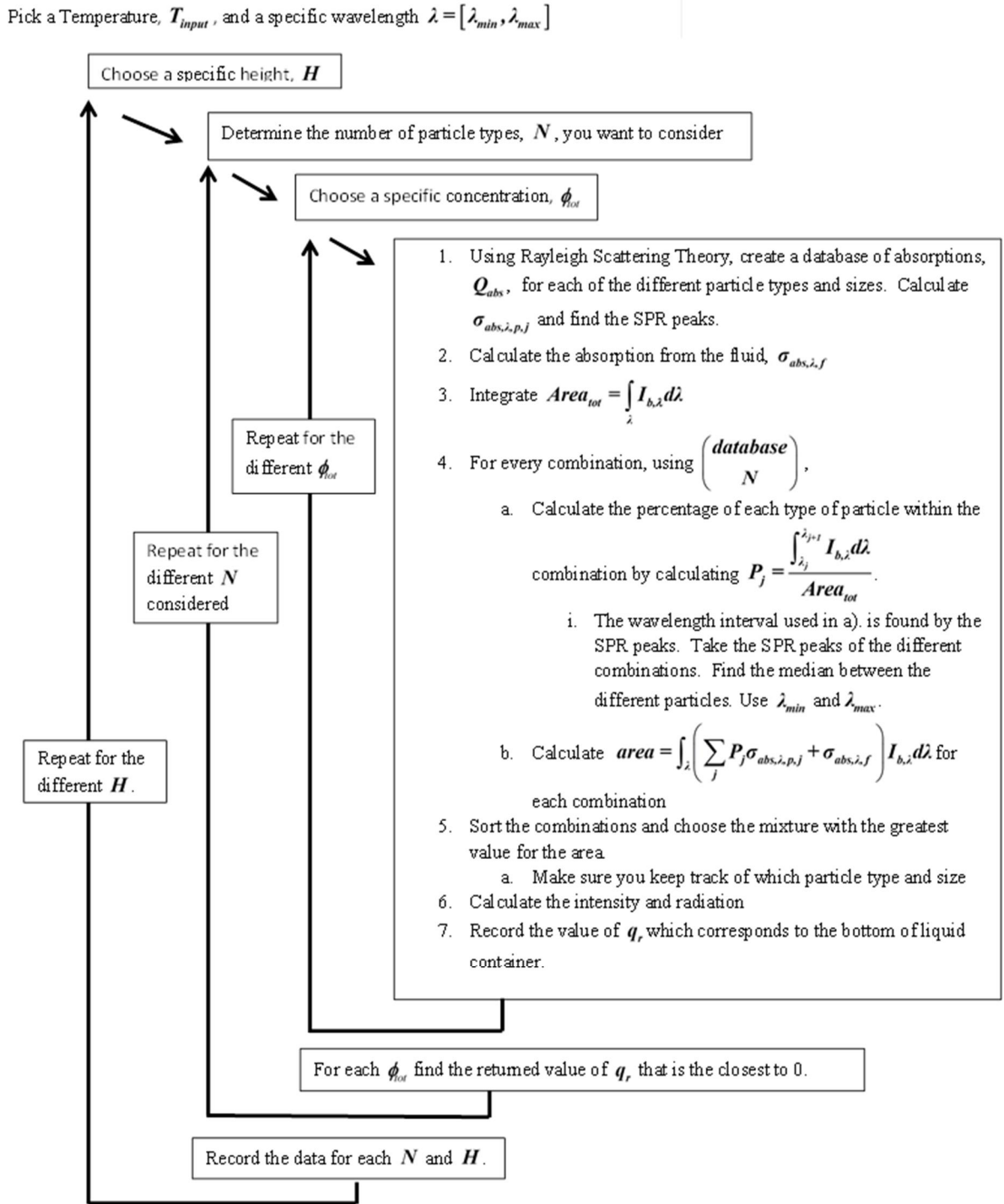


Figure 3.3.3: Algorithm for the hybrid nanofluid

3.4 Results based on the two methods

For these simulations, five different height values, $H = [1.2 \times 10^{-5}, 1.2 \times 10^{-4}, 1.2 \times 10^{-3}, 1.2 \times 10^{-2}, 1.2 \times 10^{-1}]$ m, six different concentrations values, $\phi_{tot} = [1 \times 10^{-6}, 1 \times 10^{-5}, 1 \times 10^{-4}, 1 \times 10^{-3}, 1 \times 10^{-2}, 1 \times 10^{-1}]$, four different N values, $N = [1, 2, 3, 4]$, and four different temperature values, $T_{input} = [1000, 3000, 5000, 5800]$ K, were used. The wavelength considered was between $\lambda = [200, 1000]$ nm and were chosen arbitrarily. A selection of data was collected in order to determine a correlation between H , ϕ_{tot} , N , and T_{input} . From step 7) in the algorithm, the optimized concentration for each H and N is given and presented in Fig. 3.4.1. To read this graph, choose T_{input} , H , and N to determine ϕ_{tot} . The correlation between H and ϕ_{tot} is such that as the height of the container increases the optimal concentration decreases. This is true for all values of N that were tested. This correlation is due to Eqn. (3.2.6). As the parameter H increases, the volume, V , increases resulting in ϕ_{tot} decreasing. This equation explains why this correlation does not depend on N and is a linear relationship because $\sum_j n_j V_{p,j} \ll V$.

Figure 3.4.1 also shows that for lower temperatures less concentration is needed for each height. If you refer to Fig. 3.1.3, as the temperature decreases, the

blackbody intensity, $I_{b,\lambda}$, curve decreases resulting in a decrease of intensity and therefore less absorption necessary. In summary, using the graphs in Sec. 3.3.1 is less accurate than running the simulations. Table 3.2 presents on the results that were obtained by performing the stimulations when varying the database, temperature, and N . To read the chart, the value in front of the particle types represents the percentage of the total concentration. These values add up to equal 100. Following the particle type gives the diameter of the specific particle of the particular concentrations used. Based on the information presented in this section, the following conclusions could be reached:

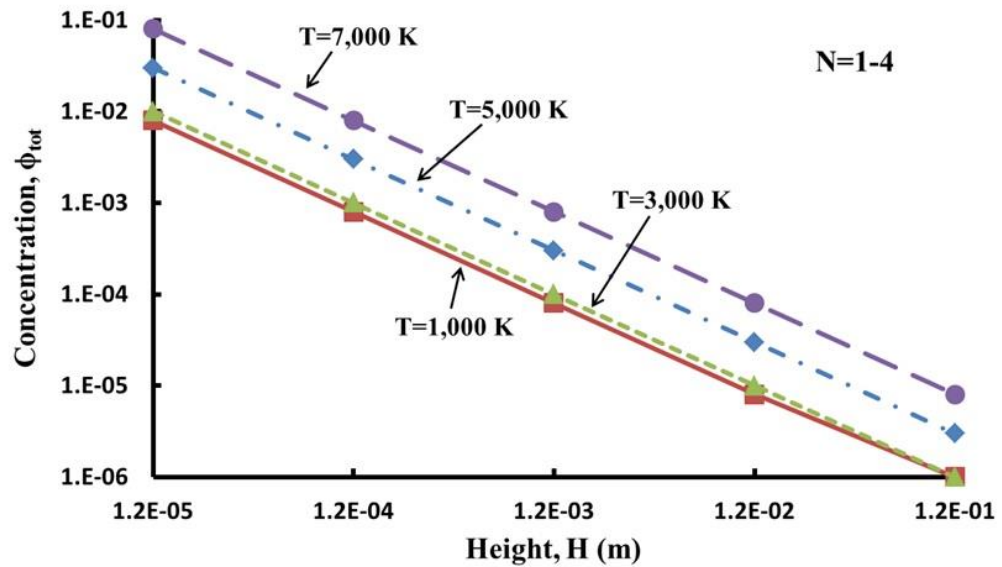


Figure 3.4.1: The correlation between concentration and height for different temperatures. This relationship holds for every value of N .

- The type of material within the database will affect the results. Table 3.2 gives insight to which particles mixtures to use when varying the database.
- Using $N = 1, 2$ is more ideal vs. when N is larger. As seen in Table 3.2, when $N = 3, 4$, often times the percentage of the material is close to 0%, implying N should be smaller.
- Extending or altering the wavelength range will vary the results and/or percentages to use. This is because the percentages were calculated using a specific wavelength.
- The input temperature can vary the mixtures to use. This is shown based on Fig. 3.1.3 by the different temperature curves and by Table 3.2.

- The parameters H and ϕ_{tot} do not change the mixture combination.

3.5 Conclusion

This chapter covers a hybrid nanofluid when exposed to radiation. Because of the tunable plasmonic properties of metallic nanoparticles and the many possible variables to consider, two optimization techniques were proposed to determining the correct recipe of nanoparticles submerged in water for a given temperature in order to get the optimal absorption. The first optimization uses two graphs dependent on diameter, SPR peak, and the area of the absorption. It also utilizes the fraction of emissive blackbody power chart found in radiation books. An algorithm was also given to determine the optimal combinations. A further study could be taking this recipe and using it on the most cost effective particles instead of the specific particles that were used in this paper. Different particle shapes and other fluids can be tested using this algorithm. Another possibility would be to include scattering from the particles and backscattering due to the bottom of the container. This paper will help to determine which particle mixtures would be suitable when exposed to radiation depending on the particular set of particles, size of particles, height of the container, concentration, and temperature.

Table 3.2: Combinations for various temperatures and databases

Temperature	Database	Combination
5,800 K	Au, Cu, Al, Graph, SiO ₂ /Au	100%Au(50nm)
		52%Au(50nm)+47%SiO ₂ /Au(30nm)
		40%Au(50nm)+20%SiO ₂ /Au(10nm)+40%SiO ₂ /Au(30nm)
		39%Au(50nm)+2%Au(70nm)+19%SiO ₂ /Au(10nm)+40%SiO ₂ /Au(30nm)
	Au, Cu, Al, Graph	100%Au(50nm)
		12.4%Au(10nm)+87.6%Au(50nm)
		12.4%Au(10nm)+26%Au(30nm)+61.6%Au(50nm)
		12.4%Au(10nm)+25.8%Au(30nm)+0.9%Au(50nm)+60.9%Au(70nm)
	Cu,Al,Graph	100%Cu(50nm)
		4.7%Cu50nm+95.3%Cu(70nm)
		0.3%Cu(30nm)+4.4%Cu(50nm)+95.3%Cu(70nm)
		0.1%Cu(10nm)+0.2%Cu(30nm)+4.4%Cu(50nm)+95.3%Cu(70nm)
	Al,Graph	100%Graph(130nm)
		3.1%Graph(90nm)+96.9%Graph(130nm)
		0.2%Graph(10nm)+2.9%Graph(90nm)+96.9%Graph(130nm)
		0.1%Al(70nm)+0.1%Graph(10nm)+2.9%Graph(90nm)+96.9%Graph(130nm)
5,000 K	Au, Cu, Al, Graph, SiO ₂ /Au	100%SiO ₂ /Au(30nm)
		33%Cu(50nm)+67%SiO ₂ /Au(30nm)
		15.5%Cu(50nm)+45%SiO ₂ /Au(10nm)+39.5%SiO ₂ /Au(30nm)
		0.4%Au(10nm)+15%Cu(50nm)+45.2%SiO ₂ /Au(10nm)+39.4%SiO ₂ /Au(30nm)
	Au, Cu, Al, Graph	100%Au(50nm)
		30%Au(50nm)+70%Au(70nm)
		7%Au(10nm)+22.5%Au(50nm)+70.5%Au(70nm)
		7%Au(10nm)+21.7%Au(30nm)+1%Au(50nm)+70.3%Au(70nm)
	Cu,Al,Graph	100%Cu(70nm)
		2.7%Cu(50nm)+97.3%Cu(70nm)
		0.1%Cu(30nm)+2.1%Cu(50nm)+97.8%Cu(70nm)
		0.04%Cu(10nm)+0.06%Cu(30nm)+2.1%Cu(50nm)+97.8%Cu(70nm)
	Al, Graph	100%Graph(150nm)
		6.6%Graph(130nm)+93.4%Graph(150nm)
		1.3%Graph(90nm)+5.3%Al(90nm)+93.4%Graph(150nm)
		0.06%Graph(10nm)+0.04%Graph(30nm)+1.9%Graph(90nm)+98%Graph(150nm)

*Shell thickness is 5 nm

**Wavelength range= (200,1000)nm

Table 2: Combinations for various temperatures (Continued)

Temperature	Database	Combination
3,000 K	Au, Cu, Al, Graph, SiO ₂ /Au	100%SiO ₂ /Au(50nm)
		10.3%Graph(10nm)+89.7%SiO ₂ /Au(50nm)
		0%Al(130nm)+10.3%Graph(10nm)+89.7%SiO ₂ /Au(50nm)
		0%Al(90nm)+0%Al(130nm)+10.3%Graph(10nm)+89.7%SiO ₂ /Au(50nm)
	Au, Cu, Al, Graph	100%Graph(150nm)
		0.03%Graph(90nm)+99.97%Graph(150nm)
		0%Graph(10nm)+0.03%Graph(90nm)+99.97%Graph(150nm)
		0%Graph(10nm)+0%Graph(30nm)+0.03%Graph(90nm)+99.97%Graph(150nm)
	Cu,Al,Graph	100%Graph(150nm)
		0.3%Graph(90nm)+99.97%Graph(150nm)
		0%Graph(10nm)+0.043%Graph(90nm)+99.97%Graph(150nm)
		0%Graph(10nm)+0%Graph(30nm)+0.03%Graph(90nm)+99.97%Graph(150nm)
	Al, Graph	100%Graph(150nm)
		0.3%Graph(90nm)+99.97%Graph(150nm)
		0%Graph(10nm)+0.043%Graph(90nm)+99.97%Graph(150nm)
		0%Graph(10nm)+0%Graph(30nm)+0.03%Graph(90nm)+99.97%Graph(150nm)
1,000 K	Au, Cu, Al, Graph, SiO ₂ /Au	100%SiO ₂ /Au(50nm)
		0.01%Al(130nm)+99.9%SiO ₂ /Au(50nm)
		0%Al(90nm)+0.01%Al(130nm)+99.9%SiO ₂ /Au(50nm)
		0%Al(70nm)+0%Al(90nm)+0.01%SiO ₂ /Au(130nm)+99.9%SiO ₂ /Au(50nm)
	Au, Cu, Al, Graph	100%Graph(150nm)
		0%Graph(70nm)+100%Graph(150nm)
		0%Graph(70nm)+0%Graph(90nm)+100%Graph(150nm)
		0%Graph(50nm)+0%Graph(70nm)+0%Graph(90nm)+100%Graph(150nm)
	Cu,Al,Graph	100%Graph(150nm)
		0%Graph(70nm)+100%Graph(150nm)
		0%Graph(70nm)+0%Graph(90nm)+100%Graph(150nm)
		0%Graph(50nm)+0%Graph(70nm)+0%Graph(90nm)+100%Graph(150nm)
	Al,Graph	100%Graph(150nm)
		0%Graph(70nm)+100%Graph(150nm)
		0%Graph(70nm)+0%Graph(90nm)+100%Graph(150nm)
		0%Graph(50nm)+0%Graph(70nm)+0%Graph(90nm)+100%Graph(150nm)

*Shell thickness is 5 nm

**Wavelength range= (200,1000)nm

3.6 List of Variables

A

Integrated Area (W/m)

$Area_tot$	Integrated Area (W/m)
$area$	Integrated Area (W/m)
C_{abs}	Cross section (m ²)
d	Diameter (m)
$database$	Database of particles
H	Height (m)
h	Planck's constant (J s)
I	Intensity (W/m ²)
k	Wavenumber (m ⁻¹)
k_B	Boltzmann constant (m ² kg/s ² K)
L	Length (m)
N	Number in combination
n	Number of particles in fluid
P	Polarizability constant
P_j	Percentage of concentration
Q_{abs}	Absorption coefficient (-)

q_r	Radiation term (W/m ²)
S	Graphite constant
T	Temperature (K)
V	Volume (m ³)
y	Direction (m)

Greek Symbols

α	Polarizability
$\hat{\gamma}$	Damping term (s ⁻¹)
ε	Permittivity
ε_∞	Permittivity of the bulk particle
κ	Absorption index
λ	Wavelength (m)
σ	Absorption coefficients (m ⁻¹)
ϕ	Volume Fraction
ω	Frequency (s ⁻¹)

Subscript

<i>abs</i>	Absorption
<i>b</i>	Blackbody
<i>f</i>	Fluid
<i>input</i>	Input Temperature
<i>j</i>	Type of nanoparticles
<i>max</i>	Maximum
<i>min</i>	Minimum
<i>p</i>	Particle
<i>plamsa</i>	Plasma
<i>S</i>	Graphite constant
<i>tot</i>	Total
λ	Wavelength

Chapter 4

Concluding Remarks

This thesis describes two different computational analyses for the field of solar energy. The first analysis illustrates the characteristics of a single nanoparticle submerged in a solid phase change material. When the particle reaches a temperature higher than the melting temperature of the medium, a film surrounding the particle is developed. The temperature profiles of the particle, film, and solid medium are given. It was found that the temperature profile of the particle correlates to the amount of absorption for the particle. The film size surrounding the particle differs depending on the type of particle used, the size of the particle, and the medium. Also, when viewing the temperature profile of the medias, there are two noticeable temperature jumps which correspond to an interface resistance at the particle/film interface and one due to the film. When the film is larger, this temperature jump is more pronounced. A ratio and its conditions

are derived to help determine if the particle/film interface resistance is necessary to include. This analysis gives insight to the size of the films formed around the individual particles and the temperature profiles around them.

The second analysis views a hybrid nanofluid when exposed to radiation in hopes of enhancing the efficiency. Because of the tunable plasmonic properties of metallic nanoparticles and the many possible variables to consider, this work proposed two different techniques in order to optimize the hybrid nanofluid. The incoming temperature, particle composition, and size can vary the amount of absorption of the nanofluid and therefore change the hybrid nanofluid. This analysis was used for a range of wavelengths. Chapter 3 gave insight to a possible new mixture that would be suitable when exposed to radiation depending on the particular set of particles, size of particles, height of the container, concentration, and temperature.

Both chapters contribute to the field of solar energy by providing insight to enhancing the efficiency of nanoparticle mixture. No other work had been conducted for a single nanoparticle analysis, but rather efforts have been focused on multiple nanoparticles in the PCM as a whole. Therefore this work can be used to understand the fundamental physics of one particle submerged in a fluid. Similar to the first study, no work has been completed to understand how to achieve an optimal amount of radiation absorption by varying the hybrid nanofluid. Both of these studies can be useful when attempting to achieve maximum absorption.

Appendix A

A.1 Boiling and melting temperature shift for a nanofluid

Boiling is a phenomenon that occurs at a heated surface. When applying heat to an ideal solution (one where a solute is mixed into a solvent), the kinetic energy of the molecules increase, causing the molecules at the surface to want to break away from their structure in the phase and transition to another phase. However, when there is a particle close to the surface, the kinetic energy will act like an obstruction, and the molecules at the surface will not have as much kinetic energy causing the vapor pressure to decrease. When dealing with the phases of liquid and gas, the boiling temperature does not occur until the vapor pressure is equal to the ambient pressure. If there is an obstruction like a nanoparticle, then the boiling temperature at a particular pressure will increase, called the boiling point elevation. See Fig. A.1.1.

Similarly, the freezing temperature decreases with a decrease of pressure, called the freezing point depression. This idea is described using Henry's law and Raoult's law for a solute and solvent [113]. Henry's law explains the solubility of gasses in water and is described as the pressure of the solute is equal to a constant times the molality, $P_{solute} = K \cdot molality$. Raoult's law describes the relationship for the solvent or the fluid. This law states that the pressure of the solvent is equal to the vapor pressure of the solvent multiplied by the mole fraction of the fluid,

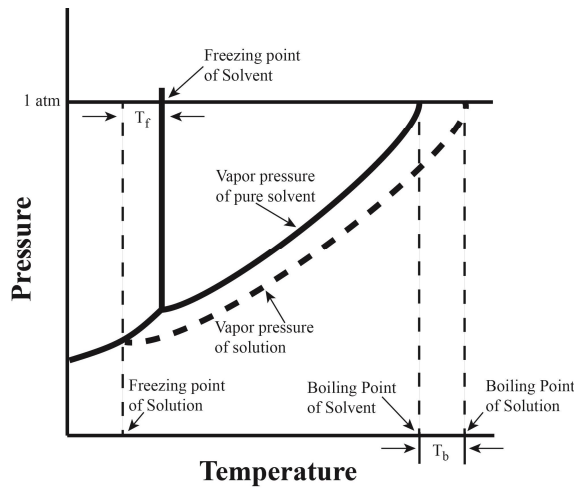


Figure A.1.1: The melting point depression and boiling point elevation phase change diagram.

$P_{\text{solvent}} = X P_{\text{vapor-pressure}}$. Utilizing these two laws, formulations for the shift in temperature for both boiling and melting for a solute in a solvent are given by

$$\begin{aligned}\Delta T_b &= K'_b X_2 = K_b \cdot \text{molality} \\ \Delta T_f &= K'_f X_2 = K_f \cdot \text{molality}\end{aligned}\tag{A.1.1}$$

where X_2 is the mole fraction of the solutes and K_b and K_f are the molal boiling and melting constants found in a chart in [113] which only depends on the solvent. For water $K_b = 0.51$ and $K_f = 1.86$ [113] (page 130-134). The relation between K_b and K'_b is

$$1000K_b = K'_b MW_f\tag{A.1.2}$$

where MW_f is the molecular weight for the solvent. For water, $MW_f = 18.01528 \times 10^{-3} \text{ kg/mol}$. The molality is defined by the number of moles of solute over the mass of the solvent ($\text{molality} = \frac{\text{amount of solute (mol)}}{\text{mass of solution (kg)}}$). Another derivation for this comes from Gibb's free energy. The resulting equation is

$$\begin{aligned}\Delta T_b &= \left(\frac{RT_0^2 MW_f}{1000 \Delta H_{\text{vap}}} \right) \cdot \text{molality} \\ \Delta T_f &= \left(\frac{RT_0^2 MW_f}{1000 \Delta H_{\text{melt}}} \right) \cdot \text{molality}\end{aligned}\tag{A.1.3}$$

where $R = 8.3144621 \text{ J/K} \cdot \text{mol}$ is the gas constant and T_0 is the boiling or melting point for the solvent. This implies that the molal boiling and melting point constants are calculated by $K_{b/f} = \frac{MW_f RT_0^2}{1000 \Delta H_{\text{vap/melt}}}$. Equation (A.1.3) only works for the very dilute solutions (10^{-4} m [113]). In 2009, Ge and Wang [114] derived a more complex equation for the freezing point depression and boiling point elevation for higher concentration. Electrolyte solutions were used for this study. This expression involves more information about the solute.

The equations given were for that of a solvent with very small particles <3nm. This appendix looks at nanofluids with particles greater than just 3nm to see if the same relations apply. In 2008, Xie et al. [115] experimentally compared nanoparticles of approximately 3.8 nm in size follow Eqn. (A.1.3) for melting temperatures. Within this section, the freezing point depression was tested for

$\text{Al}_2\text{O}_3\text{-H}_2\text{O}$ solution and $\text{TiO}_2\text{-H}_2\text{O}$ solution with various weight fractions. This section showed that as the weight fractions increases, the temperature depression increases and gets as high as 8°C for a weight fraction of 6.19% of $\text{Al}_2\text{O}_3\text{-H}_2\text{O}$ solution. This paper also suggests that nanoparticles of bigger size might have similar behaviors to solutions of lowering the melting temperature compared to the pure solvent. These results could not be duplicated using Eqn. (A.1.2), see Table A.1. When calculating the freezing point depression, a value of 1°C was recovered. This does show a shift, but is not very pronounced like [115] suggests.

In 2007, Kim [116] presented a master's thesis which studied the boiling point depression for alumina, sirconia, silica, and diamond dispersed in water for various concentrations. The average particle size is 20 nm. Kim reported that for dilute solutions ($<1\text{ v\%}$), there was no significant change relative to the boiling point of water. The largest boiling point elevation differential was $\Delta T = 0.5$. Using Eqn. (A.1.3), confirmed this data. There was no significant increase with these concentrations. Recently, Harikrishnan and Kalaiselvam [117] studied the thermal and heat characteristics of palmitic acid with TiO_2 for different mass fractions. This paper shows there is a decrease in melting temperature; however, it is not a significant change and only changes by 1°C . Using Eqn. (A.1.3) to calculate the molal melting point constant and freezing point depression confirms this data. Similar experimental data can be found in [118] which compared the freezing point depression for $\text{Al}_2\text{O}_3\text{-H}_2\text{O}$ solution for different mass concentrations. The depression was no more than 0.2°C . This was confirmed using Eqn. (A.1.3). Raam

et al. [119] provided a review on solar thermal energy storage. Within that paper, the author provided several sets of data for the melting temperature shift with various types of nanofluids and their concentrations. The shift that was melting point depression described in the paper can be described using Eqn. (A.1.3).

A summary of these papers can be viewed from Table A.1.1. This table provides the melting point depression, dT_m , or boiling point elevation, dT_B , given by the papers and also what was calculated using Eqn. (A.1.3). You can see that only the data from [115] do not match. The conclusion is that melting point depression and boiling point elevation can be modeled using Eqn. (A.1.3); however, it is of an insignificant change in temperature.

Table A.1.1: Comparison of experimental data and Eqn. (A.1.3) for the melting point depression and the boiling point elevation

Type of Nanofluid	Concentration	Paper Results	Eq. (A.1.3) Results
Xie et al. [115]			
TiO ₂ -H ₂ O	7.85 wt%	dT _m = -4°C	dT _m = -0.28°C
Al ₂ O ₂ -H ₂ O	6.19 wt%	dT _m = -8.5°C	dT _m = -0.015°C
Kim [116]			
Al ₂ O ₂ -H ₂ O	1.0 v%	dT _B = 0.1°C	dT _B = 0.9°C
	0.1 v%	dT _B = 0.2°C	dT _B = 0.71°C
	0.01 v%	dT _B = 0.2°C	dT _B = 0.23°C
Harikrishnan and Kalaiselyam [117]			
TiO ₂ -Palmitic acid	0.1 wt%	dT _m = -2°C	dT _m = -0.09°C
	0.2 wt%	dT _m = -2°C	dT _m = -0.71°C
	0.3 wt%	dT _m = -2°C	dT _m = -0.26°C
Mare et al. [118]			
Al ₂ O ₂ -H ₂ O	1 v%	dT _m = -0.1°C	dT _m = -0.17°C
	2 v%	dT _m = -0.1°C	dT _m = -0.36°C
	3 v%	dT _m = -0.1°C	dT _m = -0.53°C
Jinze et al. [120]			
Al ₂ O ₂ -H ₂ O	0.1 wt%	dT _m = -0.52°C	dT _m = -0.01°C
	0.2 wt%	dT _m = -0.60°C	dT _m = -0.01°C
	0.5 wt%	dT _m = -0.60°C	dT _m = -0.03°C
Al ₂ O ₂ -Paraffin [121]	5 wt%	dT _m = 0.5°C	dT _m = 0.0°C
	10 wt%	dT _m = -0.20°C	dT _m = -0.1°C
Graphite Platelets-Paraffin [122]	1 wt%	dT _m = -0.10°C	dT _m = -0.0°C
	3 wt%	dT _m = -0.10°C	dT _m = -0.01°C
	5 wt%	dT _m = -0.30°C	dT _m = -0.01°C

Appendix B

B.1 Mathematical steps for Chapter 2-Thermal Storage

When considering the analysis of the single nanoparticle in a thermal storage material, two main steps were used. Step one describes the particle heating through radiation with the intensity of the particle less than the melting temperature of the medium, $T_p < T_m$. Step two was such that the temperature of the particle is between the melting temperature of the medium and 89% of the critical temperature, $T_m \leq T_p < 0.89T_{crit}$. Within this step, a liquid film begins to develop and grow around the particle. Eighty nine percent of the critical temperature was used because it was predicted by Kotaidis et al. [68] that a vapor layer may begin to form and cause complexity to the problem. This appendix gives a more rigorous description of the 2-D analysis of each step.

B.1.1 Step 1: Particle within a solid medium

Within this step, the particle is heated through radiation. Lumped heating through radiation is used for the particle. This particle is in a solid medium. A pictorial image of the process is given in Fig. B.1.1.

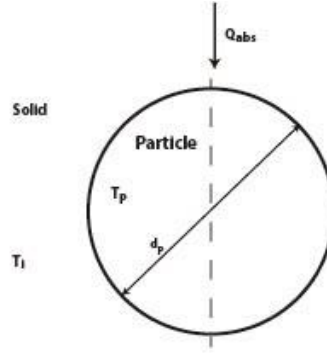


Figure B.1.1: Particle within a solid medium.

The temperature profile for the particle is described using

$$\rho_p V_p c_p \frac{\partial T_p}{\partial t} = Q_{abs} \quad (\text{B.1.1})$$

where T_p is the temperature of the particle and Q_{abs} is the absorption term described by

$$Q_{abs} = k \text{Im}(\alpha) I_{inc} = C_{abs} I_{inc} \quad (\text{B.1.2})$$

The absorption term is given using Rayleigh's scattering for small particles compared to that of the wavelength. Note that the wavelength range is $\lambda = [150, 2000] \text{ nm}$. The term C_{abs} includes the absorption due to the plasmonic effects. The plasmonic effects occur when a specific wavelength interacts with the electrons at the surface of the particle. Drude's model was used to describe the oscillating electrons from the plasmonic properties. This model is derived by assuming the electrons act as harmonic oscillators. Most of these particles are effected within the visible range which is $\sim [400, 700] \text{ nm}$. The wavelength was

expanded further to include the whole solar spectrum. More information on the derivation of C_{abs} and Drude's model are described in Appendix D.3, D.4, and D.7.

The temperature profile to the solid medium in radial and polar coordinates is given as

$$\frac{\partial T_j}{\partial t} = \frac{\hat{k}_j}{\rho_j c_j} \left(\frac{\partial^2 T_j}{\partial r^2} + \frac{2}{r} \frac{\partial T_j}{\partial r} \right) + \frac{\hat{k}_j}{\rho_j c_j} \left(\frac{1}{r^2} \frac{\partial^2 T_j}{\partial \theta^2} + \frac{1}{r^2} \frac{\cos \theta}{\sin \theta} \frac{\partial T_j}{\partial \theta} \right) \quad (\text{B.1.3})$$

After a simple non-dimensional analysis, the temperature was found to depend little on the theta direction. Therefore, Eqn. (B.1.3) reduces to

$$\frac{\partial T_j}{\partial t} = \frac{\hat{k}_j}{\rho_j c_j} \left(\frac{\partial^2 T_j}{\partial r^2} + \frac{2}{r} \frac{\partial T_j}{\partial r} \right) \quad (\text{B.1.4})$$

The boundary conditions for this equation are such that the temperature of the medium and particle are the same initial temperature at $t=0$ for all r and the temperature flux at the particle/medium interface is equal to 0.

$$\begin{aligned} T_p &= T_j = T_i \quad \text{at} \quad t=0 \quad \text{and} \quad \forall r \\ \frac{dT_j}{dr} &= 0 \quad \text{for} \quad r = d_p \end{aligned} \quad (\text{B.1.5})$$

B.1.2 Step 2: Film surrounding the particle within a solid medium

Once the temperature of the particle reaches the melting temperature of the material, a film begins to form between the solid and particle interface. See Fig. B.1.2. Now the mathematical formulation becomes a little more complex because of

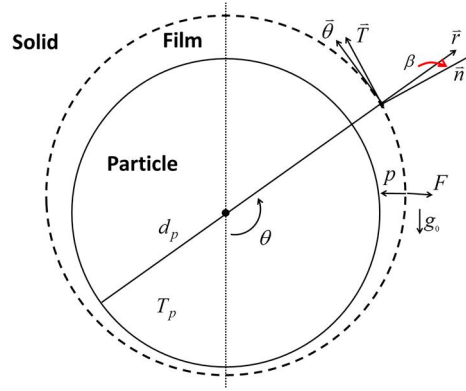


Figure B.1.2: Particle within a liquid film and solid medium.

the introduction of the film growth velocity. Two interface velocities are used in the radial direction, which describes the growth of the liquid film with pressure, p , the Van der Waal forces, F , and gravity, g_0 , acting in the r direction, and the polar direction which describes the effect due to gravity. Before the velocities are described, the area specific mass flux, dm''/dt [kg/m²s], is given by the expression

$$\frac{dm''}{dt} = \rho_l v_r \cos(\beta) + \rho_l v_\theta \sin(\beta) \quad (\text{B.1.6})$$

Here β is the angle between the radial and normal direction. Refer to Fig. B.1.2 and Appendix D.6 for more information on how to find β . This mass flow rate is defined by the mass of a substance which passes per unit time or similarly, as the product of the density, area, and velocity. The variable dm''/dt , is area specific therefore

$$\frac{dm''}{dt} = \rho_l \cdot \mathbf{v} \cdot \mathbf{n} \quad \text{where } \mathbf{v} \text{ is the vector velocity in the } r \text{ and } \theta \text{ direction and } \mathbf{n} \text{ is the}$$

vector normal of a sphere. The vector normal for a sphere in spherical coordinate is defined by

$$n = \frac{\langle r \cos(\beta), r \sin(\beta) \rangle}{\sqrt{r^2 (\cos^2(\beta) + \sin^2(\beta))}} = \frac{\langle r \cos(\beta), r \sin(\beta) \rangle}{r} = \langle \cos(\beta), \sin(\beta) \rangle. \quad (\text{B.1.7})$$

This implies that

$$dm''/dt = \rho_l \cdot v \cdot n = \rho_l \begin{bmatrix} v_r \\ v_\theta \end{bmatrix} \cdot \begin{bmatrix} \cos(\beta) \\ \sin(\beta) \end{bmatrix} = \rho_l (v_r \cos(\beta) + v_\theta \sin(\beta)).$$

The radial velocity for the interface of the film and solid medium is given by

$$\rho_l \left(\frac{\partial v_r}{\partial t} + v_r \frac{\partial v_r}{\partial r} - \frac{v_r v_\theta}{r} \right) = \frac{3F}{4\pi d_{sl}^3} - \frac{\partial p}{\partial r} + (\rho_s - \rho_l) g_0 \cos \theta \quad (\text{B.1.8})$$

Refer to Fig. B.1.2 to view the force diagram acting at the interface of the film and solid medium. The first term on the right hand side describes the Van der Waal forces, F .

$$F = \pi d_p \Delta\gamma_0 \left(\frac{a_0}{a_0 + 0.5(d_{sl} - d_p)} \right)^2 \quad (\text{B.1.9})$$

The parameter $\Delta\gamma_0 = \gamma_{SP} - \gamma_{LP} - \gamma_{SL}$ where γ [kg/s^2] is the interfacial energies between the solid/liquid, liquid/particle, and the solid/liquid interfaces. The parameter a_0 [m] is the molecular diameter of the two materials and $0.5(d_{sl} - d_p)$ represents the thickness of the liquid layer. For water $\alpha_0 = 0.10 \times 10^{-6} m$ and $\Delta\gamma_0 = 31.7 \times 10^{-3} \text{ kg}/\text{s}^2$ [65] and for n-octadecane, $\alpha_0 = 0.12 \times 10^{-10} m$ and $\Delta\gamma_0 = 9.6 \times 10^{-3} \text{ kg}/\text{s}^2$ [66]. The Van der Waal forces describe the force given by the

molecular attraction between the molecules within each substance. This force was derived by using Gibb's free energy and more detail on the derivation of this is found using Appendix D.1.

The second term given in Eqn. (D.1.8) characterizes the pressure and is described using the Clausius-Clapeyron Equation. This equation is also derived by using Gibb's free energy and describes a relationship between the pressure and temperature of two phases of a pure substance. The Clausius-Clapeyron equation states that the pressure term can be rewritten using the temperature, T , density, ρ_l , and latent heat, h_{sl} :

$$\frac{dp}{dr} = \frac{h_{sl}\rho_l}{T} \frac{dT}{dr} \quad (\text{B.1.10})$$

The derivation for this term is given in Appendix D.2. The last term describes the effects due to buoyancy/gravity that corresponds to the r direction where $g_0 = -9.8 \text{ m/s}^2$ is the gravitational force. The polar interface velocity, v_θ , can be expressed by

$$\rho_l \left(\frac{\partial v_\theta}{\partial t} + v_\theta \frac{\partial v_\theta}{\partial \theta} - \frac{v_r v_\theta}{r} \right) = (\rho_s - \rho_l) g_0 \sin \theta \quad (\text{B.1.11})$$

Again, the term on the right hand side represents the buoyancy/gravitational effects.

There are no viscous terms included in these equations. They are said to be negligible at the interface. The non-dimensional version of Eqn. (B.1.8) is

$$\left(\frac{\partial \hat{V}_r}{\partial \tau} + \hat{V}_r \frac{\partial \hat{V}_r}{\partial R} - \frac{\hat{V}_\theta^2}{R} \right) = \frac{3d_p \Delta \gamma_0}{32\rho_l \hat{\alpha}^2 \phi^3} \left(\frac{a_0}{a_0 + 0.5d_p(\phi-1)} \right)^2 - \frac{d_p^2}{4\hat{\alpha}^2} \frac{h_{sl} \partial \Theta}{\Theta \partial R} + \frac{(\rho_s - \rho_l)}{\rho_l} \frac{d_p^3}{8\hat{\alpha}^2} g_0 \cos(\theta) \quad (\text{B.1.12})$$

This equation was used to see how the Van der Wall force, pressure force, and force due to gravity effect the velocity equation in the radial direction. Using the three terms on the right hand side and the results from the simulations, it was concluded that

$$\begin{aligned} \frac{3d_p \Delta \gamma_0}{32\rho_l \hat{\alpha}^2 \phi^3} \left(\frac{a_0}{a_0 + 0.5d_p(\phi-1)} \right)^2 &\approx 10^4 \\ \frac{d_p^2}{4\hat{\alpha}^2} \frac{h_{sl} \partial \Theta}{\Theta \partial R} &\approx 1 \\ \frac{(\rho_s - \rho_l)}{\rho_l} \frac{d_p^3}{8\hat{\alpha}^2} g_0 \cos(\theta) &\approx 10^{-7} \end{aligned} \quad (\text{B.1.13})$$

This implies that the gravitational effects are negligible compared to the pressure effect due to the Clausius-Clapeyron.

The temperature of the particle and film is described using the same temperature expression used in the first step Eqns. (B.1.1-B.1.4). The film temperature profile is similarly given to that of the solid medium temperature profile. The boundary condition at the interface of the liquid film and solid medium interface is dependent on the latent heat and velocities given by

$$STE = \frac{c_p}{h_{sl}} \frac{\partial T}{\partial R} \Big|_{r=d_b} = \frac{c_p}{\hat{k}_l} \frac{\partial m''}{\partial t} \frac{d_p}{2} \quad (\text{B.1.14})$$

where STE is the Stefan number. The Stefan number is a dimensionless parameter that calculates the rate of phase change. At $t = t_1$, $T_m = T_m \quad \forall r > d_p$. This means that at the second stage when the film begins to develop, the temperature of the medium is the same as it was right before the phase change begins to occur. This is true as well for the liquid film. The boundary condition between the particle and the liquid film incorporates an interface resistance, \tilde{r} , which is provided by

$$\begin{aligned} Q_{abs} &= C_{abs} I = \frac{\Delta T A}{\tilde{r}} \\ T &= T_p - \frac{Q_{abs} \tilde{r}}{A} \end{aligned} \tag{B.1.15}$$

This resistance is particle material specific. For Au, Ag, Cu, and Al, the interface resistance is $\tilde{r} = 15 \times 10^{-9}, 5 \times 10^{-9}, 5 \times 10^{-9}, 2.5 \times 10^{-9}$ respectively. These values were found using Vera et al [64]. This implies that Au has the largest interface resistance when comparing these particles.

B.2 Code describing the particle in a solid medium with a film formation

This is the MATLAB code describes the film formation and the temperature profiles for a spherical nanoparticle of different materials. In main program is called *particle_film_soild_2D.m*. This function calls *mie_scattering.m*, *medium_properties.m*, and *particle_properties.m*. This function, *mie_scattering.m*, is found in Appendix D.7. Fourth order Runge Kutta was used to calculate the time components and finite

different solved the space components. In this function, data was saved to file. This information consisted of the temperature profile of the particle (Θ_p), both velocities V_r and V_θ (in the program V_r is represented by W and V_θ is represented by U), the film parameter (ϕ), and the temperature profile for the film and medium after every 1000 iterations.

```
function particle_film_solid_2D()

% This program calls RK functions, particle_properties.m,
% medium_properties.m, mie_scattering.m
% All the properties are global variables
% this is the particle in medium with film formation. Symmetric. Calls for particle in solid
% medium before melting.
%2D

% perform the 4th order RK for finding phi and Theta_p also the time for
% temp_films and performs the FD for W, and Theta_l in R direction
% THIS PROGRAM USES THE PROPERTIES TO various paraffins.

% num_l == 1 ---> water
% num_l == 3 ---> n-octadecane
% num_l == 4 ---> n-eicosane

% It also has properties for 5 different kinds of metals

% num_p == 1 ---> gold
% num_p == 2 ---> silver
% num_p == 3 ---> copper
% num_p == 4 ---> aluminum
```

[illegible]


```
%%%%%%%%%%%%%%%%%%%%%%%%%%%%%%%%%%%%%%%%%%%%%%%%%%%%%%%%%%%%%%%%%%%%%%%%%
```

```
T_initial = 250+20; %[K] room temperature
```

```
T_initial_p = 250+20; % [K] room temperature
```

```
intensity = 1e8; % [W/m^2 ==> kg/s^3] LHP*rho_l*c_l*v_0*T_inf %% finds intensity
```

```
alpha = lambda_s/(rho_s*c_s); % thermal diffusivity in water fluid
```

```
alpha_l = lambda_l/(rho_l*c_l); % thermal diffusivity in vapor fluid
```

```
% p_infty = 101325*1e-9; %[Pa==>kg/s^2 nm] pressure of the liquid far away from the  
surface [1atm]
```

```
g_0 = -9.8*1e9; % [m/s^2 ==> nm/s^2] gravity
```

```
sprintf('T_melt/T_inf = %e\n',T_melt_m/T_inf)
```

```
sprintf('0.89*T_crit/T_inf = %e\n',0.89*T_crit/T_inf)
```

```
sprintf('T_melt_p/T_inf = %e\n',T_melt_p/T_inf)
```

```
%%%%%%%%%%%%%%%%%%%%%%%%%%%%%%%%%%%%%%%%%%%%%%%%%%%%%%%%%%%%%%%%%%%%%%%%%
```

```
% % % % calculate the absorption and scattering cross section for both the vapor and liquid
```

```
% % % % % THIS WILL CHANGE DEPENDING ON THE FILM size
```

```
%%%%%%%%%%%%%%%%%%%%%%%%%%%%%%%%%%%%%%%%%%%%%%%%%%%%%%%%%%%%%%%%%%%%%%%%%
```

```
% % % % % before the film developed
```

```
% % % % % the absorption and scattering over the whole spectrum
```

```
lambda = linspace(150,2000,150); %[m==>nm]
```

```
length_lambda = length(lambda);
```

```
for i = 1:length_lambda
```

```
    [C_abs(i)] = mie_scattering(epsilon_m,num_p,dp0*1e-9,dp1*1e-9,lambda(i)*1e-9);
```

```
end
```

```

C_abs_l = sum(C_abs*1e18); % [m^2 ==> nm^2]

%%%%%%%%%%%%%%%%%%%%%%%%%%%%%%%%%%%%%%%%%%%%%%%%%%%%%%%%%%%%%%%%%%%%%%%% step functions for all the films

dR = 2.857142857142847e-002;

R = [1:dR:8*dR+1]; % R step for most of the grid in the SOLID. note that it changes for the
initial R so that we can know where we are tabulating it.

dtau1 = dR/(2*dp0); %1.782595603733815e-006; % tau

theta = [-pi/2:0.5*pi/2]; %0.1

theta = linspace(-pi/2,pi/2,9);

dtheta = theta(2)-theta(1);

maxit = 10000000;

% ----- for film

dyy_f1 = 2.857142857142847e-003;

dtauf1 = dyy_f1/(2*dp0);

R_ITER=length(R);

Angle_iter = length(theta);

%%%%%%%%%%%%%%%%%%%%%%%%%%%%%%%%%%%%%%%%%%%%%%%%%%%%%%%%%%%%%%%%%%%%%%%% Initialize the values

% the interface velocities are 0 initially, then I use the steady state

% computation to the first iteration whenever the film starts to form

Theta_p_new = (T_initial_p/T_inf); % absolute temp of particle assumed to be boiling temp
of the temp fluid of Water = T_p/T_inf Room temperature --> matrix dependent on angle
and time

Theta_s_new = [(T_initial/T_inf)*ones(length(R)+1,1)]; %first the temp is without radiation
3-D Matrix dependent on [y direction, angle, time]

W_new_sl = zeros(1,length(theta));

```



```

string_dp = num2str(dp0);

name1 = strcat('Phi_solid_',string_dp,string1,string2,'.txt');

fid = fopen(name1,'w');

name2 = strcat('Theta_p_solid_',string_dp,string1,string2,'.txt');

fid2 = fopen(name2,'w');

fprintf(fid,'T_amb = %d\n',T_inf);

fprintf(fid,'dp0 = %e\n',dp0);

fprintf(fid,'dtau1 = %e\n',dtau1);

fprintf(fid,'dtau_f1 = %e\n',dtauf1);

fprintf(fid,'dtime = %e\n',dtau1*dp0^2/(4*alpha));

fprintf(fid,'dtime_f1 = %e\n',dtauf1*dp0^2/(4*alpha_l));

fprintf(fid,'alpha_l = %e\n',alpha_l);

fprintf(fid,'alpha = %e\n',alpha);

fprintf(fid,'dR = %e\n',dR);

fprintf(fid,'dyy_f1 = %e\n',dyy_f1);

fprintf(fid,'dr = %e\n',dR*dp0/2);

fprintf(fid,'dr_f1 = %e\n',dyy_f1*dp0/2);

%-----

% saving the velocity

namewlv = strcat('W_sl',string_dp,string1,string2,'.txt');

fid88 = fopen(namewlv,'w');

fprintf(fid88,'%f\n',W_new_sl(1,1));

nameulv = strcat('U_sl',string_dp,string1,string2,'.txt');

fid99 = fopen(nameulv,'w');

```

```

fprintf(fid99,'%f\n',U_new_sl(1,1));

%%%%%%%%%%%%%%%%%%%%%%%%%%%%%%%%%%%%%%%%%%%%%%%%%%%%%%%%%%%%%%%%%%%%%%%%

format short E

% counter = 1; % temp variable to tell me iteration for count before film formed

temp_iter11 = 0;

stupid_temp=0;

count_film1 = 1;% temp variable to tell me iteration for count after the film begins to form.

dR_change = dR;

%%%%%%%%%%%%%%%%%%%%%%%%%%%%%%%%%%%%%%%%%%%%%%%%%%%%%%%%%%%%%%%% START OF FUNCTION

for k = 1:maxit% this is the time step

if Theta_p_new(end)<= T_melt_m/T_inf %NO BUBBLE FORMATION UNTIL T_MELTING OF
MEDIUM

Theta_p_new(k+1) = runkut3(F_Thetap_s,C_abs_l,Theta_p_new(end),alpha,dtau1); % temp
should be the same throughout the whole

fprintf(fid2,'%0.8f\n',Theta_p_new(end)); % print to file

Theta_s_new(1,k+1) = Theta_p_new(end); %this is the temperature of the particle

%this is for the liquid temp

for j = 2:R_ITER % this is for the space step in R

%first find the Neumann boundary condition

if j == 2

% solves using Finite difference this is the temp at the boundary of Phi=1

Theta_s_new(2,k+1)=Theta_s_new(1,k+1);

else

```

```

theta_s_temp=    runkut5(F_Thetam_s,Theta_s_new(j+1,k),Theta_s_new(j,k),Theta_s_new(j-
1,k),1+(j-2)*dR,alpha,dtau1); % fourth order RK for time step

% this is because the temperature should not be below the T_initial

if theta_s_temp >= T_initial/T_inf

Theta_s_new(j,k+1) = theta_s_temp;

else

Theta_s_new(j,k+1) = T_initial/T_inf;

end % end the if statement temp_s_temp

end % end if j==temp+2

end % end for loop j (for space)

%print to file

if mod(k+1,50) == 0 % prints every 100 counts

fprintf('k = %d\n',k+1)

string_count1 = num2str(k+1);

name4 = strcat('Theta_s_liquid_',string_dp,string1,string2,string_count1,'.txt');

fid4 = fopen(name4,'w');

for iv = 1:size(Theta_s_new,1)

fprintf(fid4,'%0.8f\n',Theta_s_new(iv,k+1));

end

end % end mod

elseif Theta_p_new(end)<= 0.89*T_crit/T_inf

% BEGIN FILM 1 FOMRATION

% this is for when the temp of particle exceeds the critical temperature and develops a vapor

film. Now we will have a film velocity interface w

```

```

% NOTICE: the C_abs and C_sca should vary based on the film layer.

%%-----

% creates a boundary condition for T and also opens a file to print

if count_film1 == 1

sprintf('Film 1 formation started')

count = k;

fprintf(fid,'%d\n',k); %print in phi

fprintf(fid2,'%d\n',k); % print in theta_p

Theta_film1(:,count_film1) = Theta_p_new(end)*ones(1000,length(theta));

for ii = 1:Angle_iter

Theta_s_1(1:size(Theta_s_new,1)-1,ii,count_film1) = Theta_s_new(1:end-1,end-1);

phi_new(count_film1,ii) = 1;

fprintf(fid,'%0.8f',phi_new(count_film1,ii));

end % end loop ii

fprintf(fid,'\n');

circleparticle(0,0,phi_new(count_film1,:),Angle_iter)

clearvars Theta_s_new % clear these variables so I can have more memory

end % end count_film1 ==1

for ii = 1:Angle_iter

% update phi, since the film started we need to update phi

phi_new(count_film1+1,ii)=runkut4(F_phi_dot,W_new_sl(count_film1,ii),phi_new(count_film1,ii),U_new_sl(count_film1,ii),theta(ii),dtauf1);

fprintf(fid,'%0.8f',phi_new(count_film1+1,ii)); % print to phi

end % for ii length theta

```

```

fprintf(fid, '\n');

%----- Absorption and Scattering of the particle

% need to recalculate the mie_scattering because now there is an additional layer and
because phi changes the absorption has to be recalculated every time

for i = 1:length_lambda

[C_abs_new(i)] = mie_scattering_f1(epsilon_m, epsilon_l, num_p, dp0*1e-9, dp1*1e-
9, phi_new(count_film1+1, end), lambda(i)*1e-9);

End

C_abs_f1 = sum(C_abs_new.*1e18); % with layer

%----- Temperature of particle

% solving Eq (A.21)-(A.23) --- NOT DEPENDENT ON X

Theta_p_new(end+1) = runkut3(F_Thetap_s, C_abs_f1, Theta_p_new(end), alpha_l, dtauf1); %
temperature of the particle

fprintf(fid2, '%.8f\n ', Theta_p_new(k)); % print to Theta_p

for ii = 1:Angle_iter

dy_f1 = [1:dyy_f1:phi_new(count_film1+1, ii)]; % dividing the film up into 10 spaces in the y
direction

if count_film1 == 1

w_old = 0;

else

w_old = W_new_sl(count_film1-1, ii);

end

if ii == 1

u_old = -U_new_sl(count_film1, 2);

```



```

else

u_old = U_new_sl(count_film1,ii-1);

end

W_new_sl(count_film1+1,ii)=runkut8(F_W_dot,phi_new(end,ii),W_new_sl(count_film1,ii),Th
eta_s_1(2+temp_iter11,ii,count_film1),Theta_film1(length(dy_f1)+2,ii,count_film1),w_old,U_
new_sl(count_film1,ii),theta(ii),phi_new(end,ii),dtauf1);

U_new_sl(count_film1+1,ii)=runkut5(F_U_dot,phi_new(end,ii),U_new_sl(count_film1,ii),u_ol
d,W_new_sl(count_film1+1,ii),theta(ii),dtauf1);

fprintf(fid88,'%e ',W_new_sl(count_film1+1,ii)); % print to W

fprintf(fid99,'%e,U_new_sl(count_film1+1,ii)); % print to U

%%%%%%%%%%%%%%%%%%%%%%%%%%%%%%%%%%%%%%%%%%%%%%%%%%%%%%%%%%%%%%%%%%%%%%%%%%%%%%

% Solving film temp profile - film 1 formation

%%%%%%%%%%%%%%%%%%%%%%%%%%%%%%%%%%%%%%%%%%%%%%%%%%%%%%%%%%%%%%%%%%%%%%%%%%%%%%

% boudnary condition from the paper without the

Theta_film1(1,ii,count_film1+1) = Theta_p_new(end); % particle temperature

Theta_film1(2,ii,count_film1+1)=Theta_film1(1,ii,count_film1+1)-
C_abs_f1*intensity*R_j/(pi*(dp0/2)^2*T_inf); %BC with resistance

if length(dy_f1)<=2

Theta_film1(3:end,ii,count_film1+1)=Theta_film1(2,ii,count_film1+1);

end

for iii = 3:length(dy_f1)

Theta_film1(iii,ii,count_film1+1)=runkut5(F_Thetam_f,Theta_film1(iii+1,ii,count_film1),Thet
a_film1(iii,ii,count_film1),Theta_film1(iii-1,ii,count_film1),1+(iii-2)*dyy_f1,theta(ii),dtauf1);

% fourth order RK for time step

```

```

end % loop over y direction for film, loop iii

Theta_film1(iii+1:end,ii,count_film1+1)=Theta_film1(iii,ii,count_film1+1);

%%%%%%%%%%%%%%%%%%%%%%%%%%%%%%%%%%%%%%%%%%%%%%%%%%%%%%%%%%%%%%%%%%%%%%%%

% Solving liquid medium temp profile - film 1 formation

%%%%%%%%%%%%%%%%%%%%%%%%%%%%%%%%%%%%%%%%%%%%%%%%%%%%%%%%%%%%%%%%%%%%%%%%

%this is for making sure we have the correct data for the step in space

if (1-phi_new(count_film1+1,ii))~=0

AA = abs(1-phi_new(count_film1+1,ii))/dR;

dR_change = abs(AA-ceil(AA))*dR;

temp_iter11 = floor(AA); % temp iteration for the solid area

end

% calculating the angle shift

shift_time = phi_new(count_film1+1,ii)-phi_new(count_film1,ii);

shift = (phi_new(count_film1+1,length(theta))-phi_new(count_film1+1,1))/2;

angle_shift = abs(theta(ii)-theta(1)-pi/2);

change_111 = asin(cos(angle_shift)*shift/(1+shift_time));

% -----

Theta_s_1(1+temp_iter11,ii,count_film1+1) =Theta_film1(length(dy_f1)+2,ii,count_film1+1);

Theta_s_1(2+temp_iter11,ii,count_film1+1) = Theta_s_1(1+temp_iter11,ii,count_film1+1)-

dyy_f1*alpha_l*rho_l*h_sl/(T_inf*lambda_l)*(W_new_sl(count_film1+1,ii)*cos(change_111)

+ U_new_sl(count_film1,ii)*sin(change_111));

for jjj = 3:R_iter-1-temp_iter11

```

```

theta_s_temp=runkut5(F_Thetam_s1,Theta_s_1(jjj+temp_iter11+1,ii,count_film1),Theta_s_1(
jjj+temp_iter11,ii,count_film1),Theta_s_1(jjj+temp_iter11-1,ii,count_film1),
1+(jjj+temp_iter11-2)*dR,theta(ii),dtauf1); % fourth order RK for time step
if theta_s_temp >= T_initial/T_inf
Theta_s_1(jjj+temp_iter11,ii,count_film1+1) = theta_s_temp;
else
Theta_s_1(jjj+temp_iter11,ii,count_film1+1) = T_initial/T_inf;
end % end the if statement temp_s_temp
end % end jjj statement for the y
end % end length theta ii
count_film1 = count_film1 + 1; % how many iterations after the filmed formed
fprintf(fid88,'\n'); % print to W
fprintf(fid99,'\n'); % print to U
%print to file
if mod(count_film1,1000) == 0 % prints every 1000 counts
fprintf('count_film1 = %d and k = %d\n',count_film1,k)
string_count = num2str(count_film1);
name3 = strcat('Theta_film1_solid_',string_dp,string1,string2,string_count,'.txt');
name4 = strcat('Theta_s1_solid_',string_dp,string1,string2,string_count,'.txt');
fid3 = fopen(name3,'w');
fid4 = fopen(name4,'w');
for i = 1:length(dy_f1)+2
for ii = 1:Angle_iter
fprintf(fid3,'%0.8f',Theta_film1(i,ii,count_film1));

```

```

end % end ii

fprintf(fid3,'\n');

end % end i

temp_iter11

for iv = 1:size(Theta_s_1,1)

for ii = 1:Angle_iter

fprintf(fid4,'%0.8f',Theta_s_1(iv,ii,count_film1));

end

fprintf(fid4,'\n');

end

circle(0,0,phi_new(end,:),Angle_iter)

end % end mod

else

sprintf('particle 89% critical temperature reached')

break

end % if state for theta_p_new_film

end %loop for k(for tau)

end % end of main

%%%%%%%%%%%%%%%%%%%%%%%%%%%%%%%%%%%%%%%%%%%%%%%%%%%%%%%%%%%%%%%%%%%%%%%%

% RUNGA KUTTA FUNCTIONS

%%%%%%%%%%%%%%%%%%%%%%%%%%%%%%%%%%%%%%%%%%%%%%%%%%%%%%%%%%%%%%%%%%%%%%%%

function yy = runkut3(F_xy,x,y,z,h) %(updating y)

% this function performs 1 iteration of the runga kutta method. This is

% done because everything is coupled so we are going to have to do this

```

```

% several times.

k_1 = F_xy(x,y,z);
k_2 = F_xy(x,y+0.5*h*k_1,z);
k_3 = F_xy(x,y+0.5*h*k_2,z);
k_4 = F_xy(x,y+k_3*h,z);
yy = y + (1/6)*(k_1+2*k_2+2*k_3+k_4)*h; % updates y
end

function yy = runkut4(F_xy,x,y,z,zz,h) %(updating y)

% this function performs 1 iteration of the runga kutta method. This is
% done because everything is coupled so we are going to have to do this
% several times.

k_1 = F_xy(x,y,z,zz);
k_2 = F_xy(x,y+0.5*h*k_1,z,zz);
k_3 = F_xy(x,y+0.5*h*k_2,z,zz);
k_4 = F_xy(x,y+k_3*h,z,zz);
yy = y + (1/6)*(k_1+2*k_2+2*k_3+k_4)*h; % updates y
end

function yy = runkut5(F_xy,x,y,z,zz,xx,h) %(updating y)

% this function performs 1 iteration of the runga kutta method. This is
% done because everything is coupled so we are going to have to do this
% several times.

k_1 = F_xy(x,y,z,zz,xx);
k_2 = F_xy(x,y+0.5*h*k_1,z,zz,xx);
k_3 = F_xy(x,y+0.5*h*k_2,z,zz,xx);

```

```

k_4 = F_xy(x,y+k_3*h,z,zz,xx);

yy = y + (1/6)*(k_1+2*k_2+2*k_3+k_4)*h; % updates y

end

function yy = runkut7(F_xy,x,y,z,zz,xx,xxx,zzz,yyy,h) %(updating y)

% this function performs 1 iteration of the runga kutta method. This is
% done because everything is coupled so we are going to have to do this several times.

k_1 = F_xy(x,y,z,zz,xx,xxx,zzz,yyy);

k_2 = F_xy(x,y+0.5*h*k_1,z,zz,xx,xxx,zzz,yyy);

k_3 = F_xy(x,y+0.5*h*k_2,z,zz,xx,xxx,zzz,yyy);

k_4 = F_xy(x,y+k_3*h,z,zz,xx,xxx,zzz,yyy);

yy = y + (1/6)*(k_1+2*k_2+2*k_3+k_4)*h; % updates y

end

function circleparticle(x,y,r,number)

%x and y are the coordinates of the center of the circle

%r is the radius of the circle

%0.01 is the angle step, bigger values will draw the circle faster but
%you might notice imperfections (not very smooth)

hold on

ang=linspace(0-pi/2,2*pi-pi/2,number-1);

rr = [r(1:end-1),fliplr(r)];

xp=rr.*cos(ang);

yp=rr.*sin(ang);

plot(x+xp,y+yp);

fill(x+xp,y+yp,'y');

```

```

end

function circle(x,y,r,number)

%x and y are the coordinates of the center of the circle r is the radius of the circle

%0.01 is the angle step, bigger values will draw the circle faster but

%you might notice imperfections (not very smooth)

hold on

ang=linspace(0-pi/2,2*pi-pi/2,2*number-1);

flippy = fliplr(r);

rr = [r(1:end-1),flippy];

xp=rr.*cos(ang);

yp=rr.*sin(ang);

plot(x+xp,y+yp);

end

```

The next two codes are supplemental codes that give the particle properties and medium properties.

```

function particle_properties(kind)

global rho_p c_p lambda_p R_j T_melt_p string1

if kind == 1 % parameters for GOLD particles

rho_p = 19.32e3*1e-27; % [kg/m^3 ==>kg/nm^3] density of particle

c_p = 129.1*1e18; % [J/(kg K) ==> nm^2/s^2 K] heat capacity of particle

lambda_p = 318*1e9; % [W/m K ==> kg nm/s^2 K] thermal conductivity of particle

```

```

T_melt_p = 1080; %[K] melting temp of particle

R_j = 15e-9; % [m^2 K/W ==> s^3/K kg] resitance from Jerrys work - thesis spread sheet

string1 = '_Gold_particle_';

sprintf(string1)

elseif kind == 2 % silver

rho_p = 10490*1e-27; % [kg/m^3 ==>kg/nm^3] density of particle

c_p = 235*1e18; % [J/(kg K) ==> nm^2/s^2 K] heat capacity of particle

lambda_p = 429*1e9; % [W/m K ==> kg nm/s^2 K] thermal conductivity of particle

T_melt_p = 1234.8; %[K] melting temp of particle

R_j = 5e-9; % [m^2 K/W ==> s^3/K kg] resitance from Jerrys work - thesis spread sheet

string1 = '_Silver_particle_';

sprintf(string1)

elseif kind == 3 % copper

rho_p = 8940*1e-27; % [kg/m^3 ==>kg/nm^3] density of particle

c_p = 384.4*1e18; % [J/(kg K) ==> nm^2/s^2 K] heat capacity of particle

lambda_p = 395.7*1e9; % [W/m K ==> kg nm/s^2 K] thermal conductivity of particle

T_melt_p = 1358; %[K] melting temp of particle

R_j = 5e-9; % [m^2 K/W ==> s^3/K kg] resitance from Jerrys work - thesis spread sheet

string1 = '_Copper_particle_';

sprintf(string1)

elseif kind == 4 % Aluminum

rho_p = 2.7e3*1e-27; % [kg/m^3 ==>kg/nm^3] density of particle

c_p = 904*1e18; % [J/(kg K) ==> nm^2/s^2 K] heat capacity of particle

lambda_p = 247*1e9; % [W/m K ==> kg nm/s^2 K] thermal conductivity of particle

```



```

T_melt_p = 933.3; %[K] melting temp of particle

R_j = 2.5e-9; % [m^2 K/W ==> s^3/K kg] resitance from Jerrys work - thesis spread sheet

string1 = '_Aluminum_particle_';

sprintf(string1)

elseif kind == 5 % parameters for Si/Au nanoshells particles

rho_p = 19.32e3*1e-27; % [kg/m^3 ==>kg/nm^3] density of particle

c_p = 129.1*1e9; % [J/(kg K) ==> nm/s^2 K] heat capacity of particle

lambda_p = 318*1e18; % [W/m K ==> kg nm^2/s^2 K] thermal conductivity of particle

T_melt_p = 1080; %[K] melting temp of particle

R_j = 15e-9; % [m^2 K/W ==> s^3/K kg] resitance from veras work

string1 = '_Nanoshell_particle_';

sprintf(string1)

elseif kind == 6 % parameters for Graphite particles

lambda_p = 1.5e3*1e-27; % [kg/m^3 ==>kg/nm^3] density of particle

c_p = 846*1e18; % [J/(kg K) ==> nm^2/s^2 K] heat capacity of particle

lambda_p = 300*1e9; % [W/m K ==> kg nm/s^2 K] thermal conductivity of particle

T_melt_p = 3823; %[K] melting temp of particle

R_j = 0; % [m^2 K/W ==> s^3/K kg] - didnt have for graphite

string1 = '_Graphite_particle_';

sprintf(string1)

end

end % end function

function medium_properties(kind)

```

```

global rho_s rho_l rho_v c_s c_l c_v lambda_s lambda_l lambda_v mu_l mu_s epsilon_m
epsilon_l epsilon_v n_med_s n_med_l h_sl h_lv R_v gamma_lv a dsigma T_boil T_melt_m T_crit
T_inf string2

if kind == 1

% water solid/liquid variables are jumbled because we are going
% from solid to liquid

rho_s = 1000*1e-27;% % rho_s [kg/m^3 ==> kg/nm^3] density of solid
rho_l = 997*1e-27;% % [kg/m^3 ==> kg/nm^3] density of liquid
rho_v = .598*1e-27; % [kg/m^3 ==> kg/nm^3] density of vapor
c_s = 2050*1e18; % [J/(kg K) ==> nm^2/s^2 K] heat capacity of solid
c_l = 4.2159e3*1e18; % [J/(kg K) ==> nm^2/s^2 K] heat capacity of liquid
c_v = 2.0e3*1e18; % [J/(kg K) ==> nm^2/s^2 K] heat capacity of vapor
lambda_s = 2.22*1e9; % [W/m K ==> kg nm/s^3 K] thermal conductivity of solid
lambda_l = 0.68*1e9; % [W/m K ==> kg nm/s^3 K] thermal conductivity of liquid
lambda_v = .05*1e9; % [W/m K ==> kg nm/s^3 K] thermal conductivity of vapor
mu_l = 1e-3*1e-9; % [Pa s ==> kg/s nm] dynamic viscosity
mu_s = 1308e-3*1e-9; % [Pa s ==> kg/s nm] dynamic viscosity
epsilon_m = 3.18; % [] permittivity of the medium
epsilon_l = 1.78; % [] permittivity of the medium
epsilon_v = 1.2; % [] permittivity of the medium
n_med_s = 1.309; %index of refraction of solid
n_med_l = 1.333; %index of refraction of water
h_sl = 334e3*1e18; % h_sl [J/kg ==> nm^2/s^2] latent heat for melting
h_lv = 2260e3*1e18; % [J/kg ==> nm^2/s^2] latent heat for evaporation

```

```

R_v = 8.3144621*(1/18.02)*1e3*1e18; % [J/kg K ==> nm^2/s^2 K] mass specific heat gas
constant [molar mass for water 18.02g=1mol]

gamma_lv = 67.91e-3; % [N/m ==> kg/s^2] interfacial energy between the liquid and vapor
phase found using wiki

a = 0.1*1e-6*1e9; % [micro m = 1e-10 m ==> nm]the molecular diameter

dsigma = 8.6e-3; % [kg/s^2] the van der wall energies

T_boil = 100+273; %[K] room temp

T_melt_m = 273+0; %[K] critical temp

T_crit = 580; %[K] critical temp

T_inf = 383; %[K] room temp

string2 = '_water_';

sprintf(string2)

elseif kind == 3

% n-octadecane solid/liquid variables are jumbled because we are going

% from solid to liquid

%https://www.thermalfluidscentral.org/encyclopedia/index.php/Thermophysical_Propert
ies:_Phase_Change_Materials

rho_s = 814*1e-27; %; % rho_s [kg/m^3 ==> kg/nm^3] density of solid

rho_l = 744*1e-27; % [kg/m^3 ==> kg/nm^3] density of liquid

rho_v = 8.73*1e-27; % [kg/m^3 ==> kg/nm^3] density of vapor

c_s = 2.15e3*1e18; % [J/(kg K) ==> nm^2/s^2 K] heat capacity of solid

c_l = 2.18e3*1e18; % [J/(kg K) ==> nm^2/s^2 K] heat capacity of liquid

c_v = 2.00e3*1e18; % [J/(kg K) ==> nm^2/s^2 K] heat capacity of liquid

lambda_s = 0.358*1e9; % [W/m K ==> kg nm/s^3 K] thermal conductivity of solid

```

```

lambda_l = 0.148*1e9; % [W/m K ==> kg nm/s^3 K] thermal conductivity of liquid
lambda_v = 0.10*1e9; % [W/m K ==> kg nm/s^3 K] thermal conductivity of liquid
mu_s = 773e-6*1e-9; % [Pa s ==> kg/s nm] dynamic viscosity
mu_l = 3.9e-3*1e-9; % [Pa s ==> kg/s nm] dynamic viscosity????
epsilon_m = 2.149; % [] permittivity of the solid
epsilon_l = 2.065; % [] permittivity of the liquid
epsilon_v = 2.0; % [] permittivity of the vapor
n_med_s = 1.4390; %index of refraction
n_med_l = 1.4390;
h_sl = 244e3*1e18; % h_sl [J/kg ==> nm^2/s^2] latent heat for melting
h_lv = 356*1e3*1e18; % [J/mol]-->[J/kg ==> nm^2/s^2]
R_v = 8.3144621*(1/254.4943)*1e3*1e18; % [J/kg K ==> nm^2/s^2 K] not needed
gamma_lv = 27.9*0.001; % [dyne/cm]-->[N/m ==> kg/s^2]
a = 0.12*1e-10*1e9; % [A = 1e-10 m ==> nm] the molecular diameter
dsigma = 9.6e-3; % [kg/s^2] the van der wall energies
T_boil = 317+273; % [K] room temp
T_melt_m = 28+273; % [K] critical temp
T_crit = 747; % [K] critical temp
T_inf = 20+273; % [K] room temp
string2 = '_N-ocadectane_medium';
sprintf(string2)
end
end

```

Appendix C

C.1 Construction for the 'hybrid' Nanofluid

Chapter 3 gives an idea of a recipe for optimizing a mixture of nanofluid when exposed to radiation. Because of the plasmonic properties, various metals are capable of tuning the amount of absorption or scattering a particle can have when changing the size, shape, composition, and medium that the particle is in. Because of this, having various types of particles in the nanofluid is considered. This appendix repeats the equations for this project and a little more detail of the algorithm that was outlined in Chapter 3.

A pictorial idea of a solar collector model is presented in Fig. C.1.1 to give an idea of the mathematical model provided. A nanofluid between an adiabatic surface and a transparent glass is heated through convection and radiation. In Fig. C.1.1 , H is height, $L=1\text{ m}$ is the length, and the radiative heat flux is q_r . The fluid is considered to be stagnant.

The black body intensity radiation is calculated by, $I_{b,\lambda} [W/m^2]$, defined by [103]

$$I_{b,\lambda}(\lambda, T) = \frac{2hc_0^2}{\lambda^5 \left[\exp\left(\frac{hc_0}{\lambda k_B T}\right) - 1 \right]} \quad (C.1.1)$$

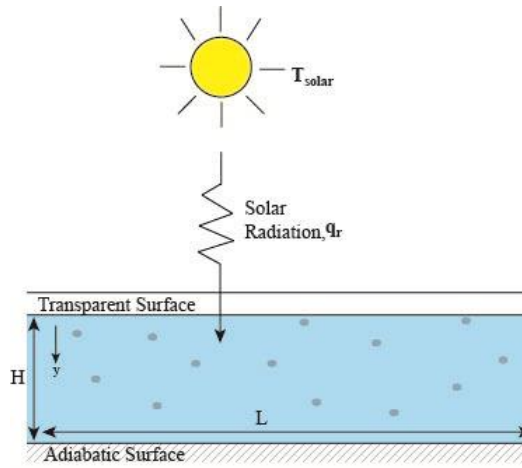


Figure C.1.1 Solar heating of a nanofluid

In this expression, $h = 6.626 \times 10^{-34} \text{ J} \cdot \text{s}$ is Planck's constant, $c_0 = 3 \times 10^8 \text{ m/s}$ is the speed of light in a vacuum, $k_B = 1.38 \times 10^{-23} \text{ m}^2 \text{kg} / \text{s}^2 \text{K}$ is Boltzmann's constant, $\lambda [m]$ is the wavelength, and $T [K]$ is the temperature. The intensity is assumed to be isotropic with no in-scattering term. Figure C.1.2 gives an idea of Eqn. (C.1.1) with $T = 5800K$. This temperature can vary depending on the application. The direction of the intensity is only in the y-direction because the x-direction is infinitely long [103]. The intensity expression varying through y is given by

$$\frac{\partial I_\lambda}{\partial y} = -\sigma_{abs,\lambda} I_\lambda \quad (C.1.2)$$

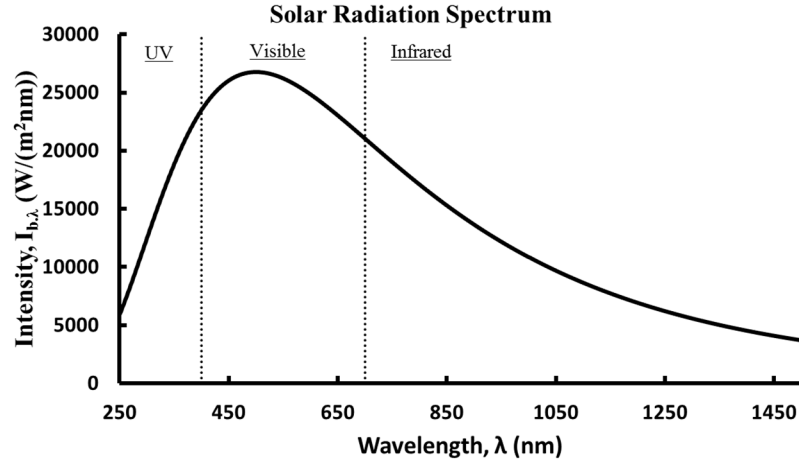


Figure C.1.2 Solar radiation spectrum using Eqn. (C.1.1)

where $\sigma_{abs,\lambda} = \sigma_{abs,f} + \sigma_{abs,p,tot}$ is the absorption for the fluid and particles and described later. Equation (C.1.2) describes the spectral intensity involving the absorption of the nanofluid. The boundary conditions at the top of the container is assumed defined by Eqn. (C.1.1),

$$I_{\lambda}(y = 0) = I_{b,\lambda} \quad (C.1.3)$$

In these applications, the highest absorption of incoming heat is desired; therefore, the expression that is are optimized is given by

$$\left(\sigma_{abs,f} + \sigma_{abs,p,tot} \right) I_{b,\lambda} \quad (C.1.4)$$

The absorption term for a pure fluid, $\sigma_{abs,f}$, is the attenuation coefficient used in the Beer-Lambert law [77]

$$\sigma_{abs,\lambda,f} = \frac{4\pi\kappa}{\lambda} \quad (C.1.5)$$

where κ is the absorption index. Values for κ are found [104,105]. The ‘hybrid’ nanoparticle absorption coefficients are defined using

$$\begin{aligned} \sigma_{a,\lambda,p,tot} &= \sum_j \sigma_{a,\lambda,p,j} = \sum_j \frac{6\phi_j C_{abs,j}}{\pi d_j^3} \\ \phi_{tot} &= \frac{\sum_j n_j V_{p,j}}{\sum_j n_j V_{p,j} + V} = \sum_j \phi_j \end{aligned} \quad (C.1.6)$$

the parameter, ϕ_{tot} , is the volume fraction of the particles, d [m] is the diameter of the particles, n is the amount of each type of particle, V_p and V [m³] are the volume of the particle and fluid, respectively, and $C_{abs,j}$ [m²] is the cross section for each particle [46,103] described in Appendix D.3 and the MATLAB code is found in Appendix D.7.

In the ‘hybrid’ nanofluid, there are distinct volume fractions, diameters, and absorption and scattering cross sections for each type of particle. The summation part in Eqn. (C.1.6) includes the summation of all the properties over the number of particle types, j . The radiative heat flux is determined by integrating the intensity over all possible directions and wavelengths as shown

$$q_r = 4\pi \int_0^{2\mu m} I_\lambda d\lambda \quad (C.1.7)$$

C.2 Optimization for the ‘hybrid’ Nanofluid

The recipe for optimization is provided. Assume a given temperature, $T_{input} = 5800\text{K}$, and wavelength range, $\lambda = [\lambda_{min}, \lambda_{max}] = [200, 1000]\text{nm}$. If using a different temperature and wavelength range, then the results will be altered. Different heights, $H = [1.2 \times 10^{-5}, 1.2 \times 10^{-4}, 1.2 \times 10^{-3}, 1.2 \times 10^{-2}, 1.2 \times 10^{-1}]$ m, number of particles you wish to use, $N = [1, 2, 3, 4, 5]$, and concentrations, $\phi = [1 \times 10^{-6}, 1 \times 10^{-5}, 1 \times 10^{-4}, 1 \times 10^{-3}, 1 \times 10^{-2}, 1 \times 10^{-1}]$, were considered. For this section, the term database is used. When referring to this, it implies the types of particles and their sizes considered. A researcher may not have access to gold nanoparticles and therefore, the gold nanoparticles would be left out of the database. Refer to Fig. C.1.1 to understand that the H represents the height of the container in which the nanofluid is in. The following steps for the algorithm were taken:

- 1) Create a database by finding the absorption, Q_{abs} , over your desired wavelength range, using Eqns. 8-12, for all particles and diameters you wish to consider. For this problem, Au, Cu, Al, SiO₂/Au Shell nanoparticles, and Graphite were

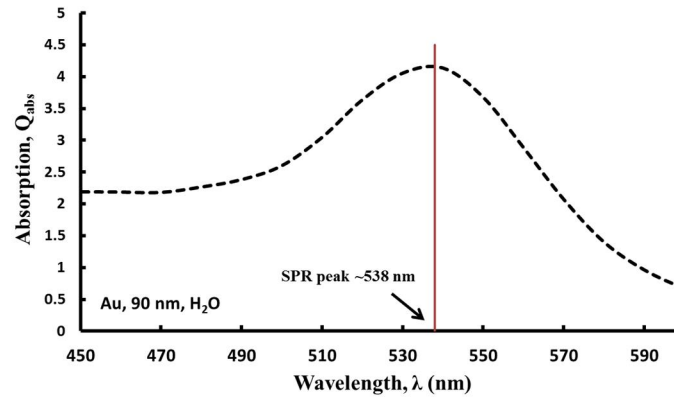


Figure C.2.1 Description of the SPR peak

considered with diameters ranging from $d = [10, 30, \dots, 130, 150]$ nm. When calculating the shell nanoparticles, the shell thickness was 5 nm. Calculate $\sigma_{abs, particles, j}$ and find the SPR peaks for all of the absorption curves for all the particles and diameters. The SPRE peak is the wavelength where the maximum absorption occurs. Figure C.2.1 gives an idea of what the SPR peak is for an absorption curve of a gold 90nm particle in water.

- 2) Calculate the absorption of the fluid, $\sigma_{abs, f}$, using Eqn. (C.1.5).
- 3) Integrate the blackbody radiation over the whole wavelength range

$Area_tot = \int_{\lambda} I_b d\lambda$. The trapezoidal rule was used to calculate this.

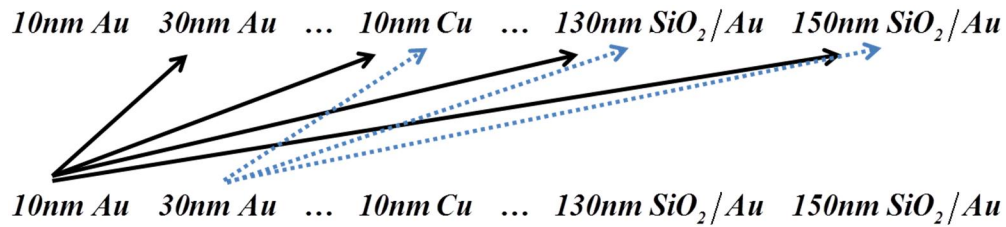


Figure C.2.2: Idea of a combination

- 4) Consider all combinations of particles, $\binom{\text{database}}{N}$. For each combination steps a and b are considered. A combination is a way of collecting or grouping items such that the order does not matter. This means given a database, choose a combination with N number of components. There are many different combinations; however, you do not include the repeated mixtures. Refer to Fig. C.2.2 which shows a combination for $N=2$. In this figure, a 10nm Au particle is grouped with the all the other particles as seen represented by the black arrows. Next, 30 nm Au particle will be grouped with the other particles except the ones that are repeated. In this case, 10 nm Au particles and 30nm Au particles are not included as seen in the dotted arrows. This continues until all mixtures are considered. The number within the combination grows as N grows.
- a) Find the percentage, P_j , of the total concentration for each type of particle.
 - i) Sort the SPR peaks, found in step 1 which correspond to the specific combination and find the median between the peaks. Use the medians, along with the initial and final wavelength in which you are considering,

to create an interval of wavelengths, i.e. $[\lambda_{\min}, \text{median}, \lambda_{\max}]$. For example, if considering 2 particles types of Au 90 nm particles and 50 nm SiO₂/Au nanoshells. The SPR peaks of these particles are 520 nm and 920 nm, respectively. The median is of these two SPR peaks associated with these particles is 720 nm. The interval is then [200,710,1000]nm. Refer to Fig. C.2.3.

- ii) Integrate $I_{b,\lambda}$ over the interval range found in step i), $A_j = \int_{\lambda_j}^{\lambda_{j+1}} I_b d\lambda$.

Note: This is similar to the fraction of blackbody emissive power found in radiations books [103,112]. Refer to Fig. C.2.3 to understand the meaning of A_j .

- iii) Divide the area for the different intervals found in step (ii) over that of the total found in step 3 to find percentages of the total concentration for

each particle type, $P_j = \frac{A_j}{Area_{tot}}$.

- b) Calculate $area = \int_{\lambda} \left(\sum_j P_j \sigma_{abs,p,j} + \sigma_{abs,f} \right) I_b d\lambda$ for each combination.

- 5) Sort the combinations and choose the mixture with the greatest value for the area. Make sure all the diameter sizes and particle types are tracked.
- 6) Calculate the intensity, I_{λ} , and radiation, q_r , using Eqns. (C.1.2) and (C.1.7), respectively.

7) Record the value of q_r which corresponds to the bottom of the liquid container.

This value helps to determine whether the radiation reaches the bottom of the container or if the radiation is terminated before it reaches the full liquid height.

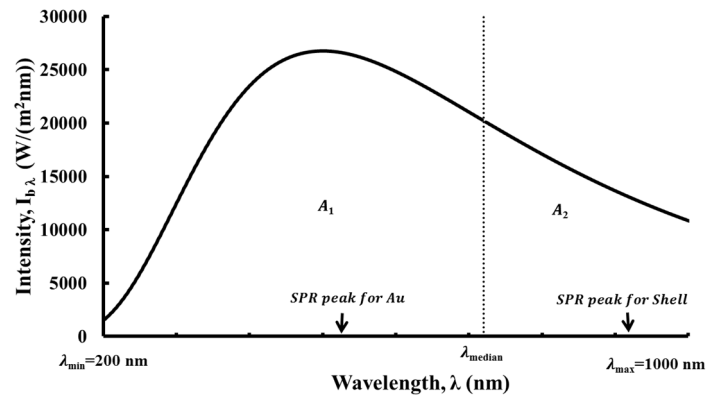


Figure C.2.3 Description of A_j

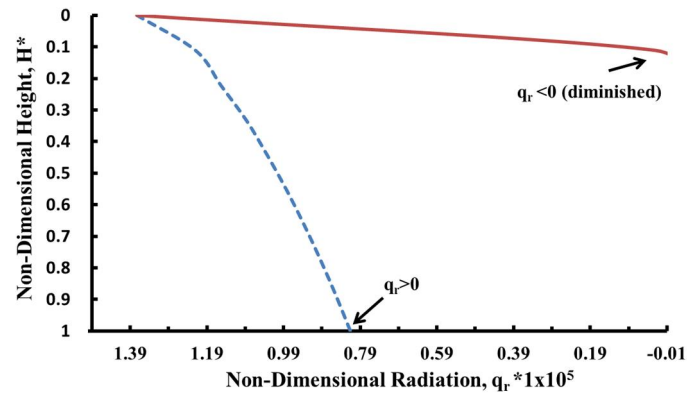


Figure C.2.4 Description of when q_r is diminished of when q_r penetrated through the fluid and reached the bottom surface.

These steps are repeated for every concentration, ϕ . Once this is done, use the values found in step 7 and determine which is closest to 0. When having a value >0 implies that the radiation used is greater than necessary and backscattering can occur at the bottom of the surface of the container. Backscattering from the bottom of the surface is not considered. If the value is <0 , implies that the intensity did not penetrate all the way through the container. Figure C.2.4 gives two examples of when q_r is diminished and when the radiation is >0 and backscattering can occur. The y-axis is the non-dimensional height value. For $H^*=0$, implies the top of the container and $H^*=1$ references the bottom of the container. Repeat the steps for number of particles, N , and height, H . Figure C.2.5 gives an outline of the process described here.

Pick a Temperature, T_{input} , and a specific wavelength $\lambda = [\lambda_{min}, \lambda_{max}]$

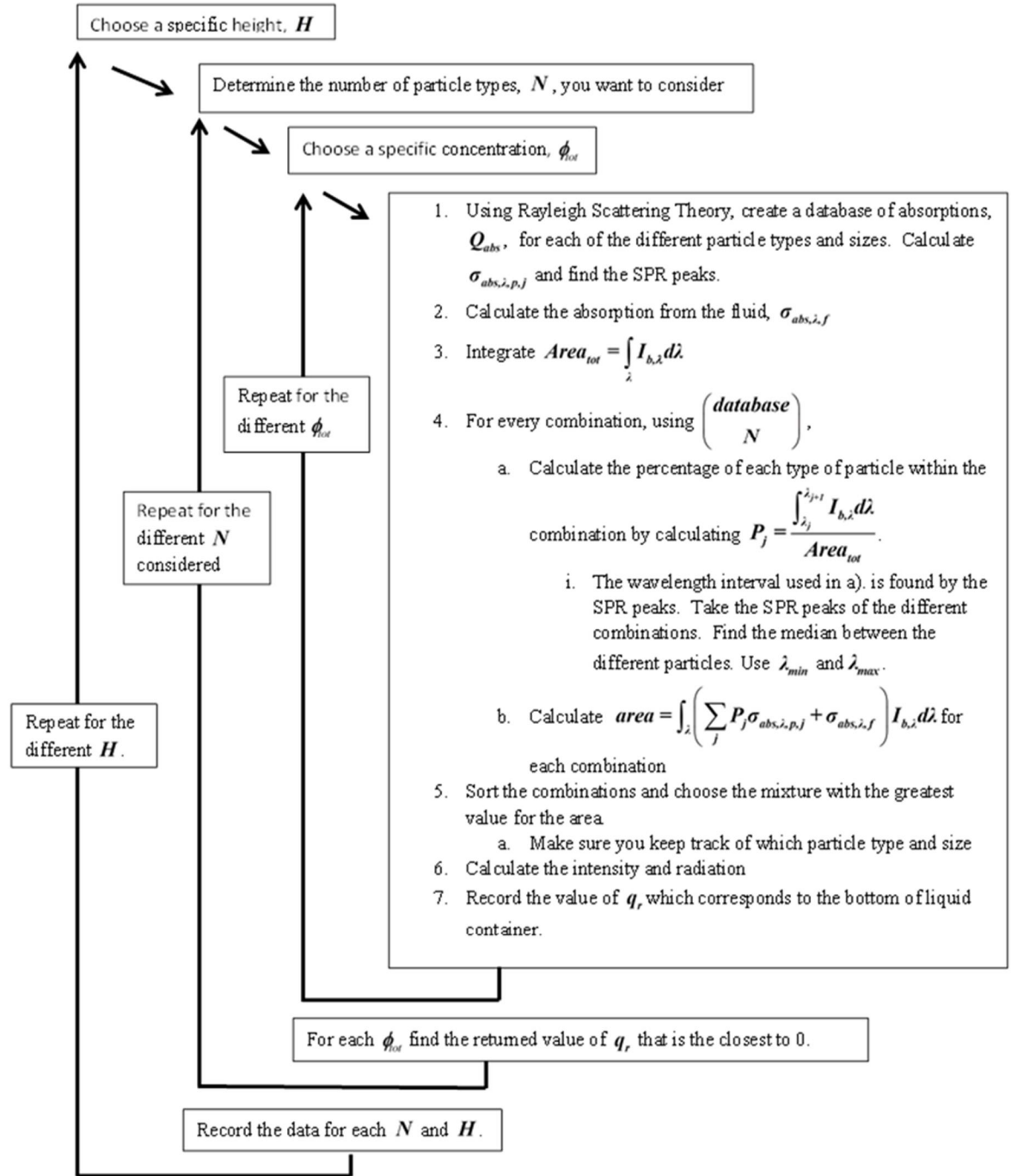


Figure C.2.5: Algorithm for the hybrid nanofluid

C.3 Code for describing the optimization of the hybrid nanofluid

In this section, the code that describes the optimization of the hybrid nanofluid is presented. This program has a main function, *main_hybrid.m*, which calls another function, *hybrid_function_optimization.m*. The program was written in MATLAB. Note: This function also references *mie_scattering.m*. This program is found in Appendix D.7.

```
function main_hybrid()

% This is the main function that calls hybrid_function_optimization.m

number_of_particles = [2]; %[1,2,3,4,5]

phi = [1e-6,1e-5,1e-4,1e-3,1e-2,1e-1];

H = [1.2e-5,1.2e-4,1.2e-3,1.2e-2,1.2e-1]; %[m]

% TO CHANGE T_input you must change temp twice in other file!!

T_input = 5800;

fprintf('T_input = %d K\n',T_input);

radiation = zeros(length(phi),length(number_of_particles));

for k = 1:length(H) %loops over height

fprintf('Height of fluid = %e m\n',H(k));

for i = 1:length(number_of_particles) % loops over N

fprintf('number of particles = %d\n',number_of_particles(i));

string2 = {};

for j = 1:length(phi) % loops over phi

[value,stringss]=hybrid_function_optimization(phi(j),number_of_particles(i),H(k));
```



```

string2 = [string2 ; stringss'];

radiation(j,i,k)=value;

end % end for loop j

string2

end% end for loop i

end% end for loop k

% helps to determine which q is closest to 0.

for k = 1:length(H)

for i = 1:length(number_of_particles)

temp_neg = find(radiation(:,i,k)<0);

temp_pos = find(radiation(:,i,k)>0);

if size(temp_neg,1)==0

temp_2 = temp_pos(end);

elseif size(temp_pos,1)==0

temp_2 = temp_neg(1);

elseif temp_pos(end)+temp_neg(1)>0

temp_2 = temp_neg(1);

elseif temp_pos(end)+temp_neg(1)<0

temp_2 = temp_pos(end);

end % end if loop

end % end for loop i

phi_choose = phi(temp_2);

%prints out the data

for i = 1:length(number_of_particles)

```

```

fprintf('%d number of particles with phi_total = %.2e for T_input=%d K with H =
%.2e\n',number_of_particles(i),phi_choose(i),T_input,H(k))

end % end for loop i

end % end for loop k

end % end function

function[radiation_bottom,string_used]=hybrid_function_optimization(phi_tot,num_of_parti
cles,H)

% This program calls myfun, mie_scattering.m,
% This is a call function.
% This function helps to optimize the hybrid method.

% input variables

%   phi_tot --- the total concentration
%   num_of_particles --- N (the number within your mixture)
%   H --- the height of the container (m)

% output variables

%   radiation_bottom --- the radiation calculated at the bottom (-)
%   string_used --- gives the mixture of particles in a string

% It also has properties for 5 different kinds of metals

%   num == 1 ---> gold
%   num == 3 ---> copper
%   num == 4 ---> aluminum
%   num == 5 ---> nanoshells Si/Au

```

```

% num == 6 ---> graphite

%%%%%%%%%%%%%%%%%%%%%%%%%%%%%%%%%%%%%%%%%%%%%%%%%%%%%%%%%%%%%%%%%%%%%%%%

% num_of_particles = 5;

phi = phi_tot;%phi_tot/num_of_particles; %concentration

H = H*1e9; % [nm] height of the tank (1.2e-6 m)

% % % % % Properties for the particle

num = [1,3,4,6,5]; % which particles in the nanofluid

diameter = [10:20:150]; % [m] diameter FOR ALL THE PARTICLES

d_1 = zeros(1,length(num)*(length(diameter)));

d_1(end-length(diameter)+1:end) = diameter-5;

string = [{'Au'},{'Cu'},{'Al'},{'Graphite'},{'Shell'}];

% % % % % Solar temperature to find Ib

T_input = 5800; %[K] solar temperature

lambda = [200:10:1000]; %--[100,2000] nm over all the wavelengths in the solar region

dlambda = abs(lambda(1)-lambda(2)); % step in wavelength

%%%%%%%%%%%%%%%%%%%%%%%%%%%%%%%%%%%%%%%%%%%%%%%%%%%%%%%%%%%%%%%%%%%%%%%% Known constants for Ib

h_p = 6.626e-34*1e18; % [J s] ==> [kg nm^2/s] plancks constant

c = 3e8*1e9; % [m/s] ==> [nm/s] speed of light in vacuum

kb = 1.38e-23*1e18; % [m^2kg/s^2K] ==> [nm^2kg/s^2K] Boltzmann's constant

sigma_b = 5.67e-8; % [W/m^2 K^4] ==> [kg/s^3 K^4] Stefan Boltzmann Constant

G = 1343.9;%1000; % [W/m^2 == kg/s^2] incident solar flux

% % % % % Properties for container the nanofluid is in

L = 1e9; % [nm] length of the tank

w = 1e9; % [nm] the width of the fluid

```

```

V = H*L*w; % [nm^3] initial volume of the fluid

%%%%%%%%%%%%%%%%%%%%%%%%%%%%%%%%%%%%%%%%%%%%%%%%%%%%%%%%%%%%%%%%%%%%%%%%

% ----- fluid properties for water

%%%%%%%%%%%%%%%%%%%%%%%%%%%%%%%%%%%%%%%%%%%%%%%%%%%%%%%%%%%%%%%%%%%%%%%%

rho_f = 997e-27; % [kg/nm^3] density of fluid

c_f = 4215.9*1e18; % [J/kg K] ==>[nm^2/s^2 K] specific heat of fluid

k_f = 0.68*1e9; % [W/m K] ==> [kg nm/s^3 K] thermal conductivity of fluid

epsilon_m = 1.78; % dielectric for fluid

epsilon = 0.98;

nn = 1.33; % index of refraction

%%%%%%%%%%%%%%%%%%%%%%%%%%%%%%%%%%%%%%%%%%%%%%%%%%%%%%%%%%%%%%%%%%%%%%%%

%%%%%%%%%%%%%%%%%%%%%%%%%%%%%%%%%%%%%%%%%%%%%%%%%%%%%%%%%%%%%%%%%%%%%%%% Absorption

%%%%%%%%%%%%%%%%%%%%%%%%%%%%%%%%%%%%%%%%%%%%%%%%%%%%%%%%%%%%%%%%%%%%%%%%

% %absorption of fluid

for jj = 1:length(lambda)

%   http://en.wikipedia.org/wiki/Optical\_properties\_of\_water\_and\_ice

kappa = absorption_water(lambda(jj)*1e-9); %absorption index for water

C_abs_f(jj)=kappa*1e-9; % [1/nm] for fluid

end

% Gives the SPR peak for all the particle types and compositions

for n_p = 1:length(num)

for jj = 1:length(diameter)

for i=1:length(lambda)

```

```

xx(i,:)=mie_scattering(epsilon_m,num(n_p),diameter(jj)*1e-9,d_1(jj+(n_p-
1)*length(diameter))*1e-9,lambda(i)*1e-9); %gives you Q
end

temp_matrix = [xx(:,1),lambda']; %this is going to help find the SPR

[sorting,Index] = sortrows(temp_matrix,1); %this sorts each row in decending order based
on absorption

SPR(jj,n_p)= sorting(end,2); % this gives the peak SPR and Peak absorption

Q_abs(:,jj+length(diameter)*(n_p-1)) = xx(:,1); %saves all the absorption for each particle

sigma(:,jj+length(diameter)*(n_p-1))=3*phi*Q_abs(:,jj+length(diameter)*(n_p-
1))./(2*diameter(jj)); % [m^-1]
end
end

Ib = (2*h_p*c^2)./[lambda.^5.*exp(h_p*c./(lambda.*kb*T_input)) - lambda.^5]; % [W/m^2]
blackbody radiation intensity

AREA_Ib = quad(@myfun,lambda(1),lambda(end)); % the area under the curve using trap
rule % the area under the curve using trap rule

combination = [];

counter = 1;

x = nchoosek(1:length(diameter)*length(num),num_of_particles); %gives the different
combinations

percent = zeros(size(x,1),size(x,2));

if size(x,2)==1

for ii = 1:length(x) % if N==1

percent(counter,num_of_particles)=1;

```

```

AREA(counter) = trapz(lambda,(sigma(:,ii)+C_abs_f).*Ib); % the area under the curve using
trap rule

combination(counter,1:num_of_particles) = x(ii,:);

counter = counter+1;

end % end ii

else % If N~=1

for ii = 1:size(x,1)

% find the interval to use based on the SPR peaks

temp_spr = SPR(x(ii,:));

[sorting_SPR_1,index_11] = sort(temp_spr); % sort in numerical order and index

for i = 1:length(temp_spr)-1

temp_SPR(i) = [sorting_SPR_1(i)+sorting_SPR_1(i+1)]/2; %the median

end

x_values = [lambda(1), temp_SPR,lambda(end)]; %wavelength x values

% Find the percentages based on the area

for kk = 1:size(x,2)

area_percentage = quad(@myfun,x_values(kk),x_values(kk+1)); % the area under the curve
using trap rule

percent(counter,kk) = area_percentage./AREA_Ib;

percent_sigma(:,kk) = percent(counter,kk)*sigma(:,x(ii,kk));

end

% Calculate the area of both (sigma + sigma_f)Ib after finding the %

AREA(counter) = trapz(lambda,(sum(percent_sigma,2)+C_abs_f').*Ib'); % the area under the
curve using trap rule

```

```

combination(counter,1:num_of_particles) = x(ii,:);

counter = counter+1;

end % end ii

end

%finding the max area and the correct combination to use

% create the name and keep track of percentage, particle type, and diameter

[sort_area,index]=sort(AREA);

combination = combination(index,:);

percent = percent(index,:);

name1 = {};

for jj = 0:4

particle_type = floor(combination(end-jj,:)/length(diameter))+1;

for ii = 1:num_of_particles

for_diameter(ii) = rem(combination(end-jj,ii),length(diameter));

if for_diameter(ii) == 0

for_diameter(ii) = length(diameter);

end

end

d = diameter(for_diameter);

% for printing the names of the particles, sizes, and percentages

for j = 1:num_of_particles

string_dp = num2str(d(j));

percent_print = num2str(percent(end-jj,j)*100);

name1(jj+1,j) = strcat(percent_print,'% ',string(particle_type(j)),string_dp,'nm');

```

[illegible]


```

%%%%%%%%%%%%%%%%%%%%%%%%%%%%%%%%%%%%%%%%%%%%%%%%%%%%%%%%%%%%%%%%%%%%%%%%
% calculated using a nondimensional q_r, I, and H
Y=linspace(0,1,10);
dyy = Y(2)-Y(1);
for i = 0:length(Y)-1 % dy*
% boundary condition at y = 0 for I and theta
if i+1 == 1
% wavelength (vector over all wavelength)
I_new_both_star(:,i+1)=Ib/G;
q(i+1) = 4*pi*sum(I_new_both_star(:,i+1).*dlambda); % sum over all wavelengths to find q
else % end if loop for i==0
% finite difference and integration over the whole spectrum and
I_new_both_star(:,i+1)=I_new_both_star(:,i)-
H*dyy*(sum(SIGMA,2)+C_abs_f').*I_new_both_star(:,i); % (dimensionless) VECTOR
q(i+1) = 4*pi*sum(I_new_both_star(:,i+1).*dlambda); % sum over all wavelengths to find q
end
end
radiation_bottom = q(end);
end % end of function

function f_Ib = myfun(wavelength)
% Ib function
h_p = 6.626e-34*1e18; % [J s] ==> [kg nm^2/s] plancks constant
c = 3e8*1e9; % [m/s] ==> [nm/s] speed of light in vacuum

```

```

kb = 1.38e-23*1e18; % [m^2kg/s^2K] ==> [nm^2kg/s^2K] Boltzmann's constant
sigma_b = 5.67e-8; % [W/m^2 K^4] ==> [kg/s^3 K^4] Stefan Boltzmann Constant
T_input = 5800; % [K] solar temperature
f_lb=(2*h_p*c^2)./[wavelength.^5.*exp(h_p*c./(wavelength.*kb*T_input))
wavelength.^5]; % [W/m^2] blackbody radiation intensity
end

```

Appendix D

D.1 Derivation for the Van Der Waal Equation

The Van Der Waal forces are the sum of the attractive or repulsive forces between the molecules. The expression used was based on Korber et al. between a spherical particle and a plane wall. A particle with radius r is moving a distance $d \ll r$ ahead of the solid liquid interface. The expression was based on the Gibb's free energy

$$\Delta G = G_{final} - G_{initial} = \left[\gamma_{sp} + (\gamma_{ls} - \gamma_{lp}) \right] C = \Delta \gamma_o C \quad (D.1.1)$$

where $C = d\pi$ is the circumference of the circle. Uhlmann et al. gives a correction to the equation including a term that corresponds to the average intermolecular distance, a_o .

$$\Delta G = d\pi\Delta\gamma_o \left(\frac{a_o}{a_o + d} \right)^2 \quad (D.1.2)$$

D.2 Derivation for the Clausius-Clapeyron Equation

The Clausius-Clapeyron Equation relates the variation of temperature needed when the change in pressure occurs in a system between two phases of a pure substance in equilibrium. The derivation for this expression is based on the Gibb's free energy. In a single phase, the change in Gibb's free energy can be defined by

$$dG = -SdT + VdP \quad (D.2.1)$$

where S is the entropy, T is temperature, V is volume, and P is pressure. For any pure substance that transforms from one phase to another, the change in Gibb's free energy is given by

$$dG = G_2 - G_1 \quad (\text{D.2.2})$$

Here G_1 and G_2 are molar free energies of the substance in initial and final states. During a phase change, the transformation from one phase to another will reach equilibrium which is when the molar free energies of the substance are the same in both phases, $dG = 0$, at a constant temperature and pressure. This implies that $G_1 = G_2$. Then at equilibrium,

$$-S_1dT + V_1dP = -S_2dT + V_2dP \quad (\text{D.2.3})$$

Rearranging this Eqn. (D.2.3) the expression becomes

$$\frac{dP}{dT} = \frac{S_2 - S_1}{V_2 - V_1} = \frac{dS}{dV} \quad (\text{D.2.4})$$

Another relation of the Gibb's free energy can also relate the latent heat by

$$dG = dH - TdS \quad (\text{D.2.5})$$

Again at Phase change $dG = 0$ which implies that $dS = \frac{dH}{T}$. Inserting this result

into Eqn. (D.2.4), gives

$$\frac{dP}{dT} = \frac{dH}{TdV} \quad (\text{D.2.6})$$

For the solid liquid phase change, the volume of the solid with respect to the liquid can be neglected, then it will be simplified as

$$\frac{dP}{dT} = \frac{dH}{TV_l} \quad (\text{D.2.7})$$

The expression is rearranged to get what we need in order to use in the velocity equation, then

$$\begin{aligned} \frac{dP}{dT} \frac{dy}{dy} &= \frac{h\rho_l}{TV_l} \\ \frac{dP}{dy} &= \frac{h\rho_l dT}{TV_l dy} \end{aligned} \quad (\text{D.2.8})$$

More information can be found in [67] . Refer to page 81 on handbook of phase change book.

D.3 Derivation for the Polarizability

The incident energy can be re-distributed depending on the particle size and the incident wave. If the particles are small compared to the wavelength of the incident wave, there is scattering almost equally into both the forward and backward direction. This type of scattering is found using Rayleigh scattering, theory which could explain the blue color of the sky.

If the particle size is comparable to the incident wavelength, then more energy is scattered in the forward direction and becomes very dependent on the refractive indices of the particle relative to the medium. Mie scattering is used to

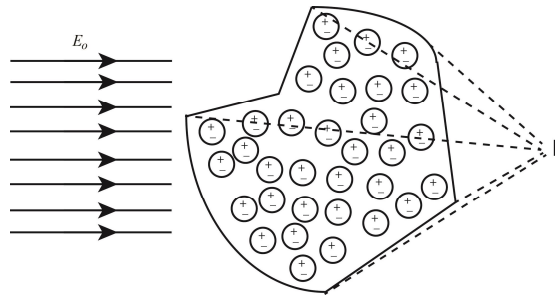


Figure D.3.1: The polarizability, P , is the combination of all the wavelets scattered by a region which is divided by many dipoles

calculate the absorption and scattering relations. This is based on solving Maxwell's equations for a spherical particle.

For Rayleigh scattering of a small homogeneous, isotropic spherical particle whose wavelength is much smaller than the incident wavelength, an applied field generates a dipole configuration dependent on the polarization. Consider an arbitrary particle similar to Fig. D.3.1. This particle is subdivided into small regions. An oscillating field of E_0 is applied to the particle inducing a dipole moment in each region causing the dipoles to oscillate at the frequency of the incident field and scatter in all directions. At P , a distance away from the particle, the total scattering fields are obtained by superimposing the scattered wavelets. The electric polarization, P , is defined as the average electric dipole moment per unit volume in the medium, or the vector sum of the dipole moments per unit volume. The constitutive relation for the dipole moment is $P = \epsilon_m \alpha E_0$, which indicates that the polarizability, α , is the measure of how easily the material can be polarized. This

value is dependent on the size, shape, composition, orientation, surrounding medium, number of particles, polarization state and, frequency of incident beam.

Consider a sphere, homogenous, isotropic particle with radius a that is placed in an arbitrary medium that is undergoing in a uniform electric field $E = E_0 e_z$, as shown in Fig. D.3.2.

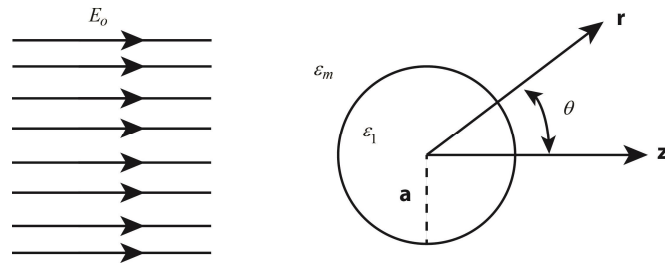


Figure D.3.2: A particle surrounded by an arbitrary medium undergoing a uniform electric field

The permittivity of the sphere and the outer medium are different. A charge is induced on the surface of a sphere. The equations describing the electric field inside and outside the sphere is described using the scalar potentials, ϕ_1 and ϕ_2 ,

$$E_1 = -\nabla \phi_1, E_2 = -\nabla \phi_2 \quad (\text{D.3.1})$$

where $\nabla \phi_1 = 0$ at $r < a$ and $\nabla \phi_2 = 0$ at $r > a$. The boundary conditions at $r = a$ are

$$\phi_1 = \phi_2, \quad \epsilon_1 \frac{\partial \phi_1}{\partial r} = \epsilon_2 \frac{\partial \phi_2}{\partial r} \quad (\text{D.3.2})$$

The solution for this problem is

$$\phi_1 = -\frac{3\varepsilon_m}{\varepsilon_1 + 2\varepsilon_m} E_0 r \cos \theta, \quad \phi_2 = -E_0 r \cos \theta + a^3 E_0 \frac{\varepsilon_1 - \varepsilon_m}{\varepsilon_1 + 2\varepsilon_m} \frac{\cos \theta}{r^2} \quad (\text{D.3.3})$$

The ideal dipole moment, P , is given as

$$P = 4\pi\varepsilon_m a^3 \frac{\varepsilon_1 - \varepsilon_m}{\varepsilon_1 + 2\varepsilon_m} E_0 \quad (\text{D.3.4})$$

As mentioned before, the constitutive relation for the dipole moment is $P = \varepsilon_m \alpha E_0$, which implies that the polarizability of a single particle in a medium can be defined by

$$\alpha = 4\pi a^3 \frac{\varepsilon_1 - \varepsilon_m}{\varepsilon_1 + 2\varepsilon_m} \quad (\text{D.3.5})$$

A similar process can be used for a coated particle surrounded by a couple of different layers with different permittivities, similar to that of Fig. D.3.3. Within this derivation, more equations and boundary conditions are needed to find the expression for the polarizability.

The absorption and scattering cross sections are defined as the amount of light absorbed or scattered per unit area in a given direction, respectively.

$$\begin{aligned} C_{abs} &= k \operatorname{Im}(\alpha) \\ C_{sca} &= \frac{k^4}{6\pi} |\alpha|^2 \end{aligned} \quad (\text{D.3.6})$$

where $k = 2\pi/\lambda$ is the wavenumber. More detailed information can be in [46]. The MATLAB code can be found in Appendix D.7.

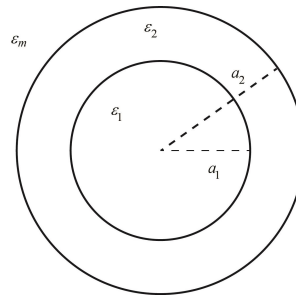


Figure D.3.3: A coated particle

D.4 Derivation for Drude's Model

In the early 1900s, Lorentz created a model that described the optical properties in which electrons and ions were treated as if it was a simple harmonic oscillator, or spring. The electron has a mass of m and charge of e , similar to Fig. D.4.1.

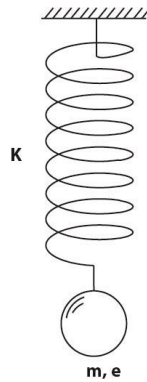


Figure D.4.1: Lorentz model using simple harmonic oscillators

The equation of motion of this oscillator is

$$m\ddot{x} + b\dot{x} + Kx = eE_{local} \quad (D.4.1)$$

In Eqn. (D.4.1), the restoring force is Kx such that K is the spring constant (or stiffness) and x is the displacement from equilibrium. The parameter $b\dot{x}$ is the damping force where b is the damping constant. The driving force is the local electric field, E_{local} . Take the electric field to be time harmonic with a frequency of ω . The solution to this problem consists of both a transient part which will die away because of the damping term, b , and an oscillatory term with the same frequency as E_{local} . The oscillatory part has a solution as

$$x = \frac{(e/m)E}{\omega_0^2 - \omega^2 - i\gamma\omega} \quad (D.4.2)$$

with $\gamma = b/m$ and $\omega_0^2 = K/m$. The induced dipole moment, p , of an oscillator is given by ex . If η represents the number of oscillators per unit volume, then the polarization, P , is given by $P = \eta p = \eta ex$. If the plasma frequency is given by $\omega_p^2 = \eta e^2 / m\epsilon_0$, then the polarization is

$$P = \frac{\omega_p^2}{\omega_0^2 - \omega^2 - i\gamma\omega} \epsilon_0 E \quad (D.4.3)$$

The constitutive relation for the polarization is $P = \epsilon_0 \chi E$, which is similar to Eqn.

(D.4.3), therefore, the dielectric for the simple harmonic oscillator is

$$\epsilon = 1 + \chi = 1 + \frac{\omega_p^2}{\omega_0^2 - \omega^2 - i\gamma\omega} \quad (D.4.4)$$

Equation (D.4.4) is Lorentz's model. Drude's model is a simplification of Eqn. (D.4.4), assuming that the value of the spring constant is zero, $K = 0$. This implies that Drude's dielectric function reduces to

$$\varepsilon = 1 - \frac{\omega_p^2}{\omega^2 + i\gamma\omega} \quad (\text{D.4.5})$$

D.5 Derivation for Level Set Method

The level set method was used to track the moving surfaces of the film and particle. This method was first proposed in 1988 by Osher and Sethian [69] which tracked the boundaries using a partial differential equation. Consider a boundary curve in two dimensions. The boundary moves with a velocity, v , which may be dependent on time and space. The level set function, d_B , is given by the advection equation

$$\frac{\partial d_B}{\partial t} + v \cdot \nabla d_B = 0 \quad (\text{D.5.1})$$

The velocity function can also be described using a force function, F , and a vector normal, n , as

$$v \cdot n = F \quad (\text{D.5.2})$$

with

$$n = \frac{\nabla d_B}{|\nabla d_B|} \quad (\text{D.5.3})$$

In this expression, when $d_B < 0$ implies inside the boundary, $d_B > 0$ represents data outside the boundary, and $d_B = 0$ represents the boundary curve. This continually changes with each time step.

Since this example is associated with a sphere of radius b . Then the equation with the moving boundary is

$$d_B = b^2 - x^2 - y^2 \quad (\text{D.5.4})$$

The normal gradient, n , is given by

$$\frac{\nabla d_B}{|\nabla d_B|} = \frac{-1}{2(x^2 + y^2)^{1/2}} \begin{bmatrix} 2x \\ 2y \end{bmatrix} \quad (\text{D.5.5})$$

Using Eqn. D.5.1 and a velocity, $v(v_1, v_2)$, then

$$\frac{\partial d_B}{\partial t} - \frac{2v_1x + 2v_2y}{2(x^2 + y^2)^{1/2}} = 0 \quad (\text{D.5.6})$$

In spherical coordinates with $x = b \cos \theta$, $y = b \sin \theta$, $v_1 = v_r \cos \theta$, $v_2 = v_\theta \sin \theta$

$$\frac{\partial d_B}{\partial t} - v_r - v_\theta = 0 \quad (\text{D.5.7})$$

Applying the non-dimensional terms $\tau = t \frac{4\hat{\alpha}}{d_p^2}$, $\hat{V}_r = \frac{2\hat{\alpha}v_r}{d_p}$, $\hat{V}_\theta = \frac{2\hat{\alpha}v_\theta}{d_p}$, $\phi = \frac{d_B}{d_p}$ our

expression becomes similar to that in Chapter 2

$$\frac{\partial \phi}{\partial \tau} = \frac{\hat{V}_r + \hat{V}_\theta}{2} \quad (\text{D.5.8})$$

D.6 Derivation of the angle between radial and tangential direction

When deriving the area specific mass flux, Eqn. (2.2.9) and/or Eqn. (B.1.6), the vector normal is used. However, my coordinates are in the radial and polar direction. If the particle/film were concentric circles, then the radial direction and normal direction would equal to one another. However, this is not the case. Within my calculations, the force of gravity is taken into account causing the film/particle to be non-concentric. To make the calculations complete, the angle, β , describing the shift between the normal and radial direction is derived in this section. Simple geometry was used to describe this shift.

For finding β , consider Fig. D.6.1. The inner circle represents the particle. The outer circle represents the film. To find the normal direction, consider that the radius is 'shifted' by x to be in the center of the outer circle (This is represented by the blue dashed line). The line x is calculated by considering the radius from the center of the particle to the top of the film, ϕ_{top} , and the radius of the center of the particle to the bottom of the film, ϕ_{bottom} ,

$$x = \frac{\phi_{top} - \phi_{bottom}}{2} \quad (D.6.1)$$

Notice ϕ_{top} is for when $\theta = -\pi/2$ and ϕ_{bottom} is for when $\theta = \pi/2$.

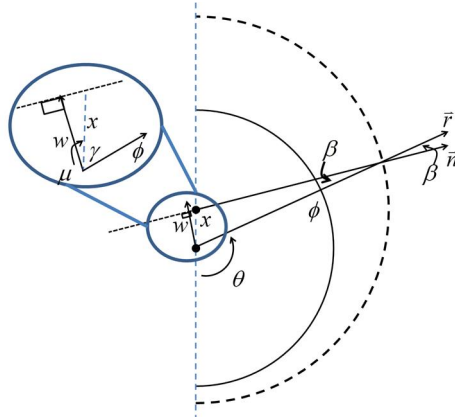


Figure D.6.1: Geometry for finding β when $\theta \geq 0$

Draw a line from the center of the particle to the radius of the normal so that the angle is perpendicular. Refer to Fig. D.6.1. This line is represented by w . Using Trig functions, β can be calculated by

$$\begin{aligned}\cos \mu &= \frac{w}{x} \\ \sin \beta &= \frac{w}{\phi} = \frac{x \cos \mu}{\phi}\end{aligned}\tag{D.6.2}$$

where μ is the angle between x and w . Finding μ is difficult and an approximation is considered. Based on this image the following statements are true,

$$\begin{aligned}\pi - \theta &= \gamma \\ \mu + \gamma &< \pi / 2 \\ \pi - \theta &< \pi / 2 - \mu \Rightarrow \mu < \theta - \pi / 2\end{aligned}\tag{D.6.3}$$

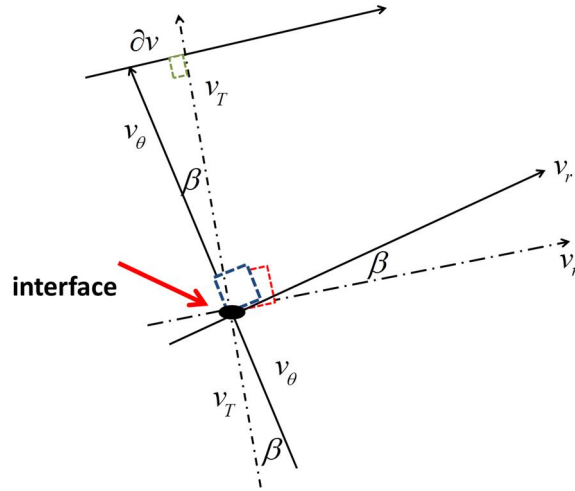


Figure D.6.3: Physical interpretation of the angle β

The value for β is very small, i.e. $\beta \approx 10^{-9}$ rads. This implies that my geometry is practically concentric for this application and the normal/radial direction are practically equal. This variable changes depending on $d\theta$ and ϕ and therefore β needs to be calculated for every iteration and for every $d\theta$.

D.7 Comments about Plasmonic Properties

Much of this work concentrates on the plasmonic properties. Plasmonic particles occur when an electron density couples with an electric field causing the electrons to oscillate. These oscillations are the consequences of the formation of a dipole in material when exposed to the photon. The light waves oscillate through the material creating a constant shift in the dipole. Because of this shift, the electrons deviate from its initial state and also vibrate. This arises at the same

frequency in which the particle is exposed to. The coupling of the electron and photon only occur when the frequency of the light is equal to or less than that of the plasma frequency and is greatest when it is equal to the plasma frequency.

Due to these oscillations, the absorption and scattering cross sections, which are described as the intensity that is absorbed and scattered for a particular frequency can be tuned dependent on the size, shape, dielectric material, and medium in which the material is in. This means that when changing the characteristics of the particle, the peak absorption cross section can shift throughout the visible and infrared range. In order to track the shift, the surface plasmon resonance (SPR) peak is compared. The SPR peak is defined as the wavelength in which the peak absorption occurs. The characteristic of altering tunability of the absorption and scattering is important for different applications like the hybrid nanofluid provided in Chapter 3 and biomedical applications [39]. Shapes in which researchers are fabricating include the nanosphere, nanoshell, nanorod, nanocage, nanobelt, etc. Schematics of the different particles are provided

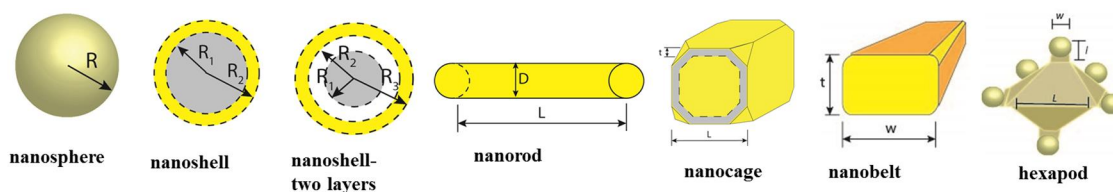


Figure D.7.1: Schematics of different nanoparticle shapes [39]

Table D.7.2: Optical properties of metal nanoparticles. Found in [39]

	Dimensions (nm)	λ_{\max} (nm)	Q_{abs}	Q_{ext}	Q_{sca}
Nanosphere					
Au [63,123,124]	$R=20$	521	0.9	0.9	0.0
	$R=40$	528	2.4	3.0	0.6
	$R=80$	549	4.0	6.0	2.0
Ag [125]	$R=76$	466	0.98	1.52	0.52
	$R=92$	486	1.61	2.1	0.39
Nanoshell					
Au Hollow [3,5]	$[R_1, R_2] = [20, 30]$	680	-	9.5	-
	$[R_1, R_2] = [30, 40]$	800	-	13	-
	$[R_1, R_2] = [40, 50]$	980	-	15	-
Si-Au [63,127,128]	$[R_1, R_2] = [60, 170]$	892	3.2	5.2	2.0
	$[R_1, R_2] = [90, 105]$	984	4.2	5.2	1.0
	$[R_1, R_2] = [120, 140]$	1120	3.5	4.1	0.6
(Fe ₃ O ₄ / γ - Fe ₂ O ₃)-Si-Au [129–131]	$[R_1, R_2, R_3] = [15, 155, 200]$	800	1.0	-	-
SPIO-Si-Au [129–131]	$[R_1, R_2] = [-, 90]$	720	0.55	-	-
Nanorod (capped cylinder)					
Au [63]	$[D, L] = [15, 30]$	797	13.5	14.5	1
	$[D, L] = [14.5, 3.3]$	863	15.5	17	1.5
	$[D, L] = [24, 46]$	815	13.5	18	4.5
Nanocage					
Au [132]	$[L, t] = [36.7, 3.3]$	800	11.9	13.5	1.6
Nanobelt					
Au [133]	$[w, t] = [100, 17]$	625	-	-	-
Nano-hexapod					
Au [134]	$[L, w, l] = [60, 13.2, 14.8]$	880	-	-	-
	$[L, w, l] = [33.4, -, 2]$	579	-	-	-

in Fig. D.7.1. From [39], Table D.7.2 is provided to show the SPR peak for various shapes, sizes, and materials. SPR peak is given by λ_{\max} .

There have been a couple of studies that are used to try and understand how the diffuse and collimated radiation is effected by adding nanoparticles with tunable absorption or scattering properties to the fluid. In 2008, Tjahjono and Bayazitoglu [37] observed the changes in the radiative transfer spectrum, local heat generation, and temperature distribution in a nanofluid medium when varying the concentration and configuration of the embedded nanoparticles. It was found that gold nanoshells particles tuned to have a great amount of scattering, increases the internal diffuse radiation resulting in a larger radiative distribution. When the particles are tuned to have a large amount of absorptance, the radiation intensity is high at the entry boundary and small near the exit boundary, resulting in a larger temperature gradient between the entry and exit sites. They propose that the proper concentration and nanoparticle configuration should be selected in order to get the desired magnitude of radiative decay. Another investigation by Vera and Bayazitoglu [48] conducted a one dimensional computational analysis of the radiative intensity profiles of tissues containing nanoparticles and exposed to radiation. He found that the diffuse radiation is more dominant than collimated radiation; however, the penetration depth expires within 1 mm. Increasing the concentration of the nanoparticles was shown to decrease the penetration depth and lower the radiative intensity for the diffuse component. The collimated radiation is not affected with the addition of nanoparticles. Both of these studies give insight to how the penetration depth is affected by adding tunable nanoparticles.

D.8 Code for Rayleigh Theory

This section gives the MATLAB program to describe Rayleigh scattering, *mie_scattering.m*. This code is for Au, Ag, Cu, Al, Graphite, and SiO₂/Au nanoshell. This function also calls another function called *properties.m* which essentially gives the absorption and index of refraction dependent on the wavelength and particle properties.

```
function [C_abs] = mie_scattering(dp0,epsilon_m,n_med,num)

% input dp0 - diameter of the particle

%   epsilon_m - permittivity of the medium --will vary dependent on whether it is a
%               gas or liquid

%   n_med - index of refraction for the medium

%   num - temp variable...tells us whether it is gold==1, silver==2, copper==3, or
%         alumunimum==4

% output C_abs - absorption cross section

%   C_sca - scattering cross section

e = 1.60217657e-19; % electron charge

m_e = 9.10938291e-31; % electron mass(kgs)

epsilon_0 = 8.854187817e-12; % permittivity of vacuum (Fm^-1)

lambda = 532e-9; % [m] wavelength

c = 3e8; % [m/s] speed of light

w = 2*pi*c./lambda; % [m/s] angular frequency

r = dp0/2; % [m] radius of sphere

k = 2*pi*n_med/lambda; % wavenumber
```

```

%%%%%%%%%%%%%%%%%%%%%%%%%%%%%%%%%%%%%%%%%%%%%%%%%%%%%%%%%%%%%%%%%%%%%%%%
% particle properties
%%%%%%%%%%%%%%%%%%%%%%%%%%%%%%%%%%%%%%%%%%%%%%%%%%%%%%%%%%%%%%%%%%%%%%%%

if num == 1

% parameters for gold particles

w_p = 2.183e15; %[n*e^2/(epsilon_0*m_e)]^(1/2); (s^-1) % plasma frequency
v_F = 1.4e6; %fermi velocity for gold (ms^-1)

ell = 3.8e-8; % electron mean free path for gold (m)

gamma = 6.46e12;%v_F/ell; %v_F/ell; for gold % relaxation constant or damping

string1 = ' Gold particle';

elseif num == 2

% parameters for silver particles

w_p = 1.327e15; %[n*e^2/(epsilon_0*m_e)]^(1/2); (s^-1) % plasma frequency
v_F = 1.39e6; %fermi velocity for silver (ms^-1)

ell = 5.2e-8; % electron mean free path for silver (m)

gamma = 4.343e12;%v_F/ell; %v_F/ell; for silver % relaxation constant or damping

string1 = ' Silver particle';

elseif num == 3

% parameters for copper particles

w_p = 1.6926e15; %[n*e^2/(epsilon_0*m_e)]^(1/2); (s^-1) % plasma frequency
v_F = 1.57e6; %fermi velocity for Cu (ms^-1)

ell = 3.9e-8; % electron mean free path for Cu (m)

gamma = v_F/ell; %for Cu % relaxation constant or damping term

string1 = ' Copper particle';

```

```

elseif num == 4

% parameters for aluminum particles

w_p = 2.829e15; %[n*e^2/(epsilon_0*m_e)]^(1/2); (s^-1) % plasma frequency v_F =
2.03e6; %fermi velocity for Al (ms^-1)

ell = 1.08e-8; % electron mean free path for Al (m)

gamma = 19.79e12;%v_F/ell; %for Al % relaxation constant or damping term

string1 = ' Aluminum particle';

elseif num == 6

w_p = 3.1753e15; % (s^-1) % plasma frequency

gamma = 3.388e15; %

%values found from Lidorikis

gamma_s=[2.4004e15, 3.9349e15, 2.4308e15, 1.5345e15, 3.2968e15, 1.5102e16,
1.2762e16];

omega_s= [1.1243e15, 6.6159e15, 6.7759e15, 2.1908e16, 2.1452e16, 2.4855e16,
3.2588e16];

sigma_s=[6.5632e15, 7.8850e15, 1.2534e16, 5.4846e15, 2.2227e16, 2.2743e16,
9.1916e15];

string1 = 'Graphite particle';

end % end if statement for particle properties

%%%%%%%%%%%%%%%%%%%%%%%%%%%%%%%%%%%%%%%%%%%%%%%%%%%%%%%%%%%%%%%%%%%%%%%%%%%%%%
%%%%%%%%%%%%%%%%%%%%%%%%%%%%%%%%%%%%%%%%%%%%%%%%%%%%%%%%%%%%%%%%%%%%%%%%%%%%%%

% finding the bulk dielectric function from Johnson and Christy "Optical constants of the
nobel metals"

% the values are given in eV

```

```

% h = 4.13566733e-15; %eVs

% interpolation for the specific wavelenths i wanted. recall that E = h nu

% = hc/lambda

% using the function i made to find the bulk properties from Johnson and
% Christy's paper for gold silver and copper--- and Rakic 1995 for aluminum
if num ~= 6

    % using the function i made to find the bulk properties from Johnson and
    % Christy's paper for gold silver and copper--- and Rakic 1995 for aluminum

    [n,kappa] = properties(lambda,num);

    e_bulk = n^2 - kappa^2 + 1i*2*n*kappa;

    % drude's model

    epsilon = e_bulk - w_p^2./(w.^2+1i*gamma.*w); % dielectric function for sphere epsilon =
    epsilon_1+iepsilon_2

else

    % drude lorentz model for graphite

    summation = 0;

    for kk = 1:7

        bottom = [omega_s(kk)^2 - w^2 - 1i*w.*gamma_s(kk)];

        summation = summation + sigma_s(kk)^2/bottom;

    end

    epsilon = 1 - w_p^2./(w.^2+1i*gamma.*w) + summation; % dielectric function for sphere

    epsilon = epsilon_1+iepsilon_2

end % end if statement

epsilon_r = epsilon/epsilon_m;

```

```

V = (4/3)*pi*r^3; % [m] volume of the particle

alpha = (3*r^3)/(4*pi)*(epsilon_r-1)/(epsilon_r+2); % polarizability

C_abs = (k)*imag(alpha); %[m^2] absorption cross section

C_sca = (k^4/(6*pi))*abs(alpha)^2; % [m^2] scattering cross section\

Q_abs = C_abs/(pi*(dp0/2)^2)

end

function [n,kappa] = properties(lambda,num)

% This essentially does a linear interpolation of the properties if necessary

if num == 5

num=1;

end

% input -- lambda or the wavelength and num == 1 means gold, num == 2 means silver, num

== 3 means copper

% output -- kappa and n

% the values are given in eV

% recall that  $E = h \nu = hc/\lambda$ 

c = 3e8; % speed of light [m/s]

h = 4.13566733e-15; % [eVs]

if num == 1 % gold

% finding the bulk dielectric function from Johnson and Christy "Optical constants of the

%nobel metals"

eV=[15,11.5,7.5,6.60,6.47,6.35,6.22,6.10,5.98,5.85,5.73,5.60,5.48,5.36,5.23,5.11,4.98,4.86,4.

```



```

74,4.61,4.49,4.36,4.24,4.12,3.99,3.87,3.74,3.62,3.50,3.37,3.25,3.12,3.00,2.88,2.75,2.63,2.50,2
.38,2.26,2.13,2.01,1.88,1.76,1.64,1.51,1.39,1.26,1.14,1.02,0.89,0.77,0.64,0.5,0.1,0.05,0.01];

lambda_sample = [(h*c)./eV];    %wavelength [m]

n_sample=[1.54, 1.569, 1.786, 1.28, 1.32, 1.34, 1.33, 1.33, 1.30, 1.30, 1.30, 1.30, 1.31, 1.30,
1.32, 1.32, 1.33, 1.33, 1.35, 1.38, 1.43, 1.47, 1.49, 1.53, 1.53, 1.54, 1.48, 1.48, 1.50, 1.48, 1.46,
1.47, 1.46, 1.45, 1.38, 1.31, 1.04, 0.62, 0.43, 0.29, 0.21, 0.14, 0.13, 0.14, 0.16, 0.17, 0.22, 0.27,
0.35, 0.43, 0.56, 0.92, 1.273, 26.9, 65.5, 222];

kappa_sample=[0.934, 0.92, 1.15, 1.188, 1.203, 1.226, 1.251, 1.277, 1.304, 1.350, 1.387,
1.427, 1.460, 1.497, 1.536, 1.577, 1.631, 1.688, 1.749, 1.803, 1.847, 1.869, 1.878, 1.889,
1.893, 1.898, 1.883, 1.871, 1.866, 1.895, 1.933, 1.952, 1.958, 1.948, 1.914, 1.849, 1.833,
2.081, 2.455, 2.863, 3.272, 3.697, 4.103, 4.542, 5.083, 5.663, 6.350, 7.150, 8.145, 9.519,
11.21, 13.78, 18.1, 80.7, 124, 256];

elseif num == 2 % silver

% finding the bulk dielectric function from Johnson and Christy "Optical constants of the
nobel metals"

eV=[14,12,9,7,6.60,6.47,6.35,6.22,6.10,5.98,5.85,5.73,5.60,5.48,5.36,5.23,5.11,4.98,4.86,4.74
,4.61,4.49,4.36,4.24,4.12,3.99,3.87,3.74,3.62,3.50,3.37,3.25,3.12,3.00,2.88,2.75,2.63,2.50,2.3
8,2.26,2.13,2.01,1.88,1.76,1.64,1.51,1.39,1.26,1.14,1.02,0.89,0.77,0.64,0.6,0.55,0.5,0.45,0.4,0.
35,0.3,0.25,0.2,0.15,0.1];

lambda_sample = [(h*c)./eV];    %wavelength [m]

n_sample=[1.72, 1.608, 1.326, 1.178, 1.07, 1.10, 1.12, 1.14, 1.15, 1.18, 1.20, 1.22, 1.25, 1.26,
1.28, 1.28, 1.30, 1.31, 1.33, 1.35, 1.38, 1.41, 1.41, 1.39, 1.34, 1.13, 0.81, 0.17, 0.14, 0.10, 0.07,
0.05, 0.05, 0.05, 0.04, 0.04, 0.05, 0.05, 0.05, 0.06, 0.05, 0.06, 0.05, 0.04, 0.03, 0.04, 0.04, 0.04,

```

```
0.04, 0.09, 0.13, 0.15, 0.24, 0.674, 0.749, 0.865, 1.078, 1.3, 1.697, 2.222, 3.154, 5.037, 8.326,
17.544];
```

```
kappa_sample= [0.783, 0.587, 0.562, 1.06, 1.212, 1.232, 1.255, 1.277, 1.296, 1.312, 1.325,
1.336, 1.342, 1.344, 1.357, 1.367, 1.378, 1.389, 1.393, 1.387, 1.372, 1.331, 1.264, 1.161,
0.964, 0.616, 0.392, 0.829, 1.142, 1.419, 1.657, 1.864, 2.070, 2.275, 2.462, 2.657, 2.869,
3.093, 3.324, 3.586, 3.858, 4.152, 4.483, 4.838, 5.242, 5.727, 6.312, 6.992, 7.795, 8.828,
10.10, 11.85, 13.08, 13.77, 14.65, 15.92, 18.01, 19.96, 23.03, 26.55, 31.84, 40.43, 52.07,
75.33];
```

```
elseif num == 3 % copper
```

```
% finding the bulk dielectric function from Johnson and Christy "Optical constants of the
nobel metals"
```

```
eV=[14, 12, 11, 10, 8.5, 6.60, 6.47, 6.35, 6.22, 6.10, 5.98, 5.85, 5.73, 5.60, 5.48, 5.36, 5.23,
5.11, 4.98, 4.86, 4.74, 4.61, 4.49, 4.36, 4.24, 4.12, 3.99, 3.87, 3.74, 3.62, 3.50, 3.37, 3.25, 3.12,
3.00, 2.88, 2.75, 2.63, 2.50, 2.38, 2.26, 2.13, 2.01, 1.88, 1.76, 1.64, 1.51, 1.39, 1.26, 1.14, 1.02,
0.89, 0.77, 0.64, 0.5, 0.1, 0.05, 0.01, 0.005];
```

```
lambda_sample = [(h*c)./eV]; %wavelength [m]
```

```
n_sample=[1.055, 0.091, 1.074, 1.038, 1.029, 0.94, 0.95, 0.97, 0.98, 0.99, 1.01, 1.04, 1.08,
1.13, 1.18, 1.23, 1.28, 1.34, 1.37, 1.41, 1.41, 1.45, 1.46, 1.45, 1.42, 1.40, 1.38, 1.38, 1.34, 1.36,
1.37, 1.36, 1.33, 1.32, 1.28, 1.25, 1.24, 1.25, 1.22, 1.18, 1.02, 0.70, 0.30, 0.22, 0.21, 0.24, 0.26,
0.30, 0.32, 0.36, 0.48, 0.60, 0.76, 1.09, 1.692, 29.1, 62.8, 186, 270];
```

```
kappa_sample=[0.724, 0.713, 0.754, 0.818, 0.979, 1.337, 1.338, 1.440, 1.493, 1.550, 1.599,
1.651, 1.699, 1.737, 1.768, 1.792, 1.802, 1.799, 1.783, 1.741, 1.691, 1.668, 1.646, 1.633,
1.633, 1.679, 1.729, 1.783, 1.821, 1.864, 1.916, 1.975, 2.045, 2.116, 2.207, 2.305, 2.397,
```

```
2.483, 2.564, 2.608, 2.577, 2.704, 3.205, 3.747, 4.205, 4.665, 5.180, 5.768, 6.421, 7.217,
8.245, 9.439, 11.12, 13.43, 17.6, 71.1, 103, 213, 294];
```

```
elseif num == 4 % aluminum
```

```
% these values are found using Rakic 1995 "Algorithm for the determination of intrinsic
optical constants of metal films: application to aluminum"
```

```
eV=[15.5,13,11,9,0,8,0,7,0,6,0,5,0,4,0,3,8,3,4,3,0,2,8,2,6,2,4,2,2,2,0,1,9,1,8,1,7,1,6,1,5,6,1,5,2,1,
48,1,40,1,36,1,32,1,28,1,24,1,2,1,10,1,0,0,9,0,8,0,7,0,6,0,5,0,4,0,3,8,0,3,6,0,3,4,0,3,2,0,3,0,2
8,0,26,0,24,0,22,0,2,0,18,0,16,0,14,0,12,0,1,0,0,5,0,0,1,0,0,0,5];
```

```
lambda_sample = [(h*c)./eV]; %wavelength [m]
```

```
n_sample=[0.252, 0.065, 0.061, .057167, .072505, .094236, .12677, .18137, .28003, .31474,
.39877, .52135, .6079, .7278, .8734, 1.0728, 1.366, 1.5724, 1.8301, 2.1606, 2.6154, 2.7675,
2.7668, 2.6945, 2.2802, 1.9739, 1.6784, 1.4967, 1.4359, 1.3998, 1.3281, 1.3157, 1.3899,
1.5782, 1.9205, 2.4738, 3.3372, 3.938, 4.7097, 5.0735, 5.4903, 5.9564, 6.4808, 7.0796,
7.7757, 8.5881, 9.5580, 10.742, 12.195, 14.088, 16.755, 20.837, 26.216, 33.519, 95.7, 323,
484];
```

```
kappa_sample=[0.0997 ,0.593 ,0.946, 1.3775, 1.6366, 1.9519, 2.3563, 2.9029, 3.7081,
3.9165, 4.3954, 5.0008, 5.3676, 5.7781, 6.2418, 6.7839, 7.4052, 7.7354, 8.0601, 8.3565,
8.4914, 8.3866, 8.2573, 8.1878, 8.1134, 8.3058, 8.5970, 9.0655, 9.4939, 9.8914, 10.969,
12.245, 13.784, 15.6556, 17.991, 20.982, 25.004, 27.580, 30.737, 32.183, 33.814, 35.608,
37.595, 39.826, 42.367, 45.257, 48.593, 52.518, 57.156, 62.841, 69.857, 78.274, 88.197,
101.28, 185, 383, 528];
```

```
end
```

```
% start doing linear interpolation
```

```
difference = lambda_sample-lambda*ones(1,length(eV));
```

```

if length(find(difference==0))~= 0

    A = find(difference==0);
    kappa = kappa_sample(A);
    n = n_sample(A);

else

    A = find(difference>0);
    one = A(1); % A is a temp variable. I am getting the first positive place
    B = find(difference<0);
    two = B(end); % B is a temp variable. I am getting the last negative place
    kappa=([kappa_sample(one)-kappa_sample(two)]/[lambda_sample(one)-
    lambda_sample(two)])*(lambda - lambda_sample(one)) + kappa_sample(one);
    n=([n_sample(one)-n_sample(two)]/[lambda_sample(one)-lambda_sample(two)])*(lambda
    - lambda_sample(one)) + n_sample(one);
end % end if statement

end

```

References

- [1] Tullius T. K., and Bayazitoglu Y., 2015, "Temperature of a metallic nanoparticle embedded in a phase change media exposed to radiation," *Int. J. Heat Mass Transf.*, **Submitted**.
- [2] Tullius T. K., and Bayazitoglu Y., 2015, "Analysis of a hybrid nanofluid exposed to radiation," *Numer. Heat Transf. Part B*, **Submitted**.
- [3] Cabeza L. F., Sole C., Castell A., Oro E., and Gil A., 2012, "Review of solar thermal storage techniques and associated heat transfer technologies," *Proc. IEEE*, **100**(2), pp. 525–538.
- [4] Liu M., Saman W., and Bruno F., 2012, "Review on storage materials and thermal performance enhancement techniques for high temperature phase change thermal storage systems," *Renew. Sustain. Energy Rev.*, **16**(4), pp. 2118–2132.
- [5] Zhou D., Zhao C. Y., and Tian Y., 2012, "Review on thermal energy storage with phase change materials (PCMs) in building applications," *Appl. Energy*, **92**, pp. 593–605.
- [6] Mehling H., and Cabeza L. F., 2008, *Heat and cold storage with PCM: An up to date introduction into basics and applications*, Springer.
- [7] Olabi A. G., Fernandes D., Pitié F., Cáceres G., and Baeyens J., 2012, "Thermal energy storage: 'How previous findings determine current research priorities,'" *Energy*, **39**(1), pp. 246–257.
- [8] Khodadadi J. M., Fan L., and Babaei H., 2013, "Thermal conductivity enhancement of nanostructure-based colloidal suspensions utilized as phase change materials for thermal energy storage: A review," *Renew. Sustain. Energy Rev.*, **24**, pp. 418–444.
- [9] Costner E. A., Long B. K., Navar C., Jockusch S., Lei X., Zimmerman P., Campion A., Turro N. J., and Willson C. G., 2009, "Fundamental optical properties of linear and cyclic alkanes: VUV absorbance and index of refraction," *J. Phys. Chem. A*, **113**(33), pp. 9337–47.
- [10] Fermeglia M., and Torriano G., 1999, "Density, viscosity, and refractive index for binary systems of n -C16 and four nonlinear Alkanes at 298.15 K," *J. Chem. Eng. Data*, **44**(5), pp. 965–969.

- [11] Sharma S. D., Kitano H., and Sagara K., 2004, "Phase change materials for low temperature solar thermal applications," *Res. Rep. Fac. Eng. Mie Univ.*, **29**, pp. 31–64.
- [12] Khodadadi J. M., and Hosseinzadeh S. F., 2007, "Nanoparticle-enhanced phase change materials (NEPCM) with great potential for improved thermal energy storage," *Int. Commun. Heat Mass Transf.*, **34**(5), pp. 534–543.
- [13] Fan L., and Khodadadi J. M., 2012, "An experimental investigation of enhanced thermal conductivity and expedited unidirectional freezing of cyclohexane-based nanoparticle suspensions utilized as nano-enhanced phase change materials (NePCM)," *Int. J. Therm. Sci.*, **62**, pp. 120–126.
- [14] Fan L., and Khodadadi J. M., 2011, "Temperature dependent thermal conductivity of eicosane based phase change materials with copper oxide nanoparticles," *Proceedings of the International Symposium on Thermal and Materials Nanoscience and Nanotechnology*, Antalya, Turkey.
- [15] Nabil M., and Khodadadi J. M., 2013, "Experimental determination of temperature-dependent thermal conductivity of solid eicosane-based nanostructure-enhanced phase change materials," *Int. J. Heat Mass Transf.*, **67**, pp. 301–310.
- [16] El Hasadi Y. M. F., and Khodadadi J. M., 2013, "Numerical simulation of the effect of the size of suspensions on the solidification process of nanoparticle-enhanced phase change materials," *J. Heat Transfer*, **135**(5), p. 052901.
- [17] Dhaidan N. S., Khodadadi J. M., Al-Hattab T. A., and Al-Mashat S. M., 2013, "Experimental and numerical investigation of melting of phase change material/nanoparticle suspensions in a square container subjected to a constant heat flux," *Int. J. Heat Mass Transf.*, **66**, pp. 672–683.
- [18] Rao Z., Wang S., and Peng F., 2013, "Molecular dynamics simulations of nano-encapsulated and nanoparticle-enhanced thermal energy storage phase change materials," *Int. J. Heat Mass Transf.*, **66**, pp. 575–584.
- [19] Cingarapu S., Singh D., Timofeeva E. V., and Moravek M. R., 2014, "Nanofluids with encapsulated tin nanoparticles for advanced heat transfer and thermal energy storage," *Int. J. Energy Res.*, **38**(1), pp. 51–59.
- [20] Chieruzzi M., Cerritelli G. F., Miliozzi A., and Kenny J. M., 2013, "Effect of nanoparticles on heat capacity of nanofluids based on molten salts as PCM for thermal energy storage," *Nanoscale Res. Lett.*, **8**(1), p. 448.

- [21] Jegadheeswaran S., Pohekar S. D., and Kousksou T., 2012, "Investigations on thermal storage systems containing micron-sized conducting particles dispersed in a phase change material," *Mater. Renew. Sustain. Energy*, **1**(1), p. 5.
- [22] Ho C. J., and Gao J. Y., 2009, "Preparation and thermophysical properties of nanoparticle-in-paraffin emulsion as phase change material," *Int. Commun. Heat Mass Transf.*, **36**(5), pp. 467–470.
- [23] Wu S. Y., Wang H., Xiao S., and Zhu D. S., 2011, "An investigation of melting/freezing characteristics of nanoparticle-enhanced phase change materials," *J. Therm. Anal. Calorim.*, **110**(3), pp. 1127–1131.
- [24] Wu S., Zhu D., Zhang X., and Huang J., 2010, "Preparation and melting/freezing characteristics of Cu/paraffin nanofluid as phase-change material (PCM)," *Energy & Fuels*, **24**(3), pp. 1894–1898.
- [25] Zeng J. L., Sun L. X., Xu F., Tan Z. C., Zhang Z. H., Zhang J., and Zhang T., 2006, "Study of a PCM based energy storage system containing Ag nanoparticles," *J. Therm. Anal. Calorim.*, **87**(2), pp. 371–375.
- [26] Zeng J. L., Cao Z., Yang D. W., Sun L. X., and Zhang L., 2009, "Thermal conductivity enhancement of Ag nanowires on an organic phase change material," *J. Therm. Anal. Calorim.*, **101**(1), pp. 385–389.
- [27] Zeng J. L., Cao Z., Yang D. W., Xu F., Sun L. X., Zhang X. F., and Zhang L., 2009, "Effects of MWNTs on phase change enthalpy and thermal conductivity of a solid-liquid organic PCM," *J. Therm. Anal. Calorim.*, **95**(2), pp. 507–512.
- [28] Assis E., Katsman L., Ziskind G., and Letan R., 2007, "Numerical and experimental study of melting in a spherical shell," *Int. J. Heat Mass Transf.*, **50**(9-10), pp. 1790–1804.
- [29] Eames I. W., and Adref K. T., 2002, "Freezing and melting of water in spherical enclosures of the type used in thermal (ice) storage systems," *Appl. Therm. Eng.*, **22**(7), pp. 733–745.
- [30] Hu Y., and Shi M., 1998, "Close-contact melting in a spherical enclosure," *Sci. China Ser. E Technol. Sci.*, **41**(1), pp. 82–87.
- [31] Assis E., Ziskind G., and Letan R., 2009, "Numerical and experimental study of solidification in a spherical shell," *J. Heat Transfer*, **131**(2), p. 024502.

- [32] Uhlmann D. R., Chalmers B., and Jackson K. A., 1964, "Interaction between particles and a solid-liquid interface," *J. Appl. Phys.*, **35**(10), p. 2986.
- [33] Shangguan D., Ahuja S., and Stefanescu D. M., 1992, "An analytical model for the interaction between an insoluble particle and an advancing solid/liquid interface," *Metall. Trans. A*, **23**(2), pp. 669–680.
- [34] Garvin J. ., and Udaykumar H. ., 2003, "Particle–solidification front dynamics using a fully coupled approach, Part I: methodology," *J. Cryst. Growth*, **252**(1), pp. 451–466.
- [35] Bulanti B., and Arslanturk C., 2006, "Analysis of inward melting of spheres subject to convection and radiation," *J. Therm. Sci. Techonology*, **26**(2), pp. 11–16.
- [36] Jain P. K., Lee K. S., El-Sayed I. H., and El-Sayed M. A., 2006, "Calculated absorption and scattering properties of gold nanoparticles of different size, shape, and composition: applications in biological imaging and biomedicine.," *J. Phys. Chem. B*, **110**(14), pp. 7238–7248.
- [37] Tjahjono I. K., and Bayazitoglu Y., 2008, "Near-infrared light heating of a slab by embedded nanoparticles," *Int. J. Heat Mass Transf.*, **51**(7-8), pp. 1505–1515.
- [38] Halas N. J., 2010, "Plasmonics: an emerging field fostered by Nano Letters.," *Nano Lett.*, **10**(10), pp. 3816–3822.
- [39] Bayazitoglu Y., Kheradmand S., and Tullius T. K., 2013, "An overview of nanoparticle assisted laser therapy," *Int. J. Heat Mass Transf.*, **67**, pp. 469–486.
- [40] Bayazitoglu Y., Kheradmand S., and Tullius T. K., 2013, "Thermal therapy with metal nanoparticle assisted laser heating," 7th International Symposium of Radiative Transfer, Kusadasi, Turkey, p. RAD–13–D1.
- [41] Qin Z., and Bischof J. C., 2012, "Thermophysical and biological responses of gold nanoparticle laser heating.," *Chem. Soc. Rev.*, **41**(3), pp. 1191–1217.
- [42] Young J. K., Figueroa E. R., and Drezek R. A., 2012, "Tunable nanostructures as photothermal theranostic agents.," *Ann. Biomed. Eng.*, **40**(2), pp. 438–459.
- [43] Bayazitoglu Y., 2014, "Volumetric laser or solar heating with plasmonic nanoparticle," The 15th International Heat Transfer Conference, Kyoto, Japan, pp. IHTC–15, IHTC15–KN20.

- [44] Pastoriza-Santos I., Gomez D., Perez-Juste J., Liz-Marzan L. M., and Mulvaney P., 2004, "Optical properties of metal nanoparticle coated silica spheres: a simple effective medium approach," *Phys. Chem. Chem. Phys.*, **6**(21), p. 5056.
- [45] Miller M. M., and Lazarides A. A., 2005, "Sensitivity of metal nanoparticle surface plasmon resonance to the dielectric environment," *J. Phys. Chem. B*, **109**(46), pp. 21556–21565.
- [46] Bohren C. F., and Huffman D. R., 1983, *Absorption and Scattering of Light by Small Particles*, Wiley, New York.
- [47] Vera J., and Bayazitoglu Y., 2009, "Gold nanoshell density variation with laser power for induced hyperthermia," *Int. J. Heat Mass Transf.*, **52**(3-4), pp. 564–573.
- [48] Vera J., and Bayazitoglu Y., 2009, "A note on laser penetration in nanoshell deposited tissue," *Int. J. Heat Mass Transf.*, **52**(13-14), pp. 3402–3406.
- [49] Xu X., Meade A., and Bayazitoglu Y., 2011, "Numerical investigation of nanoparticle-assisted laser-induced interstitial thermotherapy toward tumor and cancer treatments," *Lasers Med. Sci.*, **26**(2), pp. 213–222.
- [50] Shah M., Badwaik V. D., and Dakshinamurthy R., 2014, "Biological applications of gold nanoparticles," *J. Nanosci. Nanotechnol.*, **14**(1), pp. 344–362.
- [51] Xu X., Meade A., and Bayazitoglu Y., 2012, "Feasibility of selective nanoparticle-assisted photothermal treatment for an embedded liver tumor," *Lasers Med. Sci.*
- [52] Xu X., Meade A., and Bayazitoglu Y., 2010, "Fluence rate distribution in laser-induced interstitial thermotherapy by mesh free collocation," *Int. J. Heat Mass Transf.*, **53**(19-20), pp. 4017–4022.
- [53] Gobin A. M., Lee M. H., Halas N. J., James W. D., Drezek R. A., and West J. L., 2007, "Near-infrared resonant nanoshells for combined optical imaging and photothermal cancer therapy," *Nano Lett.*, **7**(7), pp. 1929–1934.
- [54] Huang X., and El-Sayed M. A., 2010, "Gold nanoparticles: Optical properties and implementations in cancer diagnosis and photothermal therapy," *J. Adv. Res.*, **1**(1), pp. 13–28.
- [55] Neumann O., Urban A. S., Day J., Lal S., Nordlander P., and Halas N. J., 2013, "Solar vapor generation enabled by nanoparticles," *ACS Nano*, **7**(1), pp. 42–49.

- [56] Fang Z., Zhen Y.-R., Neumann O., Polman A., García de Abajo F. J., Nordlander P., and Halas N. J., 2013, "Evolution of light-induced vapor generation at a liquid-immersed metallic nanoparticle.," *Nano Lett.*, **13**(4), pp. 1736–1742.
- [57] Neumann O., Feronti C., Neumann A. D., Dong A., Schell K., Lu B., Kim E., Quinn M., Thompson S., Grady N., Nordlander P., Oden M., and Halas N. J., 2013, "Compact solar autoclave based on steam generation using broadband light-harvesting nanoparticles.," *Proc. Natl. Acad. Sci. U. S. A.*, **110**(29), pp. 11677–11681.
- [58] Dietzel M., and Poulikakos D., 2007, "On vapor bubble formation around heated nanoparticles in liquids," *Int. J. Heat Mass Transf.*, **50**(11), pp. 2246–2259.
- [59] Honda H., Makishi O., and Yamashiro H., 2007, "Generalized stability theory of vapor film in subcooled film boiling on a sphere," *Int. J. Heat Mass Transf.*, **50**(17), pp. 3390–3400.
- [60] Johnson P. B., and Christy R. W., 1972, "Optical constants of the noble metals," *Phys. Rev. B*, **6**(12), pp. 4370–4379.
- [61] Loo C., Lin A., Hirsch L., Lee M.-H., Barton J., Halas N., West J., and Drezek R., 2004, "Nanoshell-enabled photonics-based imaging and therapy of cancer.," *Technol. Cancer Res. Treat.*, **3**(1), pp. 33–40.
- [62] Draine B. T., and Flatau P. J., 1994, "Discrete-dipole approximation for scattering calculations," *J. Opt. Soc. Am. A*, **11**(4), p. 1491.
- [63] Jain P. K., Lee K. S., El-Sayed I. H., and El-Sayed M. A., 2006, "Calculated absorption and scattering properties of gold nanoparticles of different size, shape, and composition: applications in biological imaging and biomedicine," *J. Phys. Chem. B*, **110**(14), pp. 7238–7248.
- [64] Vera J., and Bayazitoglu Y., 2015, "Temperature and heat flux dependence of thermal resistance of water/metal nanoparticle interfaces at sub-boiling temperatures," *Int. J. Heat Mass Transf.*, **86**, pp. 433–442.
- [65] Hillig W. B., 1998, "Measurement of interfacial free energy for ice/water system," *J. Cryst. Growth*, **183**(3), pp. 463–468.
- [66] Mandelkern L., 2004, *Crystallization of polymers*, Volume 2, Cambridge University Press.

- [67] Roy B. N., 2002, *Fundamentals of Classical and Statistical Thermodynamics*, John Wiley and Sons; 1 edition.
- [68] Kotaidis V., Dahmen C., von Plessen G., Springer F., and Plech a, 2006, "Excitation of nanoscale vapor bubbles at the surface of gold nanoparticles in water," *J. Chem. Phys.*, **124**(18), p. 184702.
- [69] Osher S., and Sethian J. A., 1988, "Fronts propagating with curvature-dependent speed: Algorithms based on Hamilton-Jacobi formulations," *J. Comput. Phys.*, **79**(1), pp. 12–49.
- [70] Sethian J. A., and Smereka P., 2003, "Level set methods for fluid interfaces," *Annu. Rev. Fluid Mech.*, **35**(1), pp. 341–372.
- [71] Thomas J. W., 1995, *Numerical Partial Differential Equations: Finite Difference Methods*, Volume 1, Springer Science & Business Media.
- [72] Choi S. U. S., and Eastman J. A., 1995, "Enhancing thermal conductivity of fluids with nanoparticles," 1995 International mechanical engineering congress and exhibition, San Francisco, CA (United States),.
- [73] Khanafer K., and Vafai K., 2011, "A critical synthesis of thermophysical characteristics of nanofluids," *Int. J. Heat Mass Transf.*, **54**(19-20), pp. 4410–4428.
- [74] Saidur R., Leong K. Y., and Mohammad H. A., 2011, "A review on applications and challenges of nanofluids," *Renew. Sustain. Energy Rev.*, **15**(3), pp. 1646–1668.
- [75] Lomascolo M., Colangelo G., Milanese M., and de Risi A., 2015, "Review of heat transfer in nanofluids: conductive, convective and radiative experimental results," *Renew. Sustain. Energy Rev.*, **43**, pp. 1182–1198.
- [76] Kasaeian A., Eshghi A. T., and Sameti M., 2015, "A review on the applications of nanofluids in solar energy systems," *Renew. Sustain. Energy Rev.*, **43**, pp. 584–598.
- [77] Tyagi H., Phelan P., and Prasher R., 2009, "Predicted efficiency of a low-temperature nanofluid-based direct absorption solar collector," *J. Sol. Energy Eng.*, **131**(4), p. 041004.
- [78] Otanicar T. P., Phelan P. E., Prasher R. S., Rosengarten G., and Taylor R. A., 2010, "Nanofluid-based direct absorption solar collector," *J. Renew. Sustain. Energy*, **2**(3), p. 033102.

- [79] Taylor R. A., Phelan P. E., Otanicar T. P., Adrian R., and Prasher R., 2011, "Nanofluid optical property characterization: towards efficient direct absorption solar collectors,," *Nanoscale Res. Lett.*, **6**(1), p. 225.
- [80] Taylor R. A., Phelan P. E., Adrian R. J., Gunawan A., and Otanicar T. P., 2012, "Characterization of light-induced, volumetric steam generation in nanofluids," *Int. J. Therm. Sci.*, **56**, pp. 1–11.
- [81] Lenert A., and Wang E. N., 2012, "Optimization of nanofluid volumetric receivers for solar thermal energy conversion," *Sol. Energy*, **86**(1), pp. 253–265.
- [82] Saidur R., Meng T. C., Said Z., Hasanuzzaman M., and Kamyar A., 2012, "Evaluation of the effect of nanofluid-based absorbers on direct solar collector," *Int. J. Heat Mass Transf.*, **55**(21-22), pp. 5899–5907.
- [83] Yousefi T., Veysi F., Shojaeizadeh E., and Zinadini S., 2012, "An experimental investigation on the effect of Al₂O₃-H₂O nanofluid on the efficiency of flat-plate solar collectors," *Renew. Energy*, **39**(1), pp. 293–298.
- [84] Yousefi T., Veisy F., Shojaeizadeh E., and Zinadini S., 2012, "An experimental investigation on the effect of MWCNT-H₂O nanofluid on the efficiency of flat-plate solar collectors," *Exp. Therm. Fluid Sci.*, **39**, pp. 207–212.
- [85] Lee S. W., Kim K. M., and Bang I. C., 2013, "Study on flow boiling critical heat flux enhancement of graphene oxide/water nanofluid," *Int. J. Heat Mass Transf.*, **65**, pp. 348–356.
- [86] Zhang L., Fan L., Yu Z., and Cen K., 2014, "An experimental investigation of transient pool boiling of aqueous nanofluids with graphene oxide nanosheets as characterized by the quenching method," *Int. J. Heat Mass Transf.*, **73**, pp. 410–414.
- [87] Sani E., Mercatelli L., Barison S., Pagura C., Agresti F., Colla L., and Sansoni P., 2011, "Potential of carbon nanohorn-based suspensions for solar thermal collectors," *Sol. Energy Mater. Sol. Cells*, **95**(11), pp. 2994–3000.
- [88] Li Y., Xie H. Q., Yu W., and Li J., 2011, "Investigation on heat transfer performances of nanofluids in solar collector," *Materials Science Forum*, pp. 33–36.
- [89] He Y., Wang S., Ma J., Tian F., and Ren Y., 2011, "Experimental study on the light-heat conversion characteristics of nanofluids," *Nanosci. Nanotechnol. Lett.*, **3**(4), pp. 494–496.

- [90] Khullar V., Tyagi H., Phelan P. E., Otanicar T. P., Singh H., and Taylor R. A., 2013, "Solar energy harvesting using nanofluids-based concentrating solar collector," *J. Nanotechnol. Eng. Med.*, **3**(3), p. 031003.
- [91] Polyanskiy M., "Refractive index database" [Online]. Available: <http://refractiveindex.info/?shelf=main&book=Au&page=Hagemann>. [Accessed: 29-May-2014].
- [92] Matzler C., 2002, "MATLAB functions for Mie scattering and absorption," Res. Rep. No. 2002-08 [Online]. Available: http://arrc.ou.edu/~rockee/NRA_2007_website/Mie-scattering-Matlab.pdf. [Accessed: 19-Mar-2014].
- [93] Zhang H., Chen H.-J., Du X., Lin G., and Wen D., 2015, "Dependence of Photothermal Conversion Characteristics on Different Nanoparticle Dispersions," *J. Nanosci. Nanotechnol.*, **15**(4), pp. 3055–3060.
- [94] Sajid Hossain M., Saidur R., Mohd Sabri M. F., Said Z., and Hassani S., 2015, "Spotlight on available optical properties and models of nanofluids: A review," *Renew. Sustain. Energy Rev.*, **43**, pp. 750–762.
- [95] Mak K. F., Ju L., Wang F., and Heinz T. F., 2012, "Optical spectroscopy of graphene: From the far infrared to the ultraviolet," *Solid State Commun.*, **152**(15), pp. 1341–1349.
- [96] Zhou F., Xing D., Ou Z., Wu B., Resasco D. E., and Chen W. R., 2009, "Cancer photothermal therapy in the near-infrared region by using single-walled carbon nanotubes," *J. Biomed. Opt.*, **14**(2), p. 021009.
- [97] Fisher J. W., Sarkar S., Buchanan C. F., Szot C. S., Whitney J., Hatcher H. C., Torti S. V., Rylander C. G., and Rylander M. N., 2010, "Photothermal response of human and murine cancer cells to multiwalled carbon nanotubes after laser irradiation," *Cancer Res.*, **70**(23), pp. 9855–9864.
- [98] Li X., Wang X., Zhang L., Lee S., and Dai H., 2008, "Chemically derived, ultrasmooth graphene nanoribbon semiconductors," *Science* (80-.), **319**(5867), pp. 1229–1232.
- [99] Jiao L., Zhang L., Wang X., Diankov G., and Dai H., 2009, "Narrow graphene nanoribbons from carbon nanotubes," *Nature*, **458**(7240), pp. 877–880.
- [100] Feng L., and Liu Z., 2011, "Graphene in biomedicine: opportunities and challenges," *Nanomedicine*, **6**(2), pp. 317–324.

- [101] Yang K., Feng L., Shi X., and Liu Z., 2013, "Nano-graphene in biomedicine: theranostic applications," *Chem. Soc. Rev.*, **42**(2), pp. 530–547.
- [102] Sarkar J., Ghosh P., and Adil A., 2015, "A review on hybrid nanofluids: Recent research, development and applications," *Renew. Sustain. Energy Rev.*, **43**, pp. 164–177.
- [103] Modest M. F., 2003, *Radiative heat transfer*, Second Edition, Academic Press.
- [104] Jacques P. and, 1998, "Optical absorption of water compendium," Oregon Med. Laser Cent. [Online]. Available: <http://omlc.ogi.edu/spectra/water/abs/index.html>. [Accessed: 20-May-2014].
- [105] Hale G. M., and Querry M. R., 1973, "Optical constants of water in the 200-nm to 200-microm wavelength region," *Appl. Opt.*, **12**(3), pp. 555–563.
- [106] Averitt R. D., Westcott S. L., and Halas N. J., 1999, "Linear optical properties of gold nanoshells," *J. Opt. Soc. Am. B*, **16**(10), p. 1824.
- [107] Link S., and El-Sayed M. A., 2000, "Shape and size dependence of radiative, non-radiative and photothermal properties of gold nanocrystals," *Int. Rev. Phys. Chem.*, **19**(3), pp. 409–453.
- [108] Lidorikis E., and Ferrari A. C., 2009, "Photonics with multiwall carbon nanotube arrays," *ACS Nano*, **3**(5), pp. 1238–1248.
- [109] Vialla F., Roquelet C., Langlois B., Delport G., Santos S. M., Deleporte E., Roussignol P., Delalande C., Voisin C., and Lauret J.-S., 2013, "Chirality dependence of the absorption cross section of Carbon nanotubes," *Phys. Rev. Lett.*, **111**(13), p. 137402.
- [110] Butt H., Wilkinson T. D., and Amaratunga G. A. J., 2012, "FEM modeling of periodic arrays of multiwalled carbon nanotubes," *Prog. Electromagn. Res. M*, **22**, pp. 1–12.
- [111] Djurišić A. B., and Li E. H., 1999, "Optical properties of graphite," *J. Appl. Phys.*, **85**(10), p. 7404.
- [112] Bayazitoglu Y., and Ozisik N. M., 2012, *A textbook for heat transfer fundamentals*, Begell House Inc., New York and Connecticut.
- [113] Bruce H. Mahan R. J. M., 1987, *University Chemistry*, The Benjamin/Cummings Publishing Company, Inc., California.

- [114] Ge X., and Wang X., 2009, "Estimation of Freezing Point Depression, Boiling Point Elevation, and Vaporization Enthalpies of Electrolyte Solutions," *Ind. Eng. Chem. Res.*, **48**(4), pp. 2229–2235.
- [115] XIE H., Jifen WAN, and CHEN L., 2009, "Effects on the Phase Transformation Temperature of Nanofluids by the Nanoparticles," *J. Mater. Sci. Technol.*, **24**(05), pp. 742–744.
- [116] Kim S. J. P. D. M. I. of T., 2007, "Pool boiling heat transfer characteristics of nanofluids."
- [117] Harikrishnan S., and Kalaiselvam S., 2013, "Experimental Investigation of Solidification and melting Characteristics of Nanofluid as PCM for Solar Water Heating Systems," *Int. J. Emerg. Technol. Adv. Eng.*, **3**, pp. 628–635.
- [118] Maré T., Sow O., Halelfadl S., Lebourlout S., and Nguyen C. T., 2011, "Experimental Study of the Freezing Point of Al₂O₃ Water Nanofluid," *Adv. Mech. Eng.*, **2012**.
- [119] Raam Dheep G., and Sreekumar A., 2014, "Influence of nanomaterials on properties of latent heat solar thermal energy storage materials – A review," *Energy Convers. Manag.*, **83**, pp. 133–148.
- [120] Yu J. Z., Li Z. L., and Hu H. Y., 2013, "Experimental Study of Nanofluids Crystallize on Low Temperature Environment," *Applied Mechanics and Materials*, pp. 262–265.
- [121] Wang J., Xie H., Li Y., and Xin Z., 2010, "PW based phase change nanocomposites containing γ -Al₂O₃," *J. Therm. Anal. Calorim.*, **102**(2), pp. 709–713.
- [122] Kim S., and Drzal L. T., 2009, "High latent heat storage and high thermal conductive phase change materials using exfoliated graphite nanoplatelets," *Sol. Energy Mater. Sol. Cells*, **93**(1), pp. 136–142.
- [123] Jain P. K., El-Sayed I. H., and El-Sayed M. A., 2007, "Au nanoparticles target cancer," *nanotoday*, **2**(1), pp. 18–29.
- [124] Kessentini S., and Barchiesi D., 2012, "Quantitative comparison of optimized nanorods, nanoshells and hollow nanospheres for photothermal therapy," *Biomed. Opt. Express*, **3**(3), pp. 590–604.
- [125] Evanoff D. D., and Chumanov G., 2005, "Synthesis and optical properties of silver nanoparticles and arrays," *ChemPhysChem*, **6**(7), pp. 1221–31.

- [126] Edgar J. A., Zareie H. M., Blaber M., Dowd A., and Cortie M. B., 2008, "Synthesis of hollow gold nanoparticles and rings using silver templates," 2008 Int. Conf. Nanosci. Nanotechnol., pp. 36–39.
- [127] Cole J. R., and Halas N. J., 2006, "Optimized plasmonic nanoparticle distributions for solar spectrum harvesting," *Appl. Phys. Lett.*, **89**(15).
- [128] Tuersun P., and Han X., 2013, "Optical absorption analysis and optimization of gold nanoshells," *Appl. Opt.*, **52**(6), pp. 1325–9.
- [129] Correa-Duarte M. A., Farle M., Lo A., Sieradzki K., and Diaz R., 2006, "Bifunctional gold-coated magnetic silica spheres," *Chem. Matters*, **18**(11), pp. 2701–2706.
- [130] Melancon M. P., Elliott A., Ji X., Shetty A., Yang Z., Tian M., Taylor B., Stafford R. J., and Li C., 2011, "Theranostics with multifunctional magnetic gold nanoshells: photothermal therapy and T2* magnetic resonance imaging," *Invest. Radiol.*, **46**(2), pp. 132–40.
- [131] Larson T. A., Bankson J., Aaron J., and Sokolov K., 2007, "Hybrid plasmonic magnetic nanoparticles as molecular specific agents for MRI/optical imaging and photothermal therapy of cancer cells," *Nanotechnology*, **18**(32), p. 325101.
- [132] Chen J., Saeki F., Wiley B. J., Cang H., Cobb M. J., Li Z. Y., Au L., Zhang H., Kimmey M. B., Li X., and Xia Y., 2005, "Gold nanocages: bioconjugation and their potential use as optical imaging contrast agents," *Nano Lett.*, **5**(3), pp. 473–7.
- [133] Anderson L. J. E., Payne C. M., Zhen Y. R., Nordlander P., and Hafner J. H., 2011, "A tunable plasmon resonance in gold nanobelts," *Nano Lett.*, **11**(11), pp. 5034–7.
- [134] Kim D. Y., Yu T., Cho E. C., Ma Y., Park O. O., and Xia Y., 2011, "Synthesis of gold nano-hexapods with controllable arm lengths and their tunable optical properties," *Angew. Chem. Int. Ed. Engl.*, **50**(28), pp. 6328–31.